Diss. ETH No. 19188

Laser sintered meso scale reactor by design: Characterization of heat and mass transfer

A dissertation submitted to

ETH Zurich

for the degree of

Doctor of Sciences

presented by

Cédric Hutter
MSc Process Engineering

born on July 15, 1980

citizen of
Lalden (VS), Eggerberg (VS)
Switzerland

Accepted on the recommendation of

Prof. Dr. Dr. h.c. Philipp Rudolf von Rohr (ETH Zurich), examiner
Prof. Dr. Massimo Morbidelli (ETH Zurich), co-examiner
Dr. David Ruppen (DSM Nutritional Products), co-examiner

Zurich, 2010

Um ein tadelloses Mitglied einer Schafherde sein zu können, muß man vor allem ein Schaf sein.

Albert Einstein

Vorwort

Diese Dissertation wäre ohne die Unterstützung vieler Leute nicht möglich gewesen denen ich nachfolgend danken möchte. Während der Projektdauer von 3 Jahren wurde diese Arbeit von der Kommission für Technologie und Innovation (KTI) des Bundes und den Firmen DSM Nutritional Products und Premex Reactor AG finanziert. Ich möchte mich herzlich für das Vetrauen bedanken, welches mir während dieser Zeit entgegengebracht wurde. Im Speziellen gilt der Dank den Projektverantwortlichen Dr. Franz Mascarello und Hans-Peter Zbinden für die stets kollegiale und offene Zusammenarbeit.

Mein besonderer Dank möchte ich an meinen Doktorvater Prof. Dr. Philipp Rudolf von Rohr aussprechen, der mir die Möglichkeit geboten hat die Dissertation in seinem Labor durchzuführen. Dabei ist er mir während der gesamten Zeit mit Rat und Tat zur Seite gestanden und hat es stets verstanden mich immer wieder aufs Neue zu motivieren ohne mich dabei meiner Freiheit zur Gestaltung der Doktorarbeit zu berauben.

Prof. Dr. Morbidelli und Dr. David Ruppen danke ich für die Bereitschaft zur Übernahme der Korreferate, trotz ihrer vollen Terminkalender. Zudem bin ich David für die vielen guten Gespäche während unserer Zusammenarbeit und den neuen Schwung dankbar, den er in unser Projekt einbringen konnte.

Ein recht herzliches Dankeschön möchte ich auch an alle aus externen Labors und Firmen richten, die mich unterstützt und begleitet haben: Jörg Petrasch für seine Hilfe bei der Bearbeitung der X-ray scans und Igor Zinovik für die interessante Zusammenarbeit bei der Modellierung. Danke Dominik Obrist für die guten wissenschaftlichen Gespräche und

den frühen Gruss am Morgen in der Tannenbar. Vielen Dank Ben Seeber für die Hilfe bei BET Messungen und Ueli Kiefer für die guten Ideen und Diskussionen. Herzlichen Dank auch an Julius Jeisy der das Projekt mitinitiiert und damit einen grossen Anteil an der daraus entstandenen Erfindung hat.

Mein Dank richtet sich auch an viele, teils ehemalige, Mitglieder des Instituts für Verfahrenstechnik, die ich meist bereits als Student kannte und welche mich dazu motiviert haben, noch länger an der ETH Zürich zu bleiben. Danke Ädu und Franz, dass ich bei euch während meiner Semester- und Diplomarbeit sehr viel über das wissenschaftliche Arbeiten erlernen konnte. Danke Carsten, ob wissenschaftlich oder persönlich, für mich warst du immer eine Herausforderung! Einen speziellen Dank an dich Simon, von dir durfte ich am meisten lernen und ich tue es immer noch. Auch dir Pädi danke für die schöne Zeit. Unvergesslich bleiben für mich so manche Erlebnisse, wie die Kletterpartie auf das Zerfreilahorn oder die Staumauer in Luzzone. Danke Jan, für die gemütlichen Abende beim Snooker spielen! Danke Ronny und Stefan, dass ich immer bei euch vorbeischauen durfte, wenn ich etwas gebraucht habe. Danke Jossi, dass du mich zum Walliservertreter am Institut gemacht hast. Ich habe auch schon wieder für guten Nachwuchs gesorgt... Ich danke auch Thomas für deine Freundschaft und die geselligen Abende am Uetli- und am Züriberg.

Bei der Planung, Konstruktion und dem Aufbau der experimentellen Anlagen konnte ich immer auf die Hilfe und Erfahrung unserer Werkstatt setzen. Danke Bruno und Peter für eure guten Ideen und die stets zuverlässigen Aufbauten. Vielen Dank auch an René, Daniel, Christian, Martin und Herr Dörfler für die praktischen Ratschläge in technischen Belangen und danke Markus für deine Hilfe in chemischen Fragen. Ich habe die freundschaftliche Zusammenarbeit mit der Werkstatt sehr geschätzt und habe deshalb auch die gemeinsamen Apéros immer sehr genossen! Ein spezielles Dankeschön geht an Silke und Silvia für die prompte Erledigung administrativer Angelegenheiten und den Einsatz von Sascha und Christian bei Informatikproblemen.

Natürlich gehört auch der gesamten LTR Gruppe ein grosses Dankeschön. Ich habe die Zeit mit euch sehr genossen und wünsche euch allen viel Erfolg für eure Zunkunft. Vor allem möchte ich meinen Bürokollegen Paule und Lutz für die tolle Zeit bedanken. Ich werde sicher

noch oft an das ML H15 zurückdenken!

Ein ausserordentliches Dankeschön geht auch an alle Studenten, die ich während meiner Zeit betreuen durfte. Sie haben enorm viel zum Projekt beigetragen und ich konnte von allen etwas für die Zukunft mitnehmen. Merci Adi, Christoph, Christopher, Dani Baeriswyl, Dani Büchi, Dominik, Denis, Richi, Sebastian und Veronika. Ich hoffe ihr hattet Spass an eurer Arbeit und konntet etwas lernen. Adi, Denis und Richi wünsche ich alles Gute für ihre Doktorarbeit, welche sie am LTR schreiben werden.

Ein besonders riesiger Dank geht an meine Freunde die mir immer die nötige Unterstützung geben, wann immer ich sie brauche. "Merci villmal" Adi, Chrigi, Dresi, Gely, Gian, Kaajo, Pasci, und Sili. Ich kann immer auf euch zählen und ich durfte schon einiges mit euch erleben. Hoffentlich verlieren wir uns nie aus den Augen.

Mein grösster Dank geht an meine gesamte Familie. "Merci Bella dass dü während der ganz Zit immer fer mich da bisch gsi und vor allem fer dini Geduld am Schluss va miner Arbeit!" Danke Elena dass du mich jeden Abend mit einem Lächeln an der Türe begrüsst hast und so viel Sonnenschein in unser Leben bringst. Danke Céline, dass du schon bald unsere kleine Familie erweitern wirst. Danke Mims und Pips für eure ständige Unerstützung und dass ihr mir ein Studium an der ETH erst ermöglicht habt. Und danke meinen Geschwistern Magaly und Timi und ihren Familien, dass sie immer für mich da sind. Ein grosses Danke auch an meine Schwiegereltern und Schwager für ihre Unterstützung. Bei ihnen habe ich ein weiteres zuhause gefunden.

Zürich, July 2010 - Cédric Hutter

Abstract

In the past decade the chemical and pharmaceutical industry underwent a big change. The growing need of energy savings and sustainable production led to a fast development of new technologies for process intensification. The basic idea thereof is to reduce the plant scale and with it the capital expenditures and energy consumption and to enhance the safety for human beings and environment. The micro reaction technology originating from this trend in industry encounters huge difficulties in the implementation of real production processes. The small volumetric flow rates, the predominantly laminar flow, the prevention of clogging, the fabrication of the reactors and the interface to conventional production equipment are challenges which are still not solved and which avoid an economical production with constant product quality.

In this thesis a combined experimental and numerical characterization of mass and heat transfer in a continuous meso scale reactor is addressed. The patented reactor approach is based on the concept of highly porous structures as static mixing elements with large specific surface area, manufactured by selective laser sintering. The basic geometry is the negative pattern of tetrahedral overlapping spheres with a diameter of 2.9 mm subtracted from a cylinder with a diameter of 7 mm resulting in a foam like structure (porosity of 84%). This sintered static mixer is compared to commercially available metal foam inserts of different pore sizes ranging from 20 to 45 pores per inch (ppi). Particle image velocimetry (PIV) is performed to examine the spatial variation of the axial and radial velocity of water flowing through the device in a plane downstream the reactor outlet. Laser induced fluorescence (LIF) is applied to asses the transport of a passive scalar through the porous

structures. The Reynolds numbers based on the empty tube were ranging from 600 to 7600. This corresponds to high volumetric flow rates up to 2.5 l/min. For the same conditions tracer pulse and calorimetric experiments were performed to study the axial dispersion and the heat transfer in the reactor.

The results show a distorted flow field at the outlet of the reactor with a strongly enhanced turbulent kinetic energy induced by the porous structure. The combination of flow lamination and convective transport leads to a fast homogenization of scalar species in the bulk. The narrow residence time distribution is attributed to the forced radial velocity leading to an overall plug flow behavior. The estimated dispersion coefficient compares well with literature data of packed beds and common packing materials although the porosity is much higher and the pressure drop is strongly decreased. The very large inner surface area and the turbulent flow within the structure affect also the heat transfer which is found to be increased in comparison to an empty tube case. Compared to inserted commercially available foams in empty tubes the fully sintered device performs by far best due to the fixed connection of the porous media with the surrounding reactor wall. By the numerical results of a Large Eddy Simulation (LES) the effect of the geometry on the velocity field is discussed. It can be shown that the ligament shape and thickness are key parameters for the scaling of porous media. This assumption is reinforced by the better performance of the designed structure in terms of heat and mass transfer compared to commercially available metal foam.

This study suggests that innovative meso scale reactors by design offer many advantages compared to other developments in the field of process intensification. The free choice of the geometry allows to control and scale the transport properties for a wide range of technical applications. Preliminary studies of gas-liquid flows in the reactor show for example a huge potential of the presented concept in the handling of complex multiphase flows.

Zusammenfassung

In den letzten 10 Jahren hat die chemische und pharmazeutische Industrie einen grossen Wandel durchlaufen. Der steigende politische und gesellschaftliche Druck Energie zu sparen und nachhaltig zu produzieren hat zu einer schnellen Entwicklung von neuen Technologien geführt. Ein Grundkonzept ist die Miniaturisierung von Anlagen und damit die Reduktion der Investitionskosten und des Energieverbrauchs bei gleichzeitiger Erhöhung der Sicherheit für Mensch und Umgebung. Die durch diese Entwicklung entstandene Mikroreaktionstechnik konnte jedoch bis anhin nicht grosstechnisch umgesetzt werden. Probleme, welche einen ökonomischen Einsatz solcher Systeme verhindern sind vor allem die kleinen Volumenströme, der vorwiegend laminare Fluss, die schnelle Verstopfung der kleinen Känale, die Fertigung der Reaktoren und der Anschluss an das Standardequipment.

In dieser Arbeit befassen wir uns mit der experimentellen und numerischen Charakterisierung von Stoff- und Wärmetransport in einem kontinuierlichen Reaktorsystem mit charakteristischem Durchmesser im Millimeterbereich. Der patentrechtlich geschützte Reaktor beruht auf dem Einsatz statischer Mischer, bestehend aus porösen Strukturen mit hoher spezifischer Oberfläche, welche mittels selektivem Laser sintern hergestellt werden. Die Grundgeometrie ist das negative Abbild von sich thetraedrisch überlappenden Kugeln, welche einen Durchmesser von 2.9 mm aufweisen und in einem Abstand von 2.75 mm zueinander angeordnet sind. Diese werden von einem Zylinder mit 7 mm Durchmesser subtrahiert und bilden so eine schaumartige Struktur mit einer Porosität von 84%. Dieser gesinterte statische Mischer wird mit kommerziell erhältlichen Metallschäumen mit Porengrössen von 20 bis 45 Poren

pro Inch (ppi) verglichen. Dazu werden die Geschwindigkeitsfelder am Ausgang der Mischelemente mittels optischer Messungen bestimmt und deren zeitliche und örtliche Variationen untersucht. Den Einfluss der Strukturen auf den Stofftransport eines passiven Skalars wird mittels eines fluoreszierenden Tracers erforscht. Die berechneten Reynoldszahlen basieren auf dem hydraulischen Durchmesser des Leerrohrs und bewegen sich im Bereich von 600 bis 7600, was Volumenströmen von bis zu 2.5 l/min entspricht. Für diesselben Strömungsgeschwindigkeiten wurde zudem die axiale Dispersion mittels Tracerpulsexperimenten charakterisiert und der Wärmeübergang durch kalorimetrische Messungen bestimmt.

Die Ergebnisse zeigen einen klaren Einfluss der porösen Struktur auf die Strömung durch den Eintrag von turbulenter kinetischer Energie. Die Kombination von Strömungslaminierung und konvektivem Stofftransport führt zu einer schnellen Homogenisierung eines passiven Skalars über den Reaktorquerschnitt. Die gemessene, enge Verweilzeitverteilung ist der erhöhten erzwungenen radialen Geschwindigkeit zuzuschreiben, welche zu einem ausgeprägten Pfropfenströmungsprofil führt. Obwohl die Porosität der untersuchten Strukturen viel höher ist und somit der Druckabfall geringer, stimmen die berechneten Dispersionkoeffizienten gut mit Literaturdaten von Festbetten und herkömmlichen Kolonnenpackungen überein. Die hohe innere Oberfläche und die turbulente Strömung in der Struktur führen durch die Analogie zwischen Stoff- und Wärmetransport zu einer erhöhten Wärmeübertragungsleistung. Die feste Wandanbindung beim gesinterten Reaktor, welche durch das Herstellungsverfahren realisiert wird, erweist sich zusätzlich als enormer Vorteil im Vergleich zu kommerziellen Schäumen, welche nur ins Rohr eingepresst werden. Die numerischen Berechnungen der Strömung zeigen zudem, dass die Steggeometrie ein entscheidender Faktor in der Skalierung von porösen Medien darstellt, was mittels der experimentellen Resultate bekräftigt wird.

Diese Arbeit zeigt die Vorteile des vorgestellten kontinuierlichen Rektorkonzepts gegenüber anderen Entwicklungen im Bereich der Prozessoptimierung auf. Die freie Wahl der Geometrie ermöglicht eine Auslegung des Reaktors für einen grossen Bereich technischer Anwendungen. Beispielsweise belegen erste Vorversuche das grosse Potential des Konzepts für die Durchführung von komplexen Mehrphasenreaktionen.

Table of Contents

Nomenclature

Roman symbols

a	constant	
A	tube cross section	[m^2]
A_{con}	interfacial area	[m^2]
A_s	surface area per unit volume of solid	[m^2/m^3]
b	constant	
c	constant	
c	concentration	[g/kg]
c_p	specific heat capacity	[J/(kgK)]
$\overline{c}$	mean concentration	[mol/l]
C	BET constant	[−]
C_s	Smagorinsky model constant	[−]
$C(j\omega)$	concentration signal in frequency domain	[−]
d	constant	
d	distance to the closest wall	[m]
d_p	pore size	[m]
D	inner diameter of the glass tube	[mm]
D_L	axial dispersion coefficient	[m^2/s]
D_m	molecular diffusion coefficient	[m^2/s]
$E(t)$	residence time distribution	[1/s]
$E_f(j\omega)$	residence frequency distribution	[−]
f	friction factor	
$F(t)$	cumulative residence time distribution	[−]
$F(j\omega)$	filter in the frequency domain	[−]
H	enthalpy	[J/kg]

I	light intensity	[a.u.]
I_0	incident light intensity	[a.u.]
j	imaginary unit	
k	turbulent kinetic energy	[m^2/s^2]
k_{cond}	conductive heat transfer coefficient	[$W/(m^2K)$]
k_{conv}	convective heat transfer coefficient	[$W/(m^2K)$]
k_{eff}	effective thermal conductivity	[W/(mK)]
k_r	residual kinetic energy	[m^2/s^2]
k_r	total radial heat transfer coefficient	[$W/(m^2K)$]
k_{rad}	radiative heat transfer coefficient	[$W/(m^2K)$]
L	length of the reactor	[m]
L	length of the mixing elements	[mm]
L	length of the period	[mm]
L_{ij}	resolved stress	[m^2/s^2]
L_s	Smagorinsky lengthscale	[m]
m	number of resolved data points	
$\dot{m}$	mass flow rate	[kg/s]
M	scaled composite rate of strain	[m^2/s^2]
M_g	mass flow rate gas	[m^3/s]
M_l	mass flow rate liquid	[m^3/s]
M_{ij}	modeled stress	[m^2/s^2]
n	number of images	
n_{ads}	adsorbed specific amount	[mol]
n_m	amount in the monolayer	[mol]
N_L	Avogadro constant	[1/mol]
p	pressure	[bar]
p_0	saturation vapor pressure	[Pa]
P	local pressure	[bar]
Pe_p	Peclet number	[–]
q	volumetric flow rate of side stream	[l/min]
$\dot{q}_h$	heating power	[W]
$\dot{q}''_h$	area specific heating power	[W/m^2]
Q	volumetric flow rate of main stream	[l/min]
$\dot{Q}_h$	total heating power	[W]
$\dot{Q}_p$	pumping power	[W]
R	radius of the glass tube	[mm]
R	universal gas constant	[J/(molK)]

Re	Reynolds number	
Re_p	pore Reynolds number	[-]
Ri	Richardson number	[-]
s	slip	[-]
S	rate of strain	[l/s]
S	space for single molecule	[m^2]
S_{BET}	BET surface	[m^2]
Sc	Schmidt number	[mm]
t	time	[s]
T	temperature	[K]
$\mathbf{u}$	velocity vector (u,v,w)	
u	radial velocity component	[m/s]
$\overline{u}$	mean radial velocity component	[m/s]
u'	fluctuation of radial velocity component	[m/s]
u_b	interstitial bulk velocity	[m/s]
U_B	bulk velocity	[m/s]
v	radial velocity component	[m/s]
$\overline{v}$	mean radial velocity component	[m/s]
v'	fluctuation of radial velocity component	[m/s]
V	volume of the computational cell	[m^3]
$\dot{V}$	volumetric flow rate	[m^3/s]
V_g	volume of gas	[m^3]
V_l	volume of liquid	[m^3]
w	axial velocity component	[m/s]
$\overline{w}$	mean axial velocity component	[m/s]
w'	fluctuation of axial velocity component	[m/s]
x	radial coordinate direction	
$\dot{x}$	mass transport fraction [−]	
y	radial coordinate direction	
y^+	dimensionless distance to the wall	
z	axial coordinate direction	

Greek symbols

α	constant
β	constant

γ	number of pores per inch	[−]
δ_{ij}	Kronecker Delta	
ϵ	energy dissipation rate	[m^2/s^3]
ε	porosity	[−]
ε	absorption coefficient	[a.u.]
ε_V	void fraction	[−]
$\dot{\varepsilon}_V$	volumetric transport fraction	[−]
η	Kolmogorov lengthscale	[m]
κ	von Karman constant	[−]
λ	optimization parameter	[−]
μ	dynamic viscosity	[Pa · s]
ν	kinematic viscosity	[m^2/s]
ν_r	eddy viscosity of residual motions	[m^2/s]
ρ	density	[kg/m^3]
σ	standard deviation	
τ	mean residence time	[s]
τ_{ij}^r	anisotropic residual stress tensor	[m^2/s^2]
τ_{ij}^R	residual stress tensor	[m^2/s^2]
τ_w	wall shear stress	[Pa/m^2]
ϕ	quantum efficiency	[−]
ω	imaginary part	

Abbreviations

BET	Brunauer, Emmet and Teller method
CAD	computer assisted design
CCD	charge-coupled device
CoV	coefficient of variation
CoV_0	initial coefficient of variation
DNS	direct numerical simulation
FFT	fast Fourier transformation
HPLC	high performance liquid chromatography
KCl	potassium chloride
LES	large eddy simulation
LB	Lattice Boltzmann
Nd:YAG	neodymium:yttrium aluminium garnet

	$(Y_3Al_5O_{12})$ crystal
PIV	particle image velocimetry
PLIF	planar laser induced fluorescence
ppi	pores per inch
RANS	Reynolds averaged Navier-Stokes
RTD	residence time distribution
SL	stereolithography
SLS	selective laser sintering
$\overline{(\cdot)}$	time average
$(\cdot)'$	fluctuation
$\langle\cdot\rangle$	spatial average
$\lvert(\cdot)\rvert$	absolute value
$\tilde{(\cdot)}$	filtered

Sub- and superscripts

0	initial quantity
ads	adsorption
b	interstitial
B	bulk quantity
c	convective
cond	conduction
conv	convection
f	fluid
g	gas
h	hydraulic
i	inner
i, j, k, l	running index
in	inlet
l	liquid
m	molecular
o	outer
out	outlet
p	pore
pl	plate
pulse	pulse experiment

r	radial
rad	radiation
rms	root mean square
s	solid
$step$	step experiment
w	wall

Chapter 1

Introduction

1.1 Motivation

In the industry large scale equipment, predominantly dis- or semi-continuous batch processes, are still used due to the economy of scale. For chemical plants the investment costs are in general proportional to the capacity to the power of 0.5 to 0.7. The growing need of energy saving and sustainable production leads to a demand for intensified continuous devices as the recuperation of energy is more efficient and mass and heat transfer is strongly enhanced. The big efforts to design such miniaturized continuous systems often failed at the low productivity. Approaches like spinning disc or HiGEE reactors lead in addition to constructive problems and they are hard to monitor. In small systems, e.g. continuous micro reactors, the flow rates are very low and a scale up is needed, mostly realized by numbering up of individual devices. For a large-scale production this is not an economical solution. But in spite of the huge pressure drop and the predominant laminar flow within microsystems the small scales offer many advantages. A qualitative comparison of macro- and micro-devices is presented in Figure 1.1. The demonstrated preferences of different scales lead to the conclusion that a favorable reactor size for economical and sustainable production is found at the meso scale. From the chemical point of view also the mode of operation of such a device is important, since continuous plug flow reactors

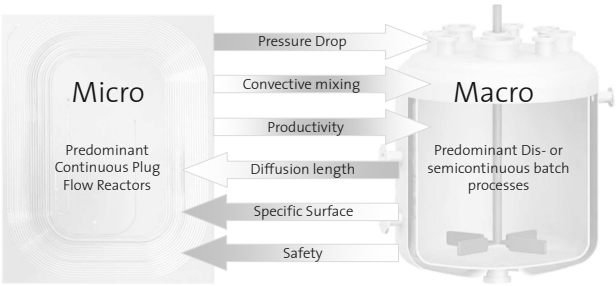

Figure 1.1: Qualitative comparison of macro and micro scale processes. The arrow shows the preferable scale of operation for every presented quality. The contrast level corresponds to the absolute value of the quality (the darker the higher).

would be often preferred. The narrow residence time distribution and the enhanced heat transfer in turbulent flows enable isothermal and safe conditions. For this reason a high selectivity and product quality can be achieved. The fast development of in situ measurement techniques has accounted in addition for a good monitoring and therewith control of such continuous devices in the past view years.

1.2 Objectives

The main objective of the thesis is the development and characterization of a continuous plug flow reactor combining the advantages of small scale reactors with the productivity of macro scale devices. The new system has to handle fast and highly exothermic reactions at high production scale throughput (flow rates up to 2.5 l/min). In order to fulfill the standards of the pharmaceutical and chemical industry the reactor should be made of corrosion resistant materials. It has to be beneficial compared to conventional macro devices in terms of stability, heat and mass transfer and compared to micro devices in terms of throughput, pressure drop and maintenance. An economical manufacturing method

for the meso scale reactor has to be proposed allowing the simple construction of different reactor designs with a free choice of predominantly metallic materials. The feasibility of the device has to be shown at the end of the thesis by means of an industrial relevant reaction.

1.3 Outline of the thesis

Our approach is to use high porous micro structured inserts for plug flow reactors in the millimeter range enabling high throughput at comparable small pressure drop. A huge potential arises from open cell metal foams as porous reactor inserts with their outstanding thermal properties. The high specific surface makes solid foams especially interesting for heterogeneous catalyzed reactions. Although the first results on mass and heat transfer with commercial metal foam were very promising, further investigations showed that a major limitation, apart from the finite choice of corrosion resistant material and its machining, is the dimensioning of a foam reactor to meet industrial standards. For this reason we developed the approach further by applying manufacturing methods known from the field of rapid prototyping. By stereo lithography (SL) and selective laser sintering (SLS) it is possible to build nearly any three-dimensional shape made from plastic respectively metal alloy as one single part. A comparison of the first concept (commercially available metal foam inserted into an empty tube) with the patented new approach is depicted in Figure 1.2. Experiments with the fully sintered porous reactor made of stainless steel have shown a strongly enhanced heat transfer rate due to the fixed connection to the wall compared to simply inserted commercial foam. The system, which complies with a so called heat exchanger reactor (Anxionnaz et al. [5]), opens up completely new vistas in the wide and booming field of Process Intensification (PI). The applied manufacturing method permits complex geometries without loosing structural stability or running into corrosion problems. A major advantage of the new concept, covering the application in the whole range of unit operations, is the flexibility.

The presented device will be characterized within this thesis in terms of heat and mass transfer. Within a literature overview recent investigations related to the studied problems will be presented followed by

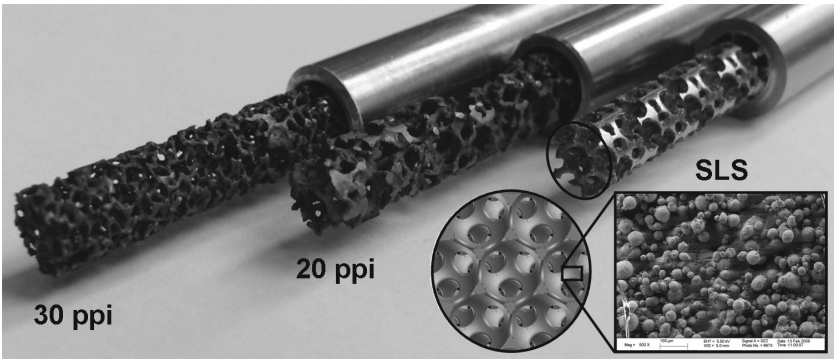

Figure 1.2: Different approaches in comparison to each other. On the left the inserted commercial foam elements (20ppi and 30 ppi) and on the right the fully sintered structure (SLS). A SEM image with a magnification of 500 clarifies the roughness of the sintered material which is in the order of the diameter of metal powder particles treated.

the theoretical considerations explaining the basic concepts used for the analysis of the experimental data. In chapter 4 basically four experimental setups will be explained in detail. The results obtained by this setups are presented in chapter 6. By means of an optical facility to measure the concentration of an injected dye and velocity fields simultaneously, the porous media was investigated concerning the radial dispersion of a passive scalar. The axial dispersion was characterized by the aid of electrodes measuring the concentration of a salty tracer dye at the inlet and outlet of the test section. By calorimetric measurements finally the heat transfer through the porous media is estimated. In the numerical part of the thesis results of a Large Eddy Simulation (LES) will be presented. They deliver insight into the flow within the structure and explain e.g. the strong influence of the ligament shape on mass and heat transfer. The concluding remarks are followed by an outlook wherein the future and already running projects are summarized and preliminary results are presented. For example, we broach the issue of gas-liquid flow through the structure and present results of recent investigations.

Chapter 2

State of the art

In this chapter the literature with respect to the experimental and numerical investigations performed within this work is summarized. The heat transfer in solid foams was widely studied in the past decade due to the original major application in the heat exchanger technologies. The expansion of the investigations on other topics shows a trend of applying foam structures in completely different technical employments. A huge field of those applications is established under the topic process intensification whereas the part of literature dealing with chemical synthesis in such structures is very small.

2.1 Process intensification

The term Process Intensification (PI) was originally coined at Imperial Chemical Industries in the 1970's. This company with domicile in the U.K. started early with the development of HiGEE and Spinning Disc Reactors which led to the concept of PI. In charge for the development was Prof. Colin Ramshaw (e.g. Ramshaw [125]) at that time. The term PI comprehend simplified the miniaturization of unit operations. This approach involves the following deliverables:

- safety and environmental advantages
- reduction of plant scales (footprint and height)

- decreased capital expenditure
- reduced energy consumption

The advantages of miniaturized systems in terms of safety were widely discussed in literature and it was always mentioned in combination with micro reaction systems. The principle of the reduction of hazards to a significant extent (Hendershot [68]), often denoted as intrinsic safety, is also addressed by PI. The urgency on the chemical industries to produce cleaner and safer leads PI to become a major concern as it offers also many advantages in terms of process control, enhanced selectivity, decreased operational and investment costs and therefore higher productivity.

Due to the high flexibility still about 50% of the world's fine chemical production originate from batch reactors (Stitt [147]) although a number of limitations in terms of heat and mass transfer are known (Phillips et al. [117], Stitt [147]). Intensified reactor systems would be an alternative approach. A comprehensive overview of the diverse technologies in the field of heat exchanger reactors is presented in Anxionnaz et al. [5]. They comment on literature of all different intensified reactor approaches, namely spinning disk reactor, microchannel reactors, static mixers and oscillatory flow reactors. In a second part of their review they present different compact heat exchanger reactor (HEX) principles and focus on the influence of different inserts like offset strip fins, vortex generators and patented fins. Among these they refer also to metal foam inserts as static mixing elements. By solving some major problems of this new material metal foam offers new possibilities in the wide field of process intensification.

2.2 Porous media

2.2.1 Metal foam

Originally metal foams were developed for the purpose of light weight constructions (Banhart [12], Baumgartner et al. [14]). Nowadays they are used in various other applications, most prominent for heat exchange purposes (Boomsma, Poulikakos and Zwick [26]), but also as flame arrestor, shock (Ramamurty and Paul [124]) and sound absorber (Ashby

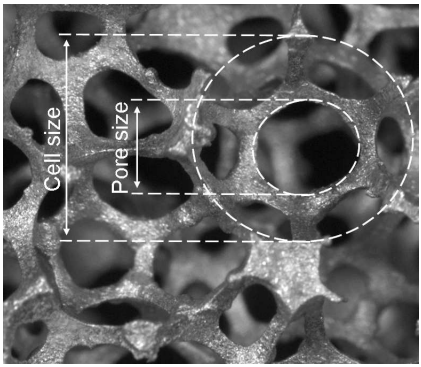

Figure 2.1: Microscopic image of aluminum metal foam. The typical shape of the cells is a tetrakaidecahedron. The pores are the openings of a cell.

and Lu [7]), etc. The different production methods for metal foams are described in Ashby et al. [6] and Banhart [11]. In general we discern between closed and open cell metal foam whereas only the open cell layout allows fluid flowing inside. This foam type consists of interconnected solid struts. The shape of a unit cell is the so called tetrakaidecahedron, a 14-faceted polyhedron, which represents the most energetically favorable shape of a single bubble in a network. The windows of a single cell are called pores as depicted in Figure 2.1. Metal foams can be characterized by the base material, the pore size and the porosity (Corporation and Aerospace [33]). Conventional materials for metal foam are Copper and Aluminum. Less common are other materials (e.g. nickel) which are more favorable concerning corrosion resistance. The pore size is described by the number of pores per inch (ppi). For metal foams this number is in the range between 5 to 100 ppi. The pore size is directly linked to the hydraulic diameter of the ligaments and has a big influence on the heat and mass transfer performance of metal foams (Boomsma and Poulikakos [24], Ferrouillat et al. [47]). The hydraulic diameter of the ligaments is increasing with increasing pore size. The porosity describes the ratio of the void volume divided by the volume of the solid material. For a small porosity the cross section of the ligaments is circu-

lar whereas for large porosities it is more triangular, which is preferable for heat transfer purposes as shown by Hackeschmidt [61]. The porosity of metal foam is typically larger than 85%. This property combined with a high specific surface of up to the order of $10^4\,m^2/m^3$ is a major advantage compared to common packing material and fixed beds. In contrast to the excellent heat transfer characteristics of open celled metal foam (Bhattacharya et al. [16], Boomsma, Poulikakos and Zwick [26], Hackeschmidt [61], Lu et al. [94]) the mass transfer (Ferrouillat et al. [47], Giani et al. [59], Stemmet et al. [143]) and the hydrodynamic flow behavior (Dimopoulos Eggenschwiler et al. [36]) was investigated only by few researchers. Within this study we ascertain metal foam from m-pore GmBH (Germany) of 20, 30 and 45 ppi concerning mixing efficiency in an application-oriented assembly with respect to the use as static mixing elements in continuous plug flow reactors.

2.2.2 Designed porous media

We developed a new type of porous material based on common rapid prototyping manufacturing processes which will be introduced in the following sections. The aim was to build a foam like well defined reference geometry to investigate heat and mass transfer and to compare the results to literature and a numerical simulation. The exact measures of the structure are defined in section 6.1.2.

Selective laser sintering and electron beam melting

In terms of chemical reactions in commercial metal foams some difficulties have to be overcome. The common material e.g. aluminum, copper etc. is not sustainable in terms of corrosion. An additional problem is the connection from the foam to the wall which is a limiting step in heat transfer. Different approaches like soldering were tested but no persistent connection was achieved. Therefore a new manufacturing approach was tested which is the so called selective laser sintering (SLS) technique. A three-dimensional structure of nearly any shape can be designed in a CAD software and then manufactured as one single part. This is done by depositing a layer of metal powder, directing energy on a selected position corresponding the CAD model to sinter it, before depositing a

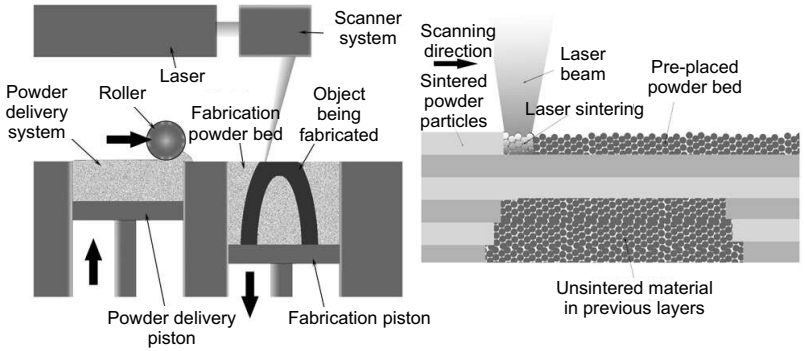

Figure 2.2: Schematic illustration (www.wikipedia.com) of the SLS process.

new layer and begin the procedure again. A schematic illustration of the process is depicted in Figure 2.2. The equipment basically consists of a powder drum, a building platform and a laser delivering the energy to sinter the material. For every cycle the powder delivery piston goes one step upwards and a roller moves the top layer to the fabrication platform, which piston moves downwards. Due to the fact that the manufacturing process has nearly no limitation in terms of the geometry up to a tolerance length scale of about 100 μm (for small parts down to 50 μm), every process specific design criteria can be fulfilled by the manufacturer. The reactor arisen in this manner is made of one piece which guarantees a good stability of the system and allows to integrate complex channels for heating or cooling, for educt feeding or product sampling. The supplier declare in the worst case 1 % residual porosity for the sintered material. A lot of different alloys are available for the use of SLS technique. In this study stainless steel of the type SS 17-2 (1.4543) was used which is a highly corrosion resistant material characterized by a high ductility.

An alternative approach to SLS is Electron Beam Melting (EBM). Instead of a laser an electron beam is focused at a selected position to melt the metal powder. Due to the higher energy density of an electron beam the process is faster and no thermal treatment of the part after

Table 2.1: Mechanical and physical properties of laser sintered parts made of stainless steel (SS 17-2)

Property	**Magnitude**
Ultimate tensile strength	$1050 \pm 50\,\mathrm{MPa}$
Yield strength	$540 \pm 50\,\mathrm{MPa}$
Elongation at break	$25 \pm 5\,\%$
Young's modulus	$170 \pm 20\,\mathrm{GPa}$
Hardness	
as laser-sintered	$\sim 230\,\mathrm{HV}$
after post-hardening	$\sim 400\,\mathrm{HV}$
Surface roughness	
after shot-peening	$0.6 - 40\,\mu\mathrm{m}$
after polishing	$< 0.5\,\mu\mathrm{m}$
Coefficient of thermal expansion	$14 \cdot 10^{-6}\,\mathrm{m/(mK)}$
Thermal conductivity at	
$20°C$	$13\,\mathrm{W/(mK)}$
$100°C$	$14\,\mathrm{W/(mK)}$
$200°C$	$15\,\mathrm{W/(mK)}$
$300°C$	$16\,\mathrm{W/(mK)}$
Maximum operating temperature	$550\,°\mathrm{C}$

assembling is needed. The disadvantage of the method is the high tolerance of $\pm 300\,\mu$m compared to SLS and the small number of suppliers of this technology. Apart from that, the methods are very similar also in the performance of the manufactured parts.

Stereolithography

The technology is based on the hardening of a polymer and works similar as the SLS method. In this case a liquid resin (UV-curable) is exposed to a UV laser which solidifies the pattern traced on the resin and adheres it to the layer below. This leads to a wavy surface observed in Figure 6.3 which is still smoother than the one of the sintered metal

Table 2.2: Mechanical and physical properties of stereolithographic parts made of WaterShed® XC 11122

Property	Magnitude
Ultimate tensile strength	$50 - 56$ MPa
Tensile Elongation	4 %
Elongation at break	$6 - 9$ %
Young's modulus	$2.860 - 2.900$ GPa
Hardness	86-87 (Shore D)
Water absorption	1.1 %
Refractive index	1.515

part. Therefore the plastic model is better suited as reference model for experimental studies to compare to modeling results. In addition the material used (WaterShed® XC 11122, DSM SOMOS®) is transparent and allows optical access.

2.3 Characterization of solid foams

2.3.1 Velocity field and scalar transport

Measurements of fluid flow through solid foams or foam like structures are very rare in literature. Hall and Hiatt [62] performed measurements of the pore scale velocity within ceramic foams. By means of Laser Doppler Anemometry (LDA) they estimated mean velocities and turbulence intensities of an air flow in foams with pore sizes from 0.8 mm to 2.5 mm. The pore Reynolds number was in the range of 20 to 200. The measurements between two foams separated by 5 mm showed a transition to fully developed pore turbulence at pore Reynolds numbers above approximately 150. Von der Schulenburg et al. [154] measured the pore scale velocity within a polyurethane foam saturated with water. The effect of foam compression on the flow field was investigated and compared with results of a Lattice Boltzmann (LB) flow simulation. The mean pore volumes were seen to decrease and a more heterogeneous flow

profile was evident as compression was increased. The flow could be adequately modeled by the proposed LB approach. Dimopoulos Eggenschwiler et al. [36] investigated the hydrodynamics in front and behind ceramic foam by means of PIV measurements. An increased uniformity of the gas flow was found behind ceramic foams in contrast to honeycomb monoliths where the uniformity does not decrease with increasing flow velocity. The better performance of foam was ascribed to the higher pressure drop and the homogenization that occurs inside the foam as a result of the momentum exchange perpendicular to the main flow direction. No further study was found dealing with velocity measurements in solid foam. In contrast to solid foams there are many publications investigating flow through other porous media like e.g. diamond-lattice networks (Zerai et al. [166]), irregularly packed spheres (Huang et al. [73]), regular packing (Horton and Pokrajac [72]) or different other porous media (Seguin et al. [134]). Those studies are however only partially valid for comparison to our investigations. No publications were found characterizing the mixing efficiency of metal foam. Only the investigation of Ferrouillat et al. [47] indirectly concerns oneself with this topic by measuring the micromixing time in foams of different pore sizes. They found a decrease of the micromixing time with increasing ligament size of the foams investigated.

2.3.2 Axial dispersion

So far and to the best of our knowledge only few publications exist characterizing the longitudinal dispersion through solid foams. Charlaix et al. [31] were the first who characterized the dispersion through sintered porous media. They investigated sintered consolidated glass beads and compared the dispersion behavior within this structure to non-consolidated packing of the same glass beads. The effective dispersion coefficient was increasing by compacting the beads and therefore decreasing the porosity. In sintered porous media anomalies in the residence time distributions were observed which are assumed to be present due to low permeability regions. Montillet et al. [101] characterized the axial dispersion in liquid flow through packed reticulated metallic foams and compared this to fixed beds of different structures. They found a very low axial dispersion for flow through the investigated Nickel foams

of 45, 60 and 100 ppi. The resulting data for very low superficial flow velocities ($u_b < 1.2 \cdot 10^{-2}$ m/s) showed that taking into account the tortuosity and dynamic surface area (defined as the wetted surface area divided by the volume of solid) is not sufficient to obtain a universal correlation equation for metal foams where the Peclet number is a function of the Reynolds number based on the pore diameter. Ceramic foams as structured catalyst inserts were investigated by Zuercher et al. [168]. The dispersion coefficients found for a gas flow at low Reynolds numbers (< 8) based on the face diameter (sum of pore diameter and mean edge width of struts) were generally higher than in glass bead packing. An empirical correlation of Wen and Fan [158] was applied representing the relationship between dispersion coefficient and Reynolds number based on the face diameter.

In order to compare our results of the axial dispersion coefficients which are obtained at elevated velocities and corresponding high Peclet numbers with existing literature, we extended the research focus to dispersion measurements in general porous media. A useful composition of earlier results of longitudinal and lateral dispersion in packed beds is given by Han et al. [64]. By comparing the different results the effect of the particle size and the length of the column on the dispersion is discussed. Delgado [35] published a review of the existing literature about dispersions in packed beds. He discusses in detail the influence of different properties of the fluids flowing through a porous media and the properties of the media itself on the dispersion behavior. An overview on the most important publications and the corresponding parameters is given in table 2.3. Also Levenspiel [90] describes in his book longitudinal mixing in pipes including predictions of longitudinal dispersion coefficients, which are universally applicable in the turbulent flow regime, and longitudinal dispersion coefficients predictions of the laminar regime, which are valid under certain conditions.

Table 2.3: Overview of different experimental studies on longitudinal dispersion in packed beds and random packing materials.

Author	Solvent	Solute	Sc	Packed bed	L(m)	d_p(mm)	L/d_p	ε	Re_p
Pfannkuch (1963)	Water	NaCl	560	Glass spheres Sand	1.5	0.355-2.1	4225-714	0.34-0.388	0.00069-9.95
Ebach and White (1958)	Water	Dye	1858	Glass spheres Raschig rings Berl saddles Intalox saddles	1.524	0.21-6.73	7257-226.4	0.34-0.632	0.0275-1023
Carberry and Bretton (1958)	Water	Dye	1858	Glass spheres Raschig rings	0.613	0.5-6	1226-102	0.365-0.645	0.258-2144
Edwards and Richardson (1968)	Air	Ar	0.72	Glass spheres Sand	1	0.377-6.07	2652-165	0.361-0.42	0.0133-32.3
Blackwell et al. (1959)	Ar	He	1.82	Sand	36.58	0.21	$1.74 \cdot 10^5$	0.339	0.00298–0.2
Han et al. (1985)	Water	NaCl	560	Glass spheres Urea-formalde-hyde sphere	1.5	2.5-15.8	600-95	0.39-0.41	0.13-5.2
Rifai et al. (1956)	Water	NaCl	560	-	1.27	0.25-0.45	5080-2822	0.375-0.395	0.000807-0.506

2.3.3 Heat transfer

Ghosh [56] gives an overview on different investigations of heat transfer in metal foams and asks, "How good is open-cell metal foam as heat transfer surface?". In his performance evaluation, he compares open-cell metal foams with conventional heat transfer surfaces by means of an area goodness factor. He concludes that foams are a promising alternative for compact heat exchangers due to the high surface area density, superior thermodynamic characteristics and good mechanical properties. It is obvious from the literature that the heat transfer mechanism in highly porous media is complex and still not fully understood. Due to the fact that the detailed geometry and the specific surface of solid foams are difficult to determine most of the authors define a pseudo convective heat transfer coefficient for the presentation of their data. A reference surface, i.e. the wall surrounding the solid foam sample, is specified. In general, the resulting pseudo convective heat transfer coefficients are functions of heat convection, heat conduction and heat radiation.

$$\alpha = f(k_{conv}, k_{cond}, k_{rad}) \tag{2.1}$$

For this reason the Nusselt correlations developed in the past decade diverge strongly, as discussed in the comprehensive review by Kurtbas and Celik [88]. Although the literature results do not permit quantitative comparisons they deliver a basic understanding of the heat transfer mechanisms in metal foam. Different variables and their effect on the heat transfer performance are summarized as follows:

Fluid: The effective thermal conductivity k_{eff} of a fluid-solid system can be generally described by the porosity of the solid ε and the conductivities of the fluid and solid phases λ_f and λ_s (Kaviany [79]):

$$k_{eff} = \varepsilon\lambda_f + (1-\varepsilon)\lambda_s \tag{2.2}$$

The fluid properties have an impact on the heat conductivity and other heat transfer mechanisms, e.g. the convective heat transfer is controlled by the heat conductivity, the viscosity and the heat capacity of the fluid. The radiation is insignificant in liquid flows while it is of importance in gases.

Most of the investigations on heat transfer in metal foams have been performed with air, due to the high pressure drop associated with liq-

uids. We present in the following the few studies dealing with liquid flow. Boomsma and coworkers (Boomsma and Poulikakos [23, 24], Boomsma, Poulikakos and Ventikos [25], Boomsma, Poulikakos and Zwick [26]) investigated the effective thermal conductivity of fluid-saturated metal foams and their applicability for heat exchangers. The effect of compression of commercial metal foam on the flow characteristics is addressed in Boomsma and Poulikakos [24] and Boomsma, Poulikakos and Zwick [26]. In these studies, an increase in the Nusselt number was observed for higher compression factors up to a certain state of compression, where the heat transfer rate again decreased. The thermal resistances of compressed open-cell aluminum foam heat exchangers were found to be lower by a factor of 2-3, compared to commercially available heat exchangers. The thermophysical properties of high porosity metal foams have also been investigated by Bhattacharya et al. [16]. A model to predict k_{eff}, based on a two-dimensional array of hexagonal cells was validated with experiments using air and water flowing through aluminum and reticulated vitreous carbon (RVC) foams. Phanikumar and Mahajan [116] present numerical and experimental results for buoyancy-induced flows in high porosity metal foams heated from below. They found significant enhancements in heat transfer up to a factor of about 16 for an Al-water system.

Solid material: The choice of the material for a chemical reactor is not only critical in terms of corrosion but also with respect to the heat transfer performance. Boomsma and Poulikakos [23] concluded that for fluid saturated metal foams in which the thermal conductivity of the solid is markedly higher than the fluid conductivity (about 3 orders of magnitude), improvements in the overall effective thermal conductivity are best made by increasing the thermal conductivity of the solid phase. The solid material affects the heat transfer towards the reactor wall and therefore the steady state temperature of the foam during operation. This effect is well described by Edouard et al. [41]. They present a comparison of experimental and numerical results of the radial and axial temperature profiles in gas flow trough different porous media with circular cross sections. For example, the results of a polyurethane foam (PU) are compared with silicon carbide (SiC) foam with the same morphological structure. Due to the significantly reduced radial effective thermal conductivity, the temperature observed in the tube center is much smaller

in case of PU compared to SiC, when heat is applied externally. They also illustrate that novel materials like SiC or graphitic foams could be applied which exhibit higher effective thermal conductivities than metal foams to further increase the heat transfer performance. Sultan et al. [148] investigated the heat transfer enhancement by bonding layers of graphitic foam to a heated metal substrate. Convective enhancements of $30 - 70\%$ were observed for air flows ranging from $7 - 11\,\mathrm{m/s}$ and foam thicknesses from $2 - 10\,\mathrm{mm}$. The application of such novel materials opens new fields of applications e.g. in jet engines. Azzi et al. [8] present the idea to homogenize the temperature between the combustor and the turbine section of a turbojet engine by means of Aluminum (Al) foam to raise the overall efficiency. The efficiency of the open cell metal foams provides a temperature homogenization on a scaled-down temperature profile at a comparable small pressure drop of less then $14\,\mathrm{bar/m}$. But obviously, Al is not a suitable material for use in this very high temperature environment and an alternative approach is needed.

Porosity: Bhattacharya et al. [16] conclude that the effective thermal conductivity strongly depends on the porosity. One can assume by considering Eq. 2.2 that the thermal conductivity increases with decreasing porosity since solid materials generally have much higher thermal conductivities than fluids. Different investigations support this conclusion. Shih et al. [136] found that the pseudo convective heat transfer increased with decreasing porosity and this was attributed to an enhanced interstitial bulk velocity and an increased k_{eff}. An increase of k_{eff} with decreasing porosity was also observed by Pavel and Mohamad [110] who studied the effect of metallic porous media on the heat transfer rate by means of metallic screens inserted into a tube. Zhao et al. [167] performed investigations with metal foam under vacuum conditions, and observed the same trend.

Pore size and ligament thickness: The pore size defines the size of the smallest channel in the porous media. This is the characteristic length-scale for the Reynolds number and presents the maximum fluid velocity. Boomsma and Poulikakos [24] found that decreasing the pore diameter at constant porosity leads to reduced permeability and an increase in the form coefficient resulting in a higher pressure drop. Apart from this obvious influence, the pore size is also critical for convective heat transfer. On the one hand, the specific surface area of foam increases with

decreasing pore size. This leads to an enhanced heat transfer surface and therefore in the case of natural convection, an increased pseudo convective heat transfer coefficient. This was observed by Mahdi et al. [96] who found a reduction in the heat resistance of more than 70% for aluminum-foam CPU heat exchangers compared to commercial heat sinks. On the other hand, the pore size of commercially available foam is coupled with the thickness of the ligaments. By decreasing the pore size, the ligament diameter of the solid material decreases which affects two heat transfer mechanisms. Firstly a reduction in heat conduction occurs through thin struts. For this reason, Zhao et al. [167] observed under vacuum conditions a reduced k_{eff} with decreasing pore size. Secondly, thicker ligaments induce more turbulent kinetic energy, as we present in this study, leading to an enhanced convective heat transfer. Bhattacharya and Mahajan [17] studied the effect of air flowing through metal foam for a wide range of pore sizes (5, 10, 20, 40 ppi). A five to six times higher heat transfer coefficient was found for the metal foam heat sinks compared to a heated surface. At constant porosity the heat transfer rate was found to be higher at lower pore densities, which corresponds to thicker ligaments. We assume that the interplay of the variables affecting the heat transfer, i.e. the specific surface area and the ligament diameter, leads to an optimum in pore size depending on the application. For example Hackeschmidt [61] investigated metal foam for applications in air conditioning, heat exchange and cryogenic engineering and employed metal foam from m-pore GmbH (same type of foam used in this study). The best heat exchange performance was obtained for metal foam with a pore size of 20ppi.

Ligament shape: In contrast to the ligament diameter in commercially available foams, which is coupled with the pore size, the shape of the ligaments is partly controllable by varying the porosity. Applying the established manufacturing method for commercial metal foam, the cross section of the ligament becomes more triangular the higher the porosity of the foam is. Previous studies of Hackeschmidt [61] and Bhattacharya and Mahajan [17] confirm that a triangular cross section is favorable for heat transfer. Heat transfer increases with increasing porosity for a given pore size (meaning for a distinct triangular shape of the ligaments). We show in this study that the turbulence is enhanced in porous media with triangular shaped ligaments compared to circular ones leading to

an enhanced convective heat transfer coefficient.

Specific surface: The high specific surface area and the high porosity of metal foams is favorable in terms of heat transfer as already mentioned above. But these properties are also interesting for other applications. Giani et al. [58] evaluated the use of metal foams as catalyst supports in gas-solid catalytic processes with short contact times and high reaction rates typically controlled by diffusive mass transfer. The developed Nusselt correlation $Nu = Re^{0.43}Pr^{\frac{1}{3}}$ satisfies the Colburn analogy with the correlation for mass transfer coefficients derived in a previous investigation (Giani et al. [59]) for very low Reynolds numbers ranging from 20 to 240. Therein the Reynolds number is defined with the equivalent diameter of the strut. By increasing the strut diameter an increased Nusselt number is observed, which is consistent with the literature results presented above.

Reactor Geometry: Different researchers studied the influence of geometrical aspect ratios of metal foam elements on the heat transfer efficiency. An investigation on the effect of the height to diameter ratio of heat sinks was performed by Shih et al. [136] by varying this value from 0.92 to 0.15. An air jet was blown into the porous media from the top towards a waste-heat generation block on which the metal foam was installed. The estimated Nusselt number of aluminum-foam heat sinks was found to first increase and then decrease. The increase is caused by the increased percentage of the cooling air reaching the top surface of the waste-heat generation block, resulting from the reduced flow resistance. The decrease in the Nusselt number is ascribed to the reduction in the heat-transfer area between the cooling air and the solid phase of the aluminum-foam heat sink. Salas and Waas [130] investigated the size effect of the metal foam core in aluminum metal foam sandwich panels. Similar to the measurements of Shih et al. [136], the experimental results show that larger foam thicknesses produce increased heat transfer levels, but this effect diminishes for thicker foams. One assumes that there is an optimum thickness given by the heat conduction towards the wall and the specific surface area delivered by the foam. We recommend a circular cross section since the distance to the reactor wall is minimized at every location in the cross section. This assumption is further supported by the results of Kurtbas and Celik [88]. They investigated the mixed convection flow through a horizontal rectangular channel with

metal foam inserts. All boundary surfaces were heated and the length of the test section was kept constant at 62 mm. A decrease in the mean Nusselt number was observed as the cross sectional aspect ratio changed from 1 to 0.25.

Wall connection: Hackeschmidt [61] found that the method of wall connection significantly impacts the total heat transfer rate. Different methods like gluing and soldering or novel casting processes were tested. Soldering was found to be the most efficient method: the heat transfer rate was around 3 times higher compared with no connection. However, soldering is time-consuming and expensive and for this reason is hard to apply to industrial manufacturing processes.

2.3.4 Gas-liquid flow

Flow studies

Only few publications were found dealing with gas-liquid flow through solid foams, given that in the majority of the cases gas reactions were studied. Topin et al. [150] investigated liquid, gas and mixed flow in metallic foams. The stationary pressure profile was measured over the test section for copper and nickel foam of pore sizes ranging from 10 to 100 ppi. The liquids used were air and water. The permeability and inertial coefficient were evaluated according to the Forchheimer model. For single phase flow the heat transfer coefficient was improved by two orders of magnitude with the presence of metallic foam at a comparable small increase of the pressure drop. Also in the investigated convective boiling regime (two-phase flow) a significant heat transfer improvement and very low pressure drops were observed. In addition the superheat at the onset of boiling was observed to be reduced with inserted metal foams. Various other studies were performed at the laboratory of Chemical Reactor Engineering at the Eindhoven University of Technology. In Stemmet [141] hydrodynamic parameters such as liquid hold up, pressure drop, and flow regimes similar to those for packed beds, have been obtained for the gas and liquid flows through solid foam packing with pore sizes ranging from 5-40 ppi. It was found that foam is excellent for gas-liquid counter-current applications with its high surface area and high porosity. In Stemmet et al. [146] experimental results of the liq-

uid holdup and gas-liquid mass transfer characteristics are compared to modeling results. Aluminum foams of 5-40 ppi within a semi-2D transparent bubble column were used for the experiments. Counter-current flow was investigated with maximum gas and liquid velocities of 0.8 m/s, respectively 0.03 m/s. In the low and the high liquid holdup regimes the holdup could be accurately described by the relative permeability model proposed by Saez and Carbonell [129]. In Stemmet et al. [142] the co-current up- and down-flow in solid foam packing of 10-40 ppi are investigated. The influence of the liquid viscosity and surface tension was studied and the gas liquid mass transfer was correlated to the fluid velocity and the Schmidt number by two different correlations (Fukushima and Kusaka [53], Sherwood and Holloway [135]) for the up- and down-flow case. In Stemmet et al. [144] the application of UV-Visible and Raman Spectroscopy is proven for the use in a slurry of particles and a packed bubble column. The disturbance in the UV-Vis and Raman spectra resulting from the bubbles could be successfully removed by a newly developed tolerance-and-averaging method. The study indicates that in situ UV-vis and Raman spectroscopy can be used to characterize solid surfaces operating under multiphase conditions. The UV-Vis measurements and the tolerance-and-averaging method is explained again in detail in Stemmet et al. [145]. Bonnet et al. [22] performed experiments for co-current flow of a water-air mixture on $5 - 20$ mm thick foam samples. They analyzed the results and describe different flow patterns by means of the homogeneous phase Lockhart-Martinelli approach or the separated phases approach to model two-phase flow in the foams. Edouard et al. [42] measured the residence time distribution and quantified, based on this data, the pressure drop and liquid holdup in solid SiC foams under co-current trickle flow conditions. Like Stemmet et al. [146] he used the relative permeability model of Saez and Carbonell [129] to correlate his data. Calvo et al. [29] performed a hydrodynamic study on gas-liquid counter-current flow in a packed (Ni-CR foam) rectangular column ($40cm \times 40cm \times 2cm$), and measured liquid holdup with increasing gas flow rates by means of 2D x-ray radiography. Local values of porosity and pore diameters are measured on a foam sample 3D image, obtained with a micro-CT system. The results agree well with manufacturer data. Gerbaux et al. [54] investigated single- and multiphase flow through thin nickel foams (thickness: $1.5mm$) in terms of

pressure drop to determine the hydraulic parameters. For two-phase flow only gas phase relative properties are estimated through a generalized Darcy-Forchheimer equation. The results show the importance of inertial effects.

Multiphase flow characterization by wire mesh sensor

An overview on the different measuring techniques is shown by Boyer et al. [27]. They conclude in their review that the multiphase flow characterization is very complex because of the diversity in nature of the different possible phases and the resulting different flow regimes. The most recent non-invasive spatially resolved techniques known from single-phase flow (i.e. particle image velocimetry) are very hard to apply or even useless in most of the cases. In addition most of spatially resolved techniques suppose optical access. Alternative methods like x-ray or γ-ray technologies deliver only time averaged data or the newest technologies in this field (i.e. Bieberle et al. [18]) are very expensive and complex in terms of construction. For this study we therefore decided to implement a method called wire mesh tomography. The device is an electrode-mesh tomograph developed for the high-speed visualization of transient gas fraction or tracer distributions in two phase flows in pipes. It consists of two electrode planes with n parallel wires each. This results in $n \times n$ sensitive points which corresponds to the spatial resolution of the device. The two planes of wire grids are placed into the flow in a short distance from each other. The angle between the wires of both grids is 90 degrees. The wires of the first plane (transmitter plane) were supplied with pulses of a driving voltage. If the pulse, given to one of the transmitter wires, arrives at a certain wire of the second plane (receiver plane), it is assumed that the crossing point between the two selected wires is occupied by the conducting phase (water).

The first wire mesh sensor (WMS) was build by Johnson [74] to detect the volumetric fraction of water in crude oil. Two wire grids orthogonal to the flow direction are mounted in a circular tube with a short distance to each other. The grid upstream acts as transmitter the one downstream as receiver. The grids are rotated 90 degrees against each other forming a mesh with a plurality of node points. The transmitter wires are supplied with a voltage one after each other. The instantaneous volume

fraction of the conductive medium in the flow was estimated by relating the number of nodes with a significant current signal to the total number of nodes. This method results in a global information on the volume fraction but does not deliver any information about the local and temporal distribution of one medium within an other. By activating the receiver wires consecutively the temporal resolution is rather low. Reinecke et al. [126] developed the first tomography sensor design to detect the composition of multiphase flows. The sensor consists of three wire mesh planes which are twisted by an angle of 60 degrees around the axial direction to each other. Conductivity is measured between parallel wires in the same plane resulting in a projection of the conductivity distribution in direction of the wires. To reconstruct an image of the flow tomographic image reconstruction has to be applied which is the bottleneck of this method as it is very time consuming. Nevertheless the sensor provides a temporal resolution of 112 fps and a spatial resolution of 2 mm. Prasser et al. [122] present an electrode-mesh tomograph for gas liquid flows which has a high temporal (1024 fps) and spatial (1.5 mm) resolution for transient void fraction measurements. The device measures the conductivity in the space between two parallel mesh planes and therefore avoids the complicated image reconstruction in comparison to Reinecke et al. [126]. Prasser et al. [122] compared the device with a γ-ray densitometer (accuracy specified with 1%). The wire mesh sensor produced a positive systematic error of 8% for the measured average volumetric gas fractions with respect to the reference measurements which is an acceptable value. Meanwhile the temporal resolution of the device has been increased to 10000 fps by simply improving the electronics. This value exceeds by far the possibilities of the fastest non-intrusive methods available. Based on the concept of Prasser et al. [122], Hampel et al. [63] managed to construct a sensor for a pipe diameter of $D = 8mm$ for a mixing chamber of an effervescent atomizer. Two mesh planes consisting of 16 wires were placed orthogonal to the flow direction with an axial displacement of $350\mu m$ to each other. The distance of the wires which exhibit a diameter of $50\mu m$ was $500\mu m$. Hampel et al. [63] stated that the measurement of the void fraction is in their case limited by the invasive nature of the sensor due to its high resolution and the resulting small distance in between the wires.

2.4 Modeling approaches and flow regimes

Motivated by the use of metal foams in heat exchangers, various flow simulations have been performed over the last decade to predict flow and heat transfer in foams. Figure 2.3 depicts an overview of the geometries discussed in this section. Boomsma, Poulikakos and Ventikos [25] simulated the flow of water through a well defined foam structure, where the unit cell of the foam structure is a tetrakaidecahedron. A steady periodic open-cell simulation was used, i.e. an infinitely large matrix of the defined foam structure was modeled by using periodic boundary conditions. The periodic unit consists of eight cells and the Reynolds number, based on the pore size d_p of the tetrakaidecahedron, was 170. Pressure drop data of the simulation were compared to experimental results and the resulting discrepancy of 25% between simulation and experiment was attributed to non-captured wall effects in the simulation, which results in a decrease of the predicted pressure drop. Krishnan et al. [83] carried out a direct numerical simulation (DNS) in a periodic open-cell metal foam structure. The computational domain consists of a single cell with a body-centered-cubic (BCC) structure assuming a spherical shape of the cell. In addition to the momentum transport heat transfer was also implemented in the calculation. The simulations were accomplished at a Reynolds numbers below 100 using water and air as fluids. The computed effective thermal conductivity, pressure drop, and local heat transfer coefficient values compared well with the existing experimental measurements and semi empirical models for porosities greater than 94%. Annapragada et al. [4] performed a DNS of flow and heat transfer in three different deformed, unit-cell foam geometries depicted in Figure 2.3. A model was developed coupling the structural deformation with fluid flow and heat transfer computations. The investigated Reynolds numbers based on the permeability were in the range of 0.01-10. Therefore the flow was simulated under laminar and steady conditions. Krishnan et al. [82] addressed fluid flow and heat transfer in open-cell metal foams by implementing several unit-cell geometries. The Reynolds number used the permeability as characteristic length and was in the range of 0.01-10. Effective thermal conductivity, pressure drop,

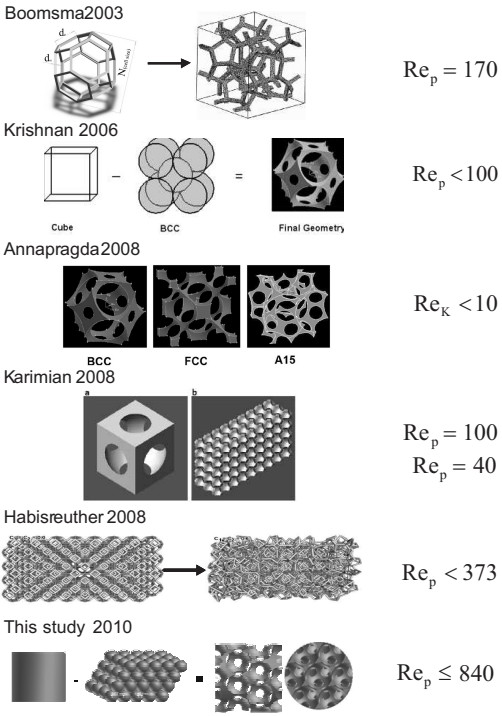

Figure 2.3: Literature overview of different geometry approaches and Reynolds numbers investigated

and Nusselt number were computed for aluminum foams saturated with air or water. The computed values compare well with existing experimental measurements and semi empirical models for porosities greater than 80%. Karimian and Straatman [77] carried out a laminar flow simulation in an idealized foam. The geometry consisting of a sphere-centered cube is slightly different to the others presented here and was already proposed by Yu et al. [165] to characterize the internal structure of graphitic foam. The investigated Reynolds numbers were 40 and 100 respectively. Based on the simulation results semi-heuristic models for pressure drop and heat transfer were developed. Habisreuther et al. [60]

used a random structure, which is based on tetrakaidecahedrons. The laminar flow was simulated in this structure and a scanned ceramic foam in a range of Reynolds numbers in between 3-373. Pressure drop data of the randomized structure were compared to experiments with commercial ceramic foam showing a huge deviation in pressure drop whereas the computational results of the magnetic resonance imaging (MRI) scan were in good agreement with the experiments. Another approach of the MRI technique is demonstrated by Von der Schulenburg et al. [154]. The scan provides simultaneously the 3-dimensional pore-scale velocity and the microstructural data for a polyurethane foam saturated with water. The effect of foam compression on the flow field was investigated by a Lattice Boltzmann (LB) flow simulation and the results were compared to experiments. This comparison showed that the LB technically was successful in modeling this effect. Tabor et al. [149] applied another imaging technique to provide the structural data of a plastic foam. They performed steady-state laminar flow computations within a micro-CT scan of a foam sample. For the investigations performed at Reynolds numbers up to 35 based on an equivalent particle diameter, the pressure drop was found to correlate with the flow speed in the appropriate manner. Another simulation using periodic boundary conditions was performed by Xu et al. [164], where the geometry consisted of 18 tetrakaidecahedron unit cells and the flow was computed for an incompressible Newtonian fluid at steady state condition at a Reynolds number of 250. In this study permeability, inertial coefficient and friction parameters were investigated. As stated above, most of the simulations in foam-like structures found in literature were performed in the laminar regime. For the rare turbulent cases mostly Reynolds-averaged Navier-Stokes (RANS) models were applied. But the transition region and the fully turbulent regime is not well investigated although it is of great interest for industrial applications and an open question is still the onset of turbulence. Pedras and de Lemos [111] distinguished 4 different flow regimes for general porous medias based on the available literature:

- Darcy or creeping flow regime ($Re_p < 1$)
- Forchheimer flow regime ($1 < Re_p < 150$);
- post-Forchheimer flow regime (unsteady laminar flow, $150 <$

$Re_p < 300$);

- fully turbulent flow ($Re_p > 300$).

where Re_p is the pore Reynolds number defined with the diameter of the open pores. A slightly higher critical Reynolds number was assumed by Horton and Pokrajac [72] who performed investigations on a matrix of spheres packed in a cubic arrangement at a pore Reynolds number of 370, which corresponds (according to their assumption) to the transitional region just before the onset of turbulence. Specific investigations of the transition to turbulence in solid foams were performed from two other authors. Hall and Hiatt [62] found a critical pore Reynolds number of 150 by LDA measurements of an exit air flow of a ceramic foam with pore sizes ranging from $0.8 - 2.5mm$. Seguin et al. [134] observed an onset of turbulence at pore Reynolds numbers around 400 depending on the pore size of the investigated foam. In addition it was observed that the velocity fluctuation increases at the same Reynolds number with increasing pore diameter, which is consistent with the findings of Hall and Hiatt [62].

Chapter 3

Theoretical consideration

In this chapter the fundamental theory is explained with respect to this study. The chapter is divided in four main topics. First the basic concepts of turbulent flow and modeling thereof are delineated. This is followed by the theoretical consideration of mass transfer in continuous reactors. In section 3.3 the heat transfer in pipes and through porous media is closer examined. In the last section the fundamentals of two-phase flow, i.e. the most important definitions for flow characterization and the different flow patterns in horizontal tubes, are presented.

3.1 Turbulence

3.1.1 Governing equations for turbulent flows

The nonlinear system of partial differential equations describing the motion in a newtonian fluid are called Navier-Stokes-equations, consisting of the conservation of mass ρ and momentum ρu_i.

$$\frac{\partial \rho}{\partial t} + \frac{\partial (\rho u_i)}{\partial x_i} = 0 \tag{3.1}$$

$$\frac{\partial (\rho u_i)}{\partial t} + \frac{\partial (\rho u_j \; u_i)}{\partial x_j} = -\frac{\partial p}{\partial x_i} + \mu \frac{\partial^2 u_i}{\partial x_j^2} + F_i \tag{3.2}$$

where p is the static pressure, F_i stands for an external force and μ is the dynamic viscosity of the fluid. Within this study simply water was used for all the experiments, which can be assumed as an incompressible fluid. In addition no external forces were applied in the investigated flow situation. Therefore the governing equations can be simplified to the following terms for an incompressible flow.

$$\frac{\partial u_i}{\partial x_i} = 0 \tag{3.3}$$

$$\frac{\partial u_i}{\partial t} + \frac{\partial (u_j\ u_i)}{\partial x_j} = -\frac{1}{\rho}\frac{\partial p}{\partial x_i} + \nu \frac{\partial^2 u_i}{\partial x_j^2} \tag{3.4}$$

where ν is the kinematic viscosity of the fluid.

3.1.2 Scales of motion

The rate of turbulent kinetic energy dissipation ε is coupled with the smallest scales in a turbulent flow. This follows the principle of the energy cascade described in detail in Pope [120]. Thereby one assumes that the kinetic energy is introduced into turbulence at the largest scales of motion and will be transferred consecutively to smaller scales. The dissipation of energy by viscous action takes then place at the smallest scales of turbulent flow which can be characterized by Kolmogorov scales defined as follows:

The length scale η

$$\eta = \left(\frac{\nu^3}{\varepsilon}\right)^{\frac{1}{4}} \tag{3.5}$$

The time scale τ_η

$$\tau_\eta = \left(\frac{\nu}{\varepsilon}\right)^{\frac{1}{2}} \tag{3.6}$$

and the velocity scale u_η

$$u_\eta = (\varepsilon\nu)^{\frac{1}{4}} \tag{3.7}$$

3.1.3 Modeling of turbulent flow

Simulations in porous media were widely studied for the laminar or low Reynolds number regime. A lot of studies are known working with macroscopic models which are in a lot of the cases only valid for the respective flow situations. Our interest on the simulation is the understanding of the flow within the structured porous media investigated. Therefore the flow has to be temporarily and spatially resolved. Different approaches to estimate the flow field in solid foams are presented in the literature listed in section 2.4. In most of the cases only a single cell or a small number of cells were investigated at low Reynolds numbers. In this study we investigate the turbulent flow through a periodic array of cells. A DNS is to expensive in terms of computational costs due to the high Reynolds numbers. RANS approaches on the other hand would have to be adapted to our flow situation. It is known from literature that in front of a stagnation point extremely high production rates of the turbulent kinetic energy are present by applying a standard $k-\varepsilon$ model. This nonphysical effect can be ascribed to the second derivative of the velocity in the kinetic energy source term. The comparison of a Large Eddy Simulation (LES) and the $k-\varepsilon$ model within a simplified porous media is shown in Kuwahara et al. [89] addressing the mentioned problem. In this work we apply therefore a dynamic LES to predict the flow field although it is very expensive in terms of computational costs and very sensitive on the mesh dimensioning.

Dynamic large eddy simulation

Based on the knowledge of the critical pore Reynolds number the flow was modeled for 3 different Reynolds numbers based on the empty tube diameter ranging from 1200 to 4500, where we observe turbulent flow. This corresponds to pore Reynolds numbers of 220 to 840 based on the pore size of the adapted geometry and the interstitial bulk velocity. In detail we performed a large eddy simulation with near wall modeling, where the larger three-dimensional unsteady turbulent motions are directly represented, while the effects of motion at smaller scales are modeled. This postulates the assumption, that the turbulence at the smallest scales is locally isotropic and can be treated properly from a statistical

point of view. A low-pass filter has to be applied to sort out the eddies which cannot be adequately resolved by the introduced grid of the simulation. In Fluent® the filtering operation is implicitly provided by the finite volume discretization. This is a usual approach which means that the filter width corresponds to the size of the grid. The modified filtered governing equations for the case of an incompressible fluid read

$$\frac{\partial \tilde{u}_i}{\partial x_i} = 0 \tag{3.8}$$

and

$$\frac{\partial \tilde{u}_i}{\partial t} + \frac{\partial \tilde{u}_j\, \tilde{u}_i}{\partial x_j} = \nu \frac{\partial^2 \tilde{u}_i}{\partial x_j^2} - \frac{1}{\rho}\frac{\partial \tilde{p}}{\partial x_i} - \frac{\partial \tau_{ij}^R}{\partial x_j}. \tag{3.9}$$

The filtered momentum equation (3.9) differs from the Navier-Stokes equation in the residual stress tensor defined as

$$\tau_{ij}^R = \widetilde{u_j u_i} - \tilde{u}_j\, \tilde{u}_i. \tag{3.10}$$

This term is analogous to the Reynolds stress tensor known from RANS modeling. It represents the stress at the subgrid scale which has to be modeled in order to achieve a closure of the equations 3.8 and 3.9 given that the term $\widetilde{u_j u_i}$ cannot be determined by the unmodified filtered governing equations. The residual stress tensor τ_{ij}^R and the residual kinetic energy $k_r = \frac{1}{2}\tau_{ii}^R$ are combined in the anisotropic residual-stress tensor which is defined as

$$\tau_{ij}^r = \tau_{ij}^R - \frac{2}{3} k_r \delta_{ij}, \tag{3.11}$$

where δ_{ij} is the Kronecker delta. The isotropic residual stress is also included in the modified filtered pressure $\tilde{p}$ as described in equation 3.12.

$$\tilde{p} = \widetilde{p} + \frac{2}{3}\rho k_r. \tag{3.12}$$

Dynamic Smagorinsky-Lilly model

In this simple approach first proposed by Smagorinsky [137] the linear eddy-viscosity model, given in equation 3.13, is used to calculate the

anisotropic residual-stress tensor τ_{ij}^r

$$\tau_{ij}^r = -2\nu_r \tilde{S}_{ij}, \tag{3.13}$$

where $\tilde{S}_{ij}$ is the filtered rate of strain

$$\tilde{S}_{ij} = \frac{1}{2}\left(\frac{\partial \tilde{u}_i}{x_j} + \frac{\partial \tilde{u}_j}{x_i}\right) \tag{3.14}$$

and ν_r is the eddy viscosity of the subgrid motions. Several models are available for ν_r. Here only the model used in this study, the dynamic Smagorinsky-Lilly model conceived by Germano et al. [55] and Lilly [92], is presented. In this approach ν_r is defined according to

$$\nu_r = L_s^2 \sqrt{2\tilde{S}_{ij}\,\tilde{S}_{ij}}. \tag{3.15}$$

In the dynamic Smagorinsky-Lilly model, implemented in Fluent® (*FLUENT 6.3 User's Guide* [50]), the dynamic Smagorinsky length scale L_s is defined by the minimum of the two products κd and $C_s V^{1/3}$ according to

$$L_s = min\left(\kappa d, C_s V^{1/3}\right), \tag{3.16}$$

where κ is the von Kármán constant, d is the distance to the closest wall, V is the volume of the computational cell and C_s is the Smagorinsky model constant. C_s is dynamically computed according to

$$C_s = \frac{M_{ij}L_{ij}}{M_{kl}M_{kl}}, \tag{3.17}$$

where L_{ij} is the resolved turbulent stress of the scales between the filter widths Δ and $\tilde{\Delta}$

$$L_{ij} = \widetilde{\tilde{u}_j\,\tilde{u}_i} - \tilde{\tilde{u}}_j\,\tilde{\tilde{u}}_i, \tag{3.18}$$

and M_{ij} represents the contribution of the modeled stress of these scales

$$M_{ij} = 2\tilde{\Delta}^2 \widetilde{\left|\tilde{S}\right|\,\tilde{S}_{ij}} - 2\tilde{\tilde{\Delta}}^2 \left|\widetilde{\tilde{S}}\right| \widetilde{\tilde{S}_{ij}}. \tag{3.19}$$

This dynamic procedure to obtain the Smagorinsky constant ensures correct near wall behavior of the turbulent viscosity which means no further wall damping functions need to be included.

Periodic boundary conditions

For our computational domain we have chosen a streamwise-periodic structure (SPS) with a constant translation length L. As we are interested in the fully developed flow regime without involvement of the entrance region we apply periodic boundary conditions according to Patankar et al. [109]. In this concept fully developed flows are not only restricted to constant cross sections, but also exist in periodically varying cross sections. Although it is originally formulated for the incompressible, laminar, steady, two dimensional case, it is assumed that this concept is also valid for the turbulent, unsteady, three dimensional case. This assumption was later proved by Pittard et al. [119] who investigated the correlation between the volume flow rate and flow-induced pipe vibration for turbulent flow. It is obvious that in our flow configurations, the conditions of a zero streamwise velocity gradient ($\frac{\partial w}{\partial z} = 0$) and zero normal velocity components ($u = v = 0$), which are valid for fully developed laminar flows in ducts with constant cross sections, cannot be fulfilled. The streamwise velocity w varies continuously with z and the radial velocity is only zero at the walls and at symmetry lines. However the velocity field repeats itself in a succession of cross sections that are separated from each other by the period length L. For periodic boundaries, according to Patankar et al. [109], the velocity and the pressure at any position can be written as

$$\mathbf{u}(x, y, z) = \mathbf{u}(x, y, z + L) = \mathbf{u}(x, y, z + 2L) = ... \tag{3.20}$$

$$p(x, y, z) - p(x, y, z + L) = p(x, y, z + L) - p(x, y, z + 2L) = ... \tag{3.21}$$

For the pressure drop another type of periodic boundary condition is applied in order to achieve a mass flow together with a decrease in pressure in positive z direction. The pressure can be decomposed by

$$p(x, y, z) = -\beta z + P(x, y, z). \tag{3.22}$$

This implies that the pressure drop per unit length is constant in z direction in which the term βz describes this global characteristic of the mass flow where β is a constant. The term $P(x, y, z)$ is related to the detailed local motions which are periodic in z direction. Consequentially

the prediction $P(x, y, z) = P(x, y, z + L) = P(x, y, z + 2L) = ...$ is valid which completes the description of the periodically fully developed flow.

Near-wall treatment

If the laminar sublayer is fully resolved by the applied mesh, the wall shear stress can be obtained from the laminar stress-strain relationship.

$$u^+_{lam} = y^+ \tag{3.23}$$

where u_τ is the friction velocity defined as $u_\tau = \sqrt{\frac{\tau_w}{\rho}}$ with the shear stress at the wall τ_w and y^+ is the dimensionless distance from the wall defined as

$$y^+ = \frac{u_\tau y}{\nu} \tag{3.24}$$

A fully resolved wall adjacent can mostly not be achieved over the whole computational domain and therefore another approach is used. When the centroid of the wall-adjacent cell falls within the logarithmic region of the boundary layer, the law-of-the-wall is employed.

$$u^+_{turb} = \frac{1}{\kappa} ln(Ey^+) \tag{3.25}$$

where κ is the von Kármán constant and $E = 9.793$. If the mesh is a such that the first near wall point is within the buffer region, then two above laws are blended according to Kader [75].

$$u^+ = e^{\Gamma} u^+_{lam} + e^{\frac{1}{\Gamma}} u^+_{turb} \tag{3.26}$$

where Γ is the blending function defined as.

$$\Gamma = -\frac{a(y^+)^4}{1 + by^+} \tag{3.27}$$

with $a = 0.01$ and $b = 5$. In order to fulfill the requirements for the above presented approaches the y^+ value was always kept small which means mostly below 5. The absolute highest values observed in the different cases are listed in the numerical results section in Table 7.1.

3.2 Mass transfer

3.2.1 Scales of mass transfer

In a general point of view the mass transfer in turbulent flow can be divided into macroscopic convection and a microscopic, diffusion driven molecular transport. Based on this mechanistic imagination the mixing process is often described as a combination of macro- and micromixing as described in Bockhorn et al. [20]. This approach makes sense to describe models or the time evolution of a mixing process but not to specify the quality of a mixture. Here one has to clearly distinguish between the different scales of mixing. The macroscopic state of a mixture cannot be compared to the microscopic one as both are related to each other. The dominant scale of mixing in a certain flow situation can be evaluated by the Batchelor scale (Batchelor [13]). This length scale describes how big a pure sphere of dye must be to diffuse in exactly the time it would take the energy in an eddy of the Kolmogorov length to dissipate.

$$\lambda_B = \left(\frac{\nu D_m}{\varepsilon} \right)^{\frac{1}{4}} \tag{3.28}$$

In analogy to the Kolmogorov scale providing a limit where turbulent stresses are balanced by viscous stresses, the Batchelor scale provides a limiting length scale where the rate of molecular diffusion is equal to the turbulent kinetic energy dissipation rate. The ratio of the Kolmogorov scale and the Batchelor scale is then equal to the square root of the well known Schmidt number Sc. The Schmidt number is defined as the ratio of the momentum and the mass diffusivity used to describe fluid systems wherein simultaneously convective mass transfer and molecular diffusion processes are observed.

$$\left(\frac{\eta}{\lambda_B} \right)^2 = Sc = \left(\frac{\nu}{D_m} \right) \tag{3.29}$$

For Schmidt numbers much smaller than 1 the molecular diffusivity is faster than the momentum diffusivity and therefore the smallest scales are in the velocity field. For a Schmidt number equal to 1 the scales are also equal and for Schmidt numbers much bigger than one the smallest

scales are in the concentration field meaning that the convective transport is the driving mixing process.

3.2.2 Characterization of radial mixing efficiency

The homogenization of different fluids is often accompanied by a fast chemical reaction. Although this mixing process is of great technical interest it is not fully understood yet. The correlation in between the convective transport of a scalar, the diffusive transport and the kinetic of the chemical reaction is not predictable. For the chemical reaction a complete homogenization on the molecular scale is of interest to avoid mass transfer limitations. The diffusion itself is only driven by concentration gradients meaning that the bulk concentration is a key parameter. A review by Baldyga and Bourne [10] shows that most of the developed micro mixing models make the assumption of a completely homogenized mixture from a macroscopic point of view. This assumption supposes an effective mixing unit which is, predominantly in continuous processes, difficult to realize. As the diffusion coefficients are given for defined temperatures and pressures only the convective mixing process can be influenced by changing the fluid dynamic in the system. This can only be done by changing the geometry of the static mixing device. It is obvious that a good convective mixing predicts by the Colburn analogy also a good convective heat transfer.

To characterize the efficiency of a static mixer, different terms are valid which are in most of the cases not comparable to each other. To understand the approach used within this thesis first one has to define the item mixing which is the distribution of different masses in a given volume, differing in at least one property like density, viscosity, color etc. The objective of the mixing process is the homogenization of those properties. For a continuous chemical plug flow reactor, where the length of the device pretends the residence time, the temporal mean concentration distribution of the educt over a well defined cross section is of major importance. A very good measure for the homogeneity of such a system is the theoretical variance as it is here unimportant if the deviation of the mean concentration is positive or negative. In this thesis the coefficient of variation (CoV) is used to describe the degree of mixing at the outlet of the different structures investigated, which is a standard term to

characterize the efficiency of static mixing elements. The CoV is defined as follows (Edward [43], Hiby [69]):

$$CoV = \frac{\sigma}{\langle \overline{c} \rangle} = \frac{\sqrt{\frac{1}{m} \sum_{i=1}^{m} (\overline{c}_i - \langle \overline{c} \rangle)^2}}{\langle \overline{c} \rangle} \tag{3.30}$$

where σ is the standard deviation of the spatial concentration from the average concentration of the observed cross-section and $\langle \overline{c} \rangle$ is the average concentration of the cross-section. The mean spatial and temporal concentration is defined as

$$\langle \overline{c} \rangle = \frac{1}{m} \sum_{i=1}^{m} \overline{c}_i \tag{3.31}$$

where m is the number of grid points for which the concentration was estimated.

3.2.3 Axial dispersion in porous media

To characterize the residence time that an element of fluid spends in a continuous plug flow reactor the theory of Danckwerts [34] is applied, which defines a probability distribution called exit age distribution $E(t)$ or more common residence time distribution (RTD). Since the RTD is a normalized function, the following constraint is always fulfilled:

$$\int_0^\infty E(t)dt = 1 \tag{3.32}$$

From the probability function $E(t)$ the volume fraction of the fluid elements of a continuous effluent stream that spent the time between t_1 and t_2 in the reactor can be calculated by the following integration:

$$\int_{t_1}^{t_2} E(t)dt \tag{3.33}$$

The mean residence time τ and the variance σ^2 are calculated according to Eq. 3.34 and 3.35.

$$\tau = \int_0^\infty tE(t)dt \tag{3.34}$$

$$\sigma^2 = \int_0^\infty (t-\tau)E(t)dt \tag{3.35}$$

Beside $E(t)$ the cumulative RTD $F(t)$ is often used in literature to compare the residence time of different systems. $F(t)$ represents the volume fraction of a continuous effluent stream, that was in the reactor less than the corresponding time t.

$$F(t) = \int_0^t E(t)dt \tag{3.36}$$

F(t) may also be seen as the probability that a fluid element entering the system at t = 0 has left the reactor within the time t.

Tracer pulse experiment

E(t) or F(t) can be determined by experimental methods using a physical or a nonreactive tracer. Therefore the concentration of the tracer is recorded at the inlet and the outlet of the reactor. It is required that the tracer does not disappear during the experiment (e.g., by selective adsorption on the walls of the reactor or on heterogeneous catalysts in a reactor, by settling out or being filtered out while it moves through the reactor, by chemical reaction). Two different types of tracer experiments can be applied. For the step experiment, presented by Hill [70], the tracer concentration at the inlet stream of the investigated reactor is changed instantaneously from one level c_0 to another c_1. In the ideal case the cumulative residence time distribution can be calculated by normalizing the measured concentration distribution of the tracer at the reactor outlet.

$$F(t) = \frac{c_{step}(t) - c_0}{c_1 - c_0} \tag{3.37}$$

For a tracer pulse experiment described by Levenspiel [91], which also used in this work, a defined amount of tracer is instantaneously injected into the inlet stream of a reactor. In the ideal case of a Dirac pulse the normalized recorded concentration distribution of the tracer in the effluent stream correspond to the residence time distribution $E(t)$.

$$E(t) = \frac{c_{pulse}(t)}{\int_0^\infty c_{pulse}(t)dt} \tag{3.38}$$

It is obvious that the real signals recorded never correspond to a Dirac pulse. At the inlet of the test section a broadened peak is observed. Hence a mathematical method has to be applied to compute the residence time distribution $E(t)$ described in the following section.

Deconvolution method

Mao et al. [99] applied an approach of deconvolution by the Fast Fourier Transformation (FFT) to analyze the tracer response to evaluate the residence time distribution from a tracer experiment. This method relies weakly on tracer response pretreatment, e.g. smoothing the data. Also Trachsel et al. [151] applied a deconvolution method using discrete Fourier transforms. The experimental data arose from an optical tracer pulse experiment in a micro channel by means of a piezoelectric injection. In another study by Lohse et al. [93] the axial dispersion of a tracer in a micro reactor was determined by means of optical experiments with a fluorescent dye. A novel method, using a caged fluorescent dye activated by a laser pulse, is compared to conventional optical measurement, where a tracer dye is injected into the investigated stream. It is concluded that the deconvolution method is not applicable in their case due to the weak signal to noise ratio. While for dispersion experiments the deconvolution is only seldom used due to its complexity the method is widely known in information technology. Especially the noise of signals in the frequency domain is well discussed and requires special treatment. Different filters are proposed by Bennia and Nahman [15], Mills and Dudukovic [100], Nahman and Guillaume [103] and Parruk and Riad [108]. In the following paragraph we describe our adopted deconvolution procedure: The inlet concentration signal $c_{in}(t)$ of an injected tracer is broadened while flowing through the reactor, which is characterized by E(t). If a reactor can be considered as a linear time-invariant system, $c_{out}(t)$ is given by

$$c_{out}(t) = \int_0^t c_{in}(t')E(t-t')dt \tag{3.39}$$

where $c_{out}(t)$ is the convolution of $E(t)$ and $c_{in}(t)$. Every flow system is linear according to Pippel [118], because it can be decomposed into either ideally mixed cells or cells with ideal plug flow behavior. The requirement of time invariance is fulfilled as the properties of the flow

system are time independent. Since the evaluation of E(t) from Equation 3.39 is not trivial, a transformation from the time domain to the frequency domain is implemented.

$$C_{out}(j\omega) = E_f(j\omega)C_{in}(j\omega) \tag{3.40}$$

Through this transformation the convolution has changed to a mathematical product and the residence frequency distribution $E_f(j\omega)$ can be obtained by

$$E_f(j\omega) = \frac{C_{out}(j\omega)}{C_{in}(j\omega)} \tag{3.41}$$

The inverse transformation of $E_f(j\omega)$ results in the residence time distribution E(t). The transformations and inverse transformations from the time to the frequency domain can be obtained by either Fourier transformations, Laplace transformations or Fourier series. Experimental data have to be treated by a discrete form of transformation since measurements are always discrete. The primary approach of a discrete transformation form is the Fast Fourier Transform (FFT) of Cooley and Tukey [32]. For a small signal to noise ratio $E_f(j\omega)$ becomes undetermined. A filter function in the frequency domain can reduce noise effects.

$$E_f(j\omega) = \frac{C_{out}(j\omega)}{C_{in}(j\omega)}F(j\omega) \tag{3.42}$$

In this work the Nahman-Guillaume Optimum filter is used recommended by Andrews [3]. It is a low-pass filter taking into account the spectral variations of the inlet concentration $c_{in}(t)$.

$$F(j\omega) = \frac{1}{1 + \frac{\lambda\omega^4}{|C_{in}(j\omega)|^2}} \tag{3.43}$$

where λ is a constant, $0 \leq \lambda < \infty$. The above mentioned regularization filter possess only a magnitude component and its performance depends on the value of the parameter λ. In this work λ is optimized for noise reduction to remove errors caused in the deconvolution processing. However the applied filter is not causal. Physical pulses which we also apply in our tracer pulse experiments, are causal functions of time, i.e. $f(t) = 0$ when $t < 0$. This fact postulates a causal residence time distribution, which is not given in case of applying a non-causal filter. Hence

the filter is modified by adding a phase component as proposed by Bennia and Nahman [15] who applied a complex mathematical algorithm to obtain the desired discrete minimum phase transfer function and the corresponding causal impulse response.

Axial dispersion model

According to Levenspiel [91] two models which are roughly equivalent are dealing with small deviations from plug flow: The axial dispersion model and the tanks-in-series model. These models can be applied to turbulent flow in pipes, laminar flow in very long tubes, flow in packed beds, long channels, etc. The axial dispersion model, often used to describe the RTD behavior in tubes, is also applied to solve the problem in this work. The model choice is based on the assumption of plug flow behavior within the metal foam, which was confirmed in the experimental study presented in section 6.2 addressing the flow through metal foam elements of different pore sizes. The governing equation of the axial dispersion model reads

$$\frac{\partial c}{\partial t} + u_b \frac{\partial c}{\partial z} = D_L \frac{\partial^2 c}{\partial z^2} \tag{3.44}$$

where z is the axial coordinate and D_L is the axial dispersion coefficient superimposed on the interstitial fluid velocity u_b. The axial dispersion coefficient is a characteristic term that accounts for mixing by molecular diffusion processes and by turbulent momentum transport in axial direction. The model assumes that the axial dispersion coefficient is independent of the position within the test section. Furthermore the tracer concentration c and the fluid velocity u_b is assumed to be constant across the tube diameter. Initial and boundary conditions have to be determined in order to solve equation 3.44. In this work the so called open boundary condition (Levenspiel [91]) was applied, which implies the same dispersion parameter characterizing the flow within and adjacent to the test section. This was achieved by a premixing zone consisting of metal foam. By further assuming a constant density the

solution of equation 3.44 according to Hill [70] is given below.

$$E(t) = \frac{1}{2\tau\sqrt{\pi\left(\frac{D_L}{u_b L}\right)\frac{t}{\tau}}} \cdot e^{-\frac{(1-\frac{t}{\tau})^2}{4\left(\frac{D_L}{u_b L}\right)\frac{t}{\tau}}} \tag{3.45}$$

where $\left(\frac{D_L}{u_b L}\right)$ is the vessel dispersion number and L is the length of the investigated media. A more common dimensionless number to describe the dispersion in porous media is the Peclet number shown in equation 3.46. Different definitions of the Peclet number are known from literature. In this study it is defined as

$$Pe_p = \frac{u_b d_p}{D_m} \tag{3.46}$$

where u_b is the interstitial bulk velocity and d_p is the pore size used as a characteristic length for the porous media according to Han et al. [64]. D_m is the molecular diffusivity of the tracer potassium chloride (KCl) in water at 20 °C.

3.3 Heat transfer - Forced convection in pipe flows

In order to estimate the convective heat transfer coefficient the complex combined heat transfer mechanism in metal foam is simplified to a standard heat transfer problem. For the derivation of the simple flow situation as depicted in Figure 3.1 the following assumptions are introduced:

- steady state
- incompressible fluid
- constant material properties (i.e. c_p, λ_s)
- axial heat transfer in the liquid is negligible
- homogeneous fluid temperature in a differential element

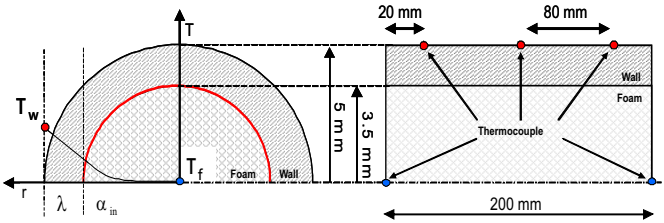

Figure 3.1: Schematic drawing of the experimental setup for heat transfer characterization. Three thermocouples are welded on top of the outer surface of the tube to estimate the wall temperature T_w. The bulk temperature of the fluid T_f is measured at the inlet and outlet of the test section in the center of the pipe.

- changes in the potential and kinetic energy of the fluid are negligible

In doing so, the energy balance for a differential fluid element with an axial length of dz can be written as:

$$d\dot{q}_h + \dot{m}c_pT_f - \left(\dot{m}c_pT_f + \dot{m}\frac{d(c_pT_f)}{dz}dz\right) = 0 \tag{3.47}$$

$$\Rightarrow d\dot{q}_h = \dot{m}c_pdT_f \tag{3.48}$$

Integration over the whole length of the tube leads to the first law of thermodynamics for the corresponding pipe.

$$\dot{Q}_h = \dot{m}c_p(T_{fout} - T_{fin}) \tag{3.49}$$

The energy $d\dot{q}_h$ transferred into the fluid can be described by a surface heat flux through a corresponding area $d_r\pi dz$.

$$d\dot{q}_h = \dot{q}''d_r\pi dz = \dot{m}c_pdT_f \tag{3.50}$$

Because of the change in the surface area of the tube wall in the radial direction, the specific surface heat flux increases with decreasing diameter. For the case of a heated pipe this heat flux results from

the temperature difference between the outer tube surface and the bulk temperature of the fluid. With the assumption of a homogeneous fluid temperature the following conditional equation for the fluid temperature with respect to the axial position can be derived.

$$\dot{m} c_p dT_f = d_r \pi dz k_r (T_w - T_f) \tag{3.51}$$

where k_r is the total heat transfer coefficient, consisting of a convective and a conductive heat transfer part corresponding to Figure 3.1. This coefficient can be defined with respect to the inner tube surface as follows:

$$\frac{1}{k_r} = \frac{1}{\alpha_i} + \frac{d_i}{2\lambda_s} ln\left(\frac{d_o}{d_i}\right) \tag{3.52}$$

where λ_s is the heat conductivity of stainless steel ($13\,\mathrm{W/(mK)}$) and α_i is the convective heat transfer coefficient inside the tube.

$$\alpha_i = \frac{1}{\frac{1}{k_r} - \frac{d_i}{2\lambda_s} ln \frac{d_0}{d_i}} \tag{3.53}$$

When a foam is inserted into the tube the same procedure can be applied to estimate the convective heat transfer coefficient. In this case we refer to a pseudo convective heat transfer coefficient that includes the heat transfer from the liquid to the porous structure and the heat conduction through the solid towards the reactor wall, as described in section 2.3.3.

3.4 Gas-liquid flow

3.4.1 Flow characterization

Multiphase flows are characterized by the presence of different phases with different densities and viscosities. An important specification is the fraction of the different phases. For gas-liquid systems the void fraction indicates the portion of the gaseous phase of the entire volume.

$$\varepsilon_V = \frac{V_g}{V_g + V_l} \tag{3.54}$$

Typically the different phases in a multi-phase flow system reveal different velocities. Generally the gas phase is faster then the liquid phase

in horizontal but also in vertical pipes. This difference in the velocities leads to a difference between the already mentioned void fraction and the volumetric transport fraction, which is defined as follows.

$$\dot{\varepsilon}_V = \frac{\dot{V}_g}{\dot{V}_g + \dot{V}_l} \tag{3.55}$$

The difference in the phase velocities is known as the slip velocity $u_s = u_g - u_l$. The ratio between the gas velocity and the liquid velocity is named slip.

$$s = \frac{u_g}{u_l} \tag{3.56}$$

By means of the slip one can interrelate the void fraction to the volumetric transport fraction in the following way. With the different phase velocities

$$u_g = \frac{\dot{V}_g}{A\varepsilon_V} \tag{3.57}$$

and

$$u_l = \frac{\dot{V}_l}{A(1-\varepsilon_V)} \tag{3.58}$$

one can depict the slip, where A is the cross section of the tube.

$$s = \frac{u_g}{u_l} = \frac{\dot{V}_g}{\dot{V}_l}\frac{A(1-\varepsilon_V)}{A\varepsilon_V} \tag{3.59}$$

By rearranging the equation 3.55 the ratio of the volumetric flow rates can be written as

$$\frac{\dot{V}_g}{\dot{V}_l} = \frac{\dot{\varepsilon}_V}{(1-\dot{\varepsilon}_V)} \tag{3.60}$$

This leads consequently to the following term for the slip.

$$s = \frac{\dot{\varepsilon}_V(1-\varepsilon_V)}{\varepsilon_V(1-\dot{\varepsilon}_V)} \tag{3.61}$$

For the sake of completeness the slip can also be written as a function of the mass transport fraction $\dot{x} = \frac{\dot{M}_g}{\dot{M}_g+\dot{M}_l}$.

$$s = \frac{\dot{x}}{1-\dot{x}}\frac{(1-\varepsilon_V)}{\varepsilon_V}\frac{\rho_l}{\rho_g} \tag{3.62}$$

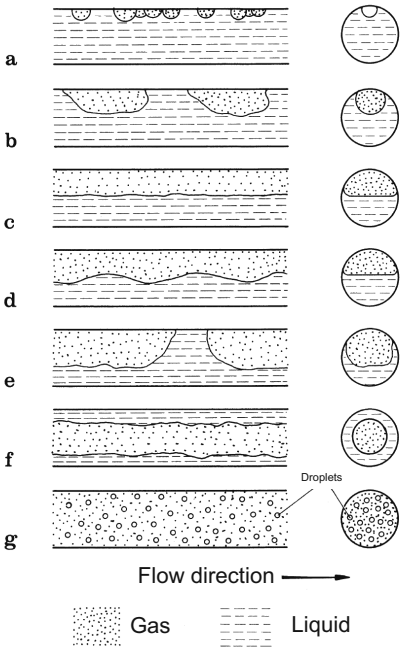

Figure 3.2: Flow patterns of a gas-liquid flow for an empty horizontal tube. a Bubble; b Plug; c Stratified; d Wavy; e Slug; f Annular; g Disperse

For the mean density over the whole considered domain, which is sometimes of interest, follows at the end

$$\langle \rho \rangle = (1 - \varepsilon_V)\rho_l + \varepsilon_V \rho_g \tag{3.63}$$

3.4.2 Flow patterns in horizontal tubes

Within preliminary results an air-water flow system is investigated in terms of gas fraction and phase distribution within a horizontal tube. We therefore focus in this chapter on gas-liquid flows. A comprehensive survey on the flow behavior and the description of multiphase flow is

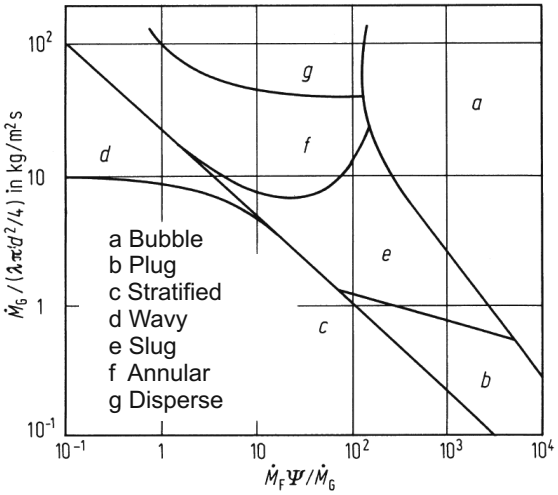

Figure 3.3: Flow chart for an empty horizontal tube according to Baker Baker [9].

given in Bohnet [21]. Depending on the ratio of the mass flow rates of the gas and the liquid phase different phase distributions are observed. The different flow patterns for an empty tube are depicted in Figure 3.2. For small gas fractions a bubble flow is observed. With increasing gas fraction the flow forces gain influence compared to the gravitational force. The flow pattern are changing to plug, stratified, wavy, slug, annular and disperse flow. The flow pattern for a horizontal empty tube case can be estimated by means of the flow chart according to Baker [9]. He introduced two characteristic numbers taking into account the different physical properties of the fluids.

$$\lambda = \left[\left(\frac{\rho_g}{1.2} \right) \left(\frac{1000}{\rho_l} \right) \right]^{\frac{1}{2}} \tag{3.64}$$

$$\psi = \frac{73 \cdot 10^{-3}}{\sigma} \left[\frac{\eta_l}{10^{-3}} \left(\frac{1000}{\rho_l} \right)^2 \right]^{\frac{1}{3}} \tag{3.65}$$

Near by the physical properties are referred to an air-water mixture meaning that the values in case of air and water are given by $\lambda = \psi = 1$. The flow chart clarifies that small changes in the flow ratios have a huge impact on the flow pattern. In most of technical gas-liquid application it is of importance to generate a huge interphase to increase the mass transfer over the phase boundary.

Chapter 4

Experimental methods

In this section the experimental setups are described. The basic facility is explained in section 4.1. Downstream this setup different test sections were installed to characterize the hydrodynamic, the mass transfer and the heat transfer of the compared reactor systems. Therefore a wide range of experimental methods were applied. The velocity distribution and the radial transport of an injected tracer were surveyed by means of optical methods described in section 4.2. Tracer pulse experiments with a salty aqueous solution were performed to investigate the axial dispersion explained in section 4.3. Calorimetric measurements finally complete the characterization of the single phase flow through the different reactor setups. In section 4.5 a relatively new concept to characterize multiphase flow systems is presented. It is a multiple electrode device consisting of two planes of wires. The device was miniaturized for our purpose and tested on liquid-liquid and gas-liquid systems.

4.1 Basic experimental facility

Exemplary a schematic drawing of the facility for optical measurements is shown in Figure 4.1, further explained in section 4.2. The basic experimental setup, as a part of it, consists of two pressurized vessels which are filled with deionized water respectively air. The reservoirs are con-

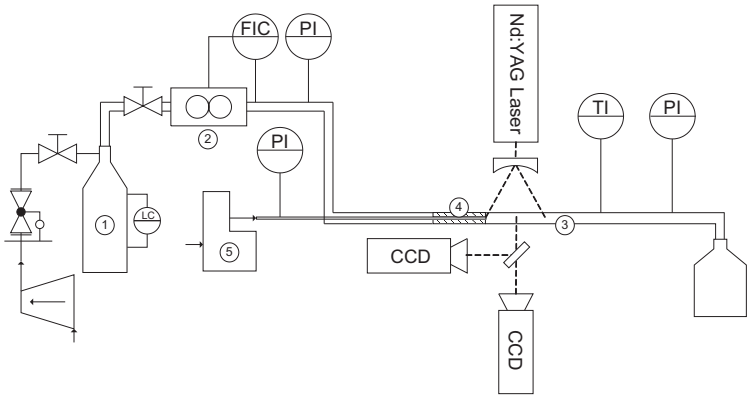

Figure 4.1: Flow chart of the experimental setup for optical measurements. The basic setup consists of two pressurized storage tanks (1) where only one is used in this case, a mass flow meter (2) and a piston pump. In the illustrated setup the main stream is flowing through a glass tube (3) with the inserted metal foam elements (4). The side stream (aqueous Rhodamine B solution seeded with hollow glass spheres) is conveyed by a piston pump (5). Pressure indicator (PI) and K-type thermocouple (TI) are installed to monitor the flow.

nected to the internal laboratory air supply which offers a maximum pressure of 7 bar. The tanks deliver the main stream which is controlled by a mass flow meter (Bronkhorst Hi-TecCORI-FLOW M55) or a gas flow controller (Brooks 5850 S) which can be monitored by a Personal Computer (PC). The pressure can be measured at maximum 5 different positions with pressure sensors of the type (Endress-Hauser Cerabar PMC131) and directly read out by the PC. Also the simultaneous gauging of 9 different temperatures is possible. For the side stream in the different experiments a piston pump (Harvard Apparatus, Standard Infusion PHD22/2000) is installed. It enables very stable conditions for small constant flow rates, i.e. up to 6 ml/min. The tubing downstream can be easily adjusted to the various conditions used for the different measurement series.

4.2 Optical measurement

4.2.1 Particle image velocimetry

Particle Image Velocimetry (PIV) is a nonintrusive optical measuring technique. The flow is seeded with small particles described in detail below. By passing a laser light sheet the particles scatter light (Mie-scattering) which is recorded by a CCD chip of a digital camera. The laser is pulsed and illuminates the sheet twice with a short delay resulting in two separate images. During this time the particles move with the fluid a certain length which should be in the order of 5 to 10 pixel. By a cross correlation of the two images the displacement of the single particles can be obtained. Therefore the area of interest is subdivided into smaller well defined so called interrogation areas wherein always one local displacement vector is determined. Assuming that the particles follow the fluid flow without interference the velocity field can be calculated by knowing the time delay between the laser pulses. In detail the image processing is subdivided into the following steps (Scarano and Riethmuller [133]; Scarano [132]): First a basic cross-correlation is applied and the resulting displacement field is locally filtered and interpolated. By the aid of the obtained predictor displacement field the two frames are deformed and interrogated with an adaptive cross-correlation. Again the field is filtered and the deformation process is repeated for a second adaptive cross-correlation. After filtering and interpolating the final velocity field was achieved. For all operations performed, an interrogation area of $32 \times 32 pixel^2$ was used to guarantee a seeding particle density of about 10 particles per interrogation area. For more detailed information on PIV we refer to Adrian [1], Westerweel [159] and Raffel et al. [123].

Tracer particles

The PIV measurements were performed with hollow glass spheres with the density $\rho_p = 1.03\,\mathrm{g/cm^3}$ and a particle diameter $d_p = 10\,\mu\mathrm{m}$. These properties fulfill the high requirements on tracer particles. The density of the glass spheres is nearly the same as the one of the test fluid water and they are therefore equally buoyant and move with the local fluid

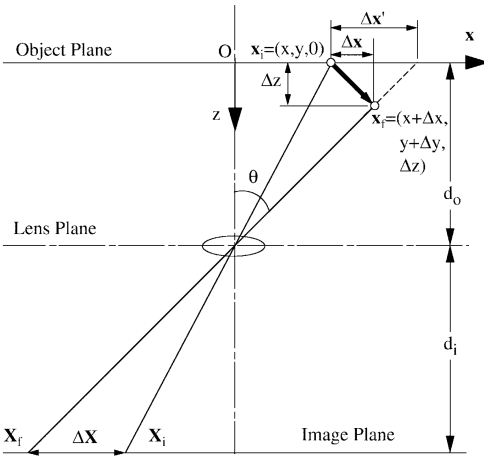

Figure 4.2: Schematic sketch of the single camera setup and explanation of the error caused by the particle movement out of the measurement plane.

velocity. The diameter of the particles is big enough to guarantee a good light scattering efficiency which is auxiliary affected positively by the spherical shape. In contrast they are small enough to represent the fluid motion as shown by Kuhn [86].

Laser sheet

A flashlamp-pumped dual Nd:YAG-laser provides the pulse light source for the sheet. The emitted green light has a wavelength of 532 nm. The light sheet is produced by a plano-concave cylinder lens and has a thickness of about 0.5 mm. The measurement of the velocity field takes place in the whole volume of the laser sheet. The scattered light is recorded by a single CCD camera with a pixel resolution of $1376 \times 1040 pixel^2$ equipped with a band-pass filter (passing light at 532 nm +/- 2 nm). In such a single camera setup the depth of the laser sheet leads to a certain measurement error, increasing with increasing motion of the

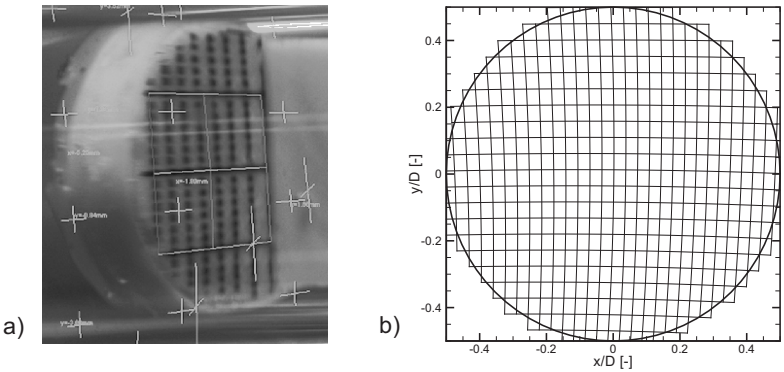

Figure 4.3: Inserted dot pattern in the glass tube (left) and resulting back counted mesh for an exemplary measurement (right).

fluid out of the plane as explained in Figure 4.2. A reduction of this error would be achieved by applying a stereoscopic PIV approach (e.g. Westerweel and Van Oord [160], Willert [162], Prasad [121]).

Spatial resolution

PIV measurements were performed in two different planes orthogonal to the axial and radial velocity. The interrogation area for the post-processing of $32 \times 32 pixel^2$ was kept constant for all the experiments. By knowing the size of the area of view (AOV) the resolvable length scale of PIV can be calculated backwards by a simple mapping method. Therefore dot patterns are inserted into the tube to scale the AOV. The plane orthogonal to the radial velocity was mapped linearly whereas for the other plane a perspective mapping had to be applied to count back the distortion. The inserted dot pattern a) and the resulting grid b) for the xy-plane are depicted in Figure 4.3. The average spatial resolution of PIV measurements is about 0.5 mm for the plane orthogonal to the radial velocity and for the cross section. This length has to be compared to the Kolmogorov scale, which was estimated by replacing the energy

dissipation rate ε in equation 4.1 by $\frac{U_b^3}{d_p}$ where U_b is the bulk velocity and d_p is the pore size.

$$\eta = \left(\frac{\nu^3}{\varepsilon}\right)^{1/4} \tag{4.1}$$

The Kolmogorov scale for the different investigated structures is, depending on the Reynolds number, up to two orders of magnitude smaller then the resolved length scale. It follows that the quality of resolved scales decreases with increasing Reynolds number and decreasing pore size of the investigated structure. However, the range of resolvable length scales is assumed to be sufficient to address turbulence phenomena in all studied cases in this thesis.

Accuracy and validation

The total deviation caused by this measurement method persists of two different kinds of errors. The first one comes from the image recording. As the distortion caused by the shape of the tube is reduced by the view cell, shown in Figure 4.7, the optical measurement system is comparable to the setups used by Kruse [84], Kuhn [86], Kuhn et al. [87] and Wagner [156], Wagner et al. [157]. Based on their findings and the information of the previous sections the error due to image recording is negligible and was estimated by Kruse et al. [85] to 0.01%. The second source of error is the post processing of the images whereat the spatial resolution is mainly responsible for the quality of the measurement. To test the resolution and the accuracy of the experimental setup, the axial velocity profiles for laminar and turbulent flow conditions were measured in an empty tube and compared with theoretical predictions. This comparison with literature is presented in Figure 4.4 for two Reynolds numbers, 600 and 4500. The laminar profile was calculated by the correlation of Hagen-Poiseuille, which is the solution of the simplified Navier-Stokes equation for an empty tube case with no slip condition at the wall:

$$\frac{\overline{w}}{U_B} = \frac{3}{2}\left(1 - \left(\frac{y}{R}\right)^2\right) \tag{4.2}$$

R is the inner radius of the tube (3.5 mm), y the radial position and U_B the bulk velocity measured with the mass flow meter. The turbulent

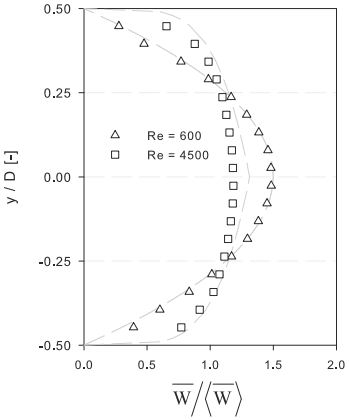

Figure 4.4: Measured velocity profiles (empty dots) of a laminar ($Re = 600$) and a turbulent ($Re = 4500$) case in comparison with analytical solutions (dotted lines).

velocity profile was calculated by the following equation Blevins [19]:

$$\frac{\overline{w}}{U_B} = \frac{(d+1)(2d+1)}{2d^2}\left(\frac{R-y}{R}\right)^{\frac{1}{d}} \tag{4.3}$$

d is equal to $f^{-0.5}$ and f is the dimensionless friction factor calculated from the smooth pipe law of Karman [78]:

$$\frac{1}{\sqrt{f}} = 2log\left(\frac{Re\sqrt{f}}{2.51}\right) \tag{4.4}$$

For the laminar case a very good agreement between analytical and experimental values was found. For the turbulent case the measured profile is slightly flattened compared to the theoretical prediction but still in good agreement. This difference can be explained by the used correlation, which is simplified in a way that the gradient at the pipe center does not go to zero, leading to a bulge effect. These preliminary measurements in the empty tube show that the system is delivering very accurate results with a high spatial resolution.

To characterize the turbulence induced by the metal foam time averaged statistics will be presented. In turbulent flows an instantaneous velocity $\mathbf{u}$ can be decomposed into the mean velocity $\overline{\mathbf{u}}$ at the certain position and the fluctuation part $\mathbf{u}'$ according to Reynolds [127].

$$\mathbf{u}' = \mathbf{u} - \overline{\mathbf{u}} \tag{4.5}$$

Based on this decomposition the root mean square of the velocity fluctuations averaged over the time of the experiment, i.e. the number of images n, is given by

$$u_{rms} = \sqrt{\frac{1}{n}\sum_{i=1}^{n}(u_i - \overline{u})^2} \tag{4.6}$$

Based on the fluctuations the turbulent kinetic energy k was calculated, defined to be half the trace of the Reynolds stress tensor Pope [120]:

$$k = \frac{1}{2}(\overline{u'u'} + \overline{v'v'} + \overline{w'w'}) \tag{4.7}$$

It is the mean kinetic energy per unit mass in the fluctuating velocity field. Since the PIV measurements only resolve two velocity components in the plane of measurement the radial velocity component was added twice to the turbulent kinetic energy term. This procedure is based on the assumption that the spatially averaged radial velocity is of the same order of magnitude in every plane rotated around the centerline. The overall mean velocity $\langle\overline{\mathbf{u}}\rangle$ is calculated from the measured 2-dimensional steady state velocity field:

$$\langle\overline{\mathbf{u}}\rangle = \frac{1}{m}\sum_{i=1}^{m}\overline{\mathbf{u}}_i \tag{4.8}$$

where m is the number of resolved data points in the area of interest with an axial extent of $2D$. The turbulent statistics for every velocity were calculated from a data set of 600 double frames. This number of images is huge in terms of the amount of data produced and stored but for an accurate statistical description of turbulent flow in the marginal range. However, the following closer examinations have shown that the

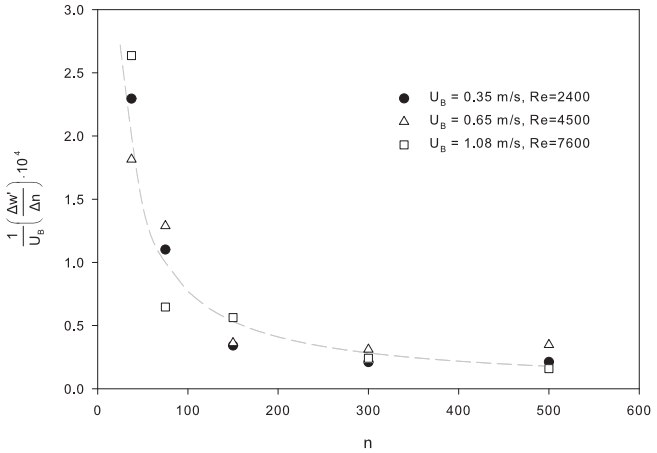

Figure 4.5: Difference quotient of the mean axial velocity fluctuation normalized by the bulk velocity versus the number of images analyzed behind a 20 ppi foam element.

error is very small and an acceptable quantitative statement about the different turbulent characteristics can be given. Figure 4.5 depicts the difference quotient of the mean axial velocity fluctuation normalized by the mean velocity versus the number of images analyzed behind a 20 ppi foam element. The field of integration has an axial extend of $2D$ downstream of the foam element. Only the turbulent cases are shown since for the laminar flow already with a small number of images very accurate steady state information were obtained. A strong decrease of the difference quotient with the number of images is recognized. The decay can be described by a power law. The very small change in the calculated absolute values of the fluctuations using 400 or 600 images was in the order of 1% and lead us to the assumption that 600 images are acceptable for the statistical description of the turbulent flow for the observed range of moderate Reynolds numbers.

4.2.2 Laser induced fluorescence

To characterize the mixing efficiency of the investigated plug flow reactors the concentration of a tracer dye (Rhodamine B) was recorded. Therefore planar laser induced fluorescence (PLIF) was applied. The fluorescent dye is excited by an Nd:YAG Laser with a wavelength of 532 nm. A part of this energy is absorbed and the other part is spontaneously re-emitted. The emitted light of the tracer is recorded by a CCD chip of a digital camera. The light intensity detected is proportional to the concentration of the tracer dye as described in equation 4.9 and can be calculated from the image by the help of a simple two point calibration at two different concentrations. The ratio of the total emitted energy per quantum of energy absorbed by a single molecule is the quantum efficiency ϕ. The energy emitted per unit volume is given by equation 4.9

$$I = I_0 \phi \varepsilon c \tag{4.9}$$

where c is the concentration of the tracer dye, ε the absorption coefficient and I_0 the incident light intensity of the laser. Inhomogeneous intensity distributions of the applied laser sheet can also be corrected by the calibration which is done pixel wise.

Laser

By performing PLIF one has to assure that the image generation time is smaller than the time scale for turbulent scalar mixing processes which is in the order of 10^{-6} s. Karasso and Mungal [76] showed, that the Nd:YAG laser is a suitable laser for the PLIF technique. The fluorescence emission of a typical tracer dye is less than 5ns thus the use of the pulsed Nd:YAG laser is justified. The two major drawbacks of using a pulsed Nd:YAG laser as light source are the inhomogeneities in the laser sheet and the pulse to pulse variation of the beam energy which is in the order of 1%. To overcome these problems a calibration function is generated corresponding to equation 4.9 for every single pixel of the CCD chip. Large ensemble averaged images were used to do so.

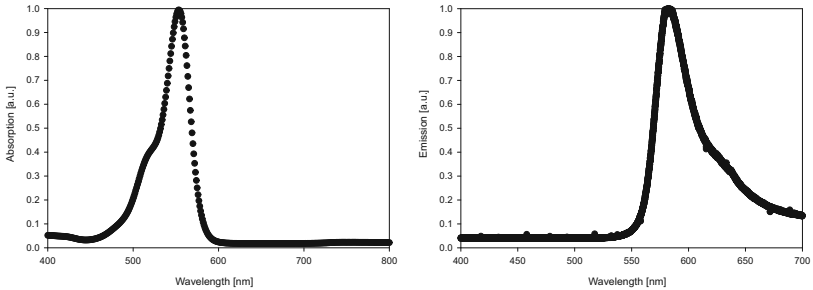

Figure 4.6: Absorption spectrum and the emission spectrum (excited with a Nd:YAG laser with a wavelength of 532 nm) of Rhodamine B

Tracer dye

The fluorescent dye used for the LIF measurement to investigate the scalar transport through the porous structures was Rhodamine B. For the characterization of the mixing behavior it is important to estimate the rate of molecular diffusion compared to convective scalar transport. This was achieved by calculating the Schmidt number which represents the ratio of momentum diffusivity (i.e. kinematic fluid viscosity ν) and the molecular diffusivity of a species D_m. In case of Rhodamine B the molecular diffusion coefficient D_m in water at 20 °C is $D_m = 3.6{\cdot}10^{-10}\,\mathrm{m^2/s}$ (calculated with the Wilke-Chang equation) which yields a Schmidt number of $Sc \approx 2800$. This means that the studied scalar transport phenomena are dominated by convective momentum transport rather than by molecular diffusion of the species. Thus the instantaneous concentration fields provide information about the mixing due to turbulent motion of the fluid. The absorption and emission spectra of Rhodamine B diluted in water are depicted in Figure 4.6.

Accuracy

The description of the mixing efficiency by 600 single frame images has to be challenged from a statistical point of view. It is known that the number of frames has an influence on the CoV (Hirschberg et al. [71], Wadley

and Dawson [155]), which is calculated by using time averaged concentration values. Initially the coefficient of variation, defined in section 3.2, decreases with the number of images due to the temporal fluctuations of the concentration caused by the periodic flow structures in the porous media. A stable value of the CoV has been reached for a frame number bigger than 100. With a data set of 600 frames a good basis is given to characterize the mixing efficiency of the system. Another important parameter is the resolution respectively the sampling size which is somehow limited by the data amount produced by exporting the single frames. With a length scale of the spatial resolution below 0.1 mm a good reproduction of the concentration field was achieved, leading to a stable CoV over the different experimental series. The influence of the pulse to pulse variation and the inhomogeneities in the laser sheet mentioned above was proven by measuring a fully homogeneous mixture. A CoV of 0.0085 was measured which fulfills the demand of literature defining a completely homogeneous mixture by a value of up to 0.01.

4.2.3 Simultaneous measurements

To quantify the mixing performance of different foam structures the experimental setup presented in Figure 4.7 and 4.8 was used. A pressurized vessel filled with distilled water provides the main fluid stream. The flow rate is controlled by a mass flow meter. It feeds the plug flow reactor which is used for the optical measurements, consisting of a glass tube with an inner diameter of $D = 7\,\text{mm}$. A capillary (outer diameter 1/16 inch) is fixed at the centerline of the tube by several fittings. Two metal foam pieces of 25 mm length are mounted around the capillary which is closed at the end. For the designed streamwise periodic structure made of plastic the capillary was inserted upstream the structure inlet. Two holes on opposite sides (separated by an angle of 180°) in the capillary in front of the different foams allow the injection of an aqueous Rhodamine B solution as tracer for concentration visualization. The constant flow rate of 6 ml/min is generated by a piston pump. The pressure drop was recorded by pressure sensors of Endress-Hauser installed at the in- and outlet of the test section. Combined particle image velocimetry (PIV) and planar laser induced fluorescence (PLIF) technique are applied to examine the spatial variation of the ax-

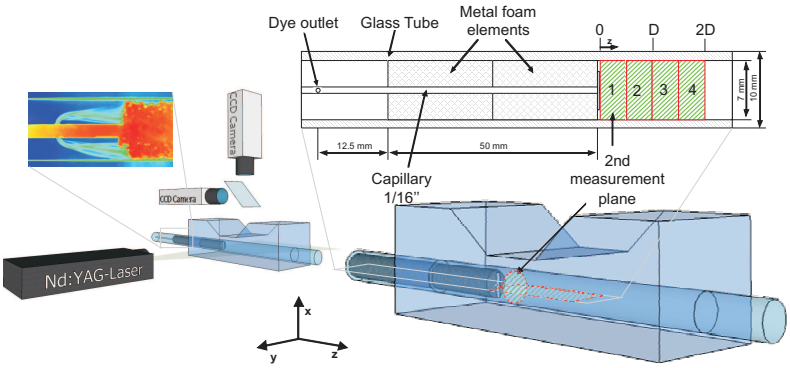

Figure 4.7: Schematic drawing of the experimental setup for PIV and PLIF measurements. The cameras are mounted rotatable to perform measurements in different planes. The view cell is filled with water to avoid optical distortion.

ial and radial velocity components and to assess the concentration field of the scalar. High-resolution CCD-cameras with a pixel resolution of $1376 \times 1040 pixel^2$ are used. A flashlamp-pumped dual Nd:YAG-laser provides the pulse light source for both. To enable the imaging of the same field of view for both cameras a dichroic mirror was installed. This beam splitter has a high transmittance at 520 nm and a high reflectance at 575 nm. The PIV camera is additionally equipped with a band-pass filter (passing light at 532 nm +/- 2 nm) and the LIF camera with a high-pass filter (cutoff below 540 nm) to completely separate the fluorescent emission from the Mie-scattering of the seeding particles. To perform simultaneous measurements the cameras, the laser and the image acquisition software were synchronized by means of an adjustable timing unit (PIV Synchronizer). For all the optical experiments an ensemble of 600 consecutive image pairs was acquired at a frame rate of 4Hz.

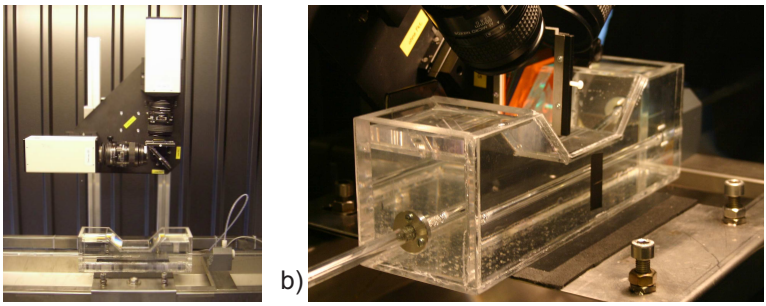

Figure 4.8: Image of the experimental setup. On the left the two cameras and the dichroic mirror are depicted mounted on a rotatable device. On the right the compensation box filled with water is shown to compensate the refraction

4.3 Conductive tracer pulse experiments

4.3.1 Experimental setup

For a detailed description of the system peripherals of the test facility we refer to section 4.1. A pressurized vessel filled with distilled water provides the main fluid stream, which is controlled by a mass flow meter. This stream is fed into the test section consisting of a stainless steel tube with an inner diameter of 7 mm and two different adaptable lengths of 1 m and 0.2 m depicted in Figure 4.9. The measurements can be performed in an empty tube reference case but also in a tube filled with metal foams of different pore sizes of 20 and 30 ppi. In addition, for the shorter tube arrangement the designed structured porous media is investigated. For the 1 m tube arrangement a constant side stream of 5 ml/min was injected via a tee connector in front of the test section. Using a 4-way-valve a tracer pulse (KCl-water) with a total volume of 0.1 ml can be generated. At the inlet and the outlet of the test section commercially available electrodes are installed to record the concentration. Difficulties were encountered when narrow RTDs were recorded with this device, which led to a huge standard deviation compared to our second measurement series in the shorter tube arrangement. For

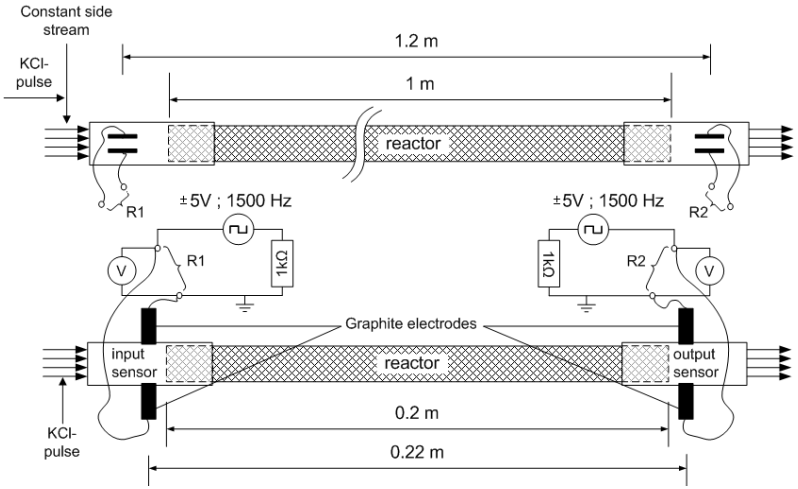

Figure 4.9: Experimental setups for conductive tracer pulse experiments with standard electrodes above and self made electrodes below.

that configuration the tracer pulse was generated by adding 0.3 ml of the tracer solution instantaneously to the main flow. The concentration was recorded by self made electrodes. The main advantage of the device was the increased measurement volume due to an increased distance between the electrodes by integrating circular graphite electrodes in the side walls. The data is collected by means of a measuring board of National Instruments (type: NI PCI6221) with a high temporal resolution of 250 kHz. A square wave voltage with an amplitude of ± 5 V is applied to the electrodes as depicted in Figure 4.9. The current conducted over the electrodes is measured as the response signal, which is detected as the voltage readout on the measuring board. This voltage is fitted with the corresponding salt concentration by a 4th degree polynomial. Therefore the concentration of KCL dissolved in water can be detected at the inlet and outlet of the test section.

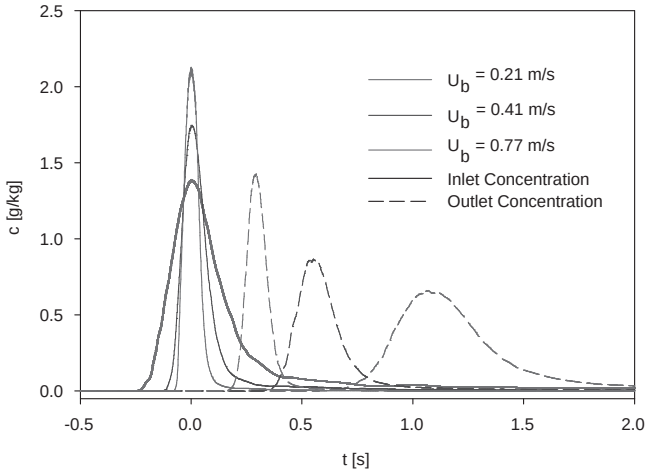

Figure 4.10: The inlet and the corresponding outlet concentration distributions of the tracer dye recorded by two electrodes placed at the entrance respectively the exit of the reactor. For a better representation of the data the time scale is cropped at 2 s whereas the data were recorded over a much longer time

4.3.2 Measurement procedure

At the beginning of the measurement the electrodes were calibrated in a continuous way by applying different KCL-water solutions with well defined concentrations. For every flow rate five different independent tracer pulse experiments were performed. A well defined pulse of a KCL-water solution was injected into the main stream and the inlet and outlet concentration was then recorded simultaneously. Figure 4.10 shows exemplarily for the short tube setup of the sintered structure typical experimental results of single tracer pulse experiments at 3 different interstitial bulk velocities. The presented data, recorded with a measurement frequency of 1 kHz, are smooth and have a high signal to noise ratio which is an important precondition for the postprocessing. One

can see that depending on the velocity the inlet pulse is already dispersed due to the injection and subsequent flow through the premixing zone. The broadening of the concentration peak is increasing with decreasing velocity. The five independent tracer pulse experiments were post processed by applying a deconvolution method described in section 3.2.3. The five estimated residence time distributions were then fitted with the dispersion model, where the axial dispersion coefficient D_L and the mean residence time τ were the free parameters.

4.4 Calorimetric measurements

4.4.1 Setup

The basic setup and system peripherals used for the experiments is further described in section 4.1. The virtual test section itself consists of a fully sintered tube with integrated porous media or an empty tube section which can be filled with commercial metal foam. Both tube devices have a length of 200 mm according to Fig. 3.1. Three thermocouples (K-Type, width 0.5 mm) are welded at an equal distance from each other, within nuts on the outer surface of the tube. One is placed in the middle of the tube and the others 20 mm away from the inlet and outlet which can be seen in Figure 4.11. On both ends of the tube, two T-junctions in series are attached at an angle of 90 degrees to each other to allow the simultaneous measurement of the temperature of the fluid in the center of the tube and the pressure. A heating cord (length 1.5 m) is wound around the tube with a maximum power release of 220 W. The system is insulated by a fiber glass insulation band. For the applied thermocouples an accuracy of $\pm 0.5\,^{\circ}\mathrm{C}$ can be assumed. The main flow (water) was generated by pressurized vessels and controlled by a coriolis force mass flow meter.

4.4.2 Measurement procedure

After setting the water flow rate, the setup was heated to steady state conditions, as indicated by a constant pressure drop and constant thermocouple temperatures. The temperature and pressure data were then recorded for 3 minutes. The three temporal mean temperatures of the

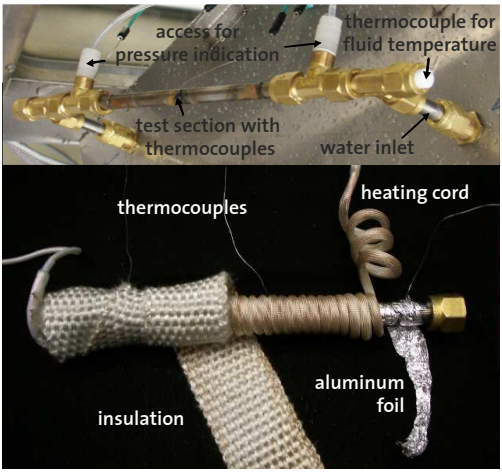

Figure 4.11: The experimental setup for calorimetric measurements installed without heating equipment (above) and dismounted with protective aluminum foil, heating cord and insulation (below).

outer wall showed a very distinct linear behavior, as depicted in Figure 4.12, for all Reynolds numbers investigated so that the wall temperature could be approximated by a linear regression. The fluid outlet temperature was then calculated by an iterative numerical method by discretizing equation 3.51 and varying the convective heat transfer coefficient until the deviation of the calculated value from the measured one was minimized. In this way, the total and the convective heat transfer coefficient from the five measured temperatures was estimated. The linear temperature behavior at the tube wall and the calculated temperature curve of the fluid flowing through the device are shown in Figure 4.12. The calculated temperature profiles are nearly linear and only minor differences were found through the evaluation of the data by using the logarithmic-mean temperature approach. To ensure reproducibility, measurements of the temperature profiles were repeated 5 times at a given set of conditions. The characteristics of the recorded temperature curves, presented in Figure 4.12, could be accurately reproduced, even

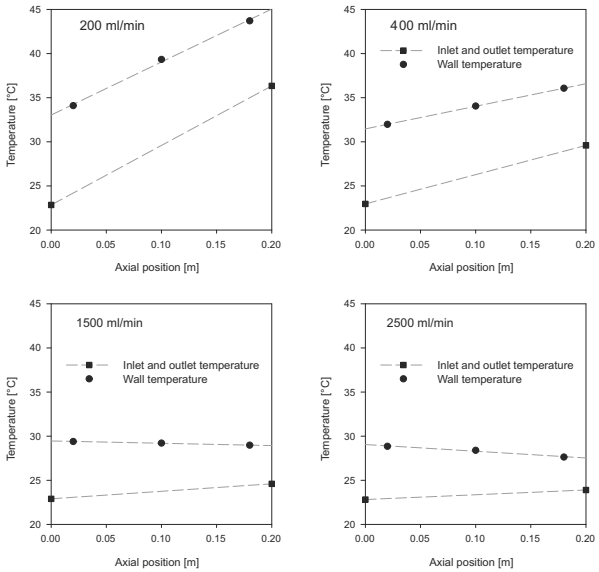

Figure 4.12: Example temperature profiles in the fully sintered structure for volumetric flow rates ranging from 200 to 2500 ml/min. Dashed lines indicate a linear regression for the wall temperatures and the calculated axial fluid temperature profile by discretizing equation 3.51.

when the fluid temperature was slightly changing due to the change in ambient temperature.

4.5 Wiremesh tomography

4.5.1 Mode of operation and accuracy

The measuring principle is based on the difference in conductivity of different phases. A schematic drawing of the device is depicted in Figure 4.13. It consists of two planes of parallel wires mounted orthogonal to

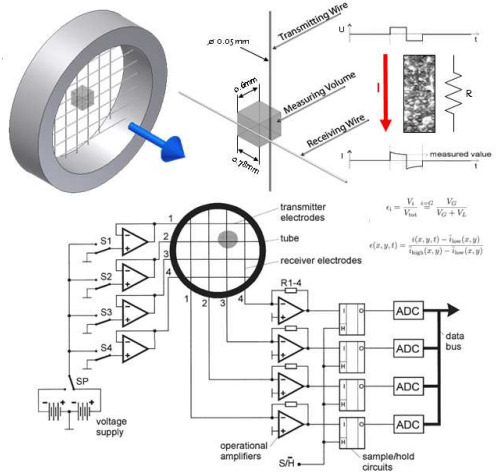

Figure 4.13: Schematic drawing of the sensor explaining the principal concept of the multi electrode device. The exemplary electronic circuit for a 4×4 wire sensor and the corresponding voltage signals are depicted.

the flow direction with a short distance to each other. The wires are rotated 90 degree against each other to generate a plurality of sensitive nodes. The wires upstream act as transmitters, the wires downstream as receivers. The transmitters are activated consecutively by closing switches S1 to S4. This is done by applying an alternating voltage (to avoid electrolysis) to these wires depicted exemplary in Figure 4.13 for a sensor with 4×4 wires. The voltage applied to a single transmitter evokes a current flow from the transmitter wire through the measuring volumes to the receiving wires. The operational amplifiers in the transmitter lines guarantee that all non-active wires are kept on ground to avoid any cross talk explained in detail in Prasser et al. [122]. The current arriving at the receiving lines is transformed into a voltage by the operational amplifiers and sampled by individual sample/hold circuits. The transient behavior of the current (I_{R3}) is caused by the capacitance of the electrodes, the ion layers in the liquid, and the cables. After an

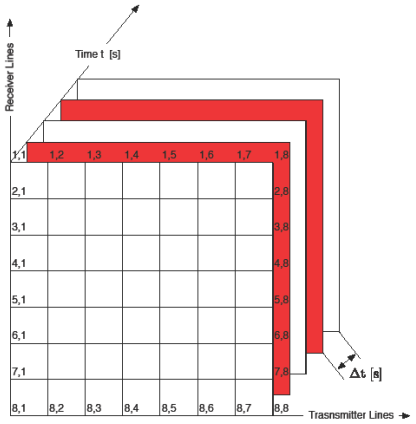

Figure 4.14: Data storage of the WMS signals. At every time step the void fraction is deposited in a matrix arranged by the corresponding radial coordinates.

analogue/digital conversion the signals are recorded by a data acquisition computer. The data is finally stored in a matrix whose dimensions are defined by the number of transmitter (number of matrix rows) and receiver wires (number of matrix columns) for every time step as depicted in Figure 4.14. Neglecting the resistance of the wires the amount of current flowing and thus the voltage at the receiver wires depends linearly on the conductivity of the phase within the measuring volume. In case of a gas liquid flow, Prasser et al. [122] showed, that the WMS produced a positive systematic error of up to 8% (absolute) for the measured gas fraction. The reason for the deviation was assumed to be an elastic deformation of the thin electrode wires. Nevertheless, the accuracy was found to be acceptable.

4.5.2 Sensor design

The major challenge of the sensor build at our laboratory were the very small dimensions of the 7 mm circular measurement cross section. Com-

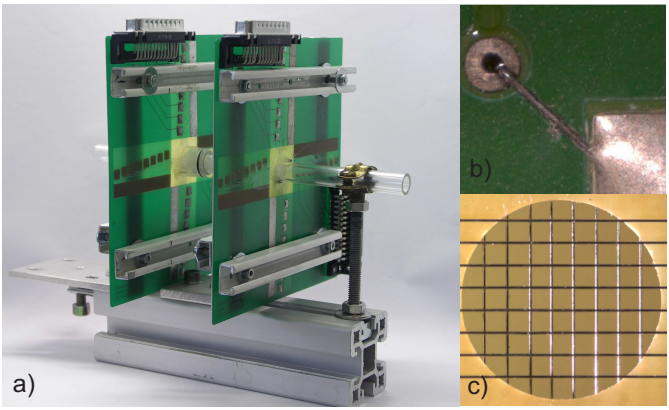

Figure 4.15: Experimental setup for multiphase flow characterization. The two WMS with the test section in between and the translucent polymer is depicted (a). A sample of a through-plated hole to avoid tearing the plate (b) and a front view of the two wire planes (c).

mercial sensors are always in the range of several centimeters. We therefore developed a new circuit board design which allows an easy soldering of 50 μm thick wires with a distance of 0.78 mm in between each other. The board is printed double sided whereas one side is the transmitter plane and the other is the receiver plane. Hence the board thickness of 0.6 mm is concurrent the axial displacement in between transmitter and receiver plane. The soldering pads were placed in a manner that all wires have the same length and that they can be designed very big to make sure that the force acting on the wires can be absorbed by the soldering joint. The reduction to 8 wires per plane was a consequence of the conclusion of Hampel et al. [63] who observed a huge influence on the flow by its highly spatially resolved sensor. Even the new board layout would allow a much higher resolution of the wire grid the number of 64 measurement nodes is assumed to be enough to estimate the void fraction. The wires were pulled through the holes in the circuit board and soldered on the backside of the board on the soldering pads. Therefore an initial load of 10 N was applied to tension the wire before

soldering. The holes in the pad were enforced by throughplating (Figure 4.15 b) to avoid tearing the plate down by the wire. At the end of the electric installation the connectors for the data cables were soldered on the provided slots. The measuring board was then stabilized by a frame consisting of rails fixed at the boarders of the plate. Afterwards the tube connections were mounted. A bush with O-ring was used on top of each plate. The bush was centered by means of two metal rods. For that purpose holes in the reactor socket were designed. The bush was simply glued by a two-component adhesive. By the stabilizing frame the plates were assembled on top of a horizontal slide rail allowing an axial movement of the WMS to ensure the simple exchange of the test section, which is placed in between the two sensor plates.

4.5.3 Measurement procedure

Since the WMS signals are amplified, a calibration is necessary. Each investigated phase has to be measured separately. The values of the current recorded for the lower conductive phase are referred to as the low calibration values $i_{low}(x, y, t)$ and correspond in case of a gas liquid flow to a void fraction $\varepsilon = 1$. The set with the values of the higher conductive phase are referred to as high calibration values $i_{high}(x, y, t)$ and correspond to a void fraction $\varepsilon = 0$. Assuming a linear correlation between current values i and void fraction ε the following relationships are valid.

$$\varepsilon(x, y, t) = 1 - \widetilde{i}(x, y, t) \tag{4.10}$$

$$\widetilde{i}(x, y, t) = \frac{i(x, y, t) - \overline{i}_{low}(x, y)}{\overline{i}_{high}(x, y) - \overline{i}_{low}(x, y)} \tag{4.11}$$

where $\widetilde{i}(x, y, t)$ is the fraction of the conductive phase. The time averaged values $\overline{i}_{high}(x, y)$ and $\overline{i}_{low}(x, y)$ were collected before every experimental run to take into account the drift of the electronics during operation due to warm-up effects. This is a troublesome procedure as the tubing including the sensors has to be dried and then flooded again. In a later version of the electronics resistors depicting a reference mesh sensor can be interconnected which enables a single calibration. The drift is compensated by a short reference measurement over the resistors at the be-

ginning of every experiment. For the preliminary experiments performed in this study the data was collected with a measurement frequency of $f_{meas} = 10\,\text{kHz}$ which lead to a three-dimensional arrangement of data points with a time scale and two spatial coordinates depicting a series of snapshots.

4.5.4 Experimental setup

The basic experimental setup (4.1) was used to generate the two phase flow. Therefore one vessel was pressurized with air and the other one was filled with water and also pressurized. Two flow controllers were used to control the flow of both phases separately. The virtual setup consist of two WMS placed at the inlet and the outlet of the test section, a camera at the outlet and a light source for the background illumination of the tube. The snapshots of the CCD camera with a pixel resolution of $1376 \times 1040 pixel^2$ reflect the flow pattern at the outlet of the test section allowing an estimate of the mean bubble size.

Chapter 5

Analytical methods

In order to characterize the laser sintered and stereo lithographic geometry different analytical methods were applied described in the following. Microscopy and x-ray tomography were used to specify the basic geometry of the manufactured parts and the scanning electron Microscopy (SEM) and the Brunauer, Emmet and Teller (BET) method were applied to estimate the surface topology.

5.1 Microscopy

For the purpose of magnification of the sintered structure and the plastic model for the characterization of the surfaces a stereo microscope of Zeiss® was used. The device is a Stemi 2000C equipped with camera (AxioCamMRc5). For illumination a cold-light source of type KL2500 LCD was applied.

5.2 SEM

To characterize the surface of the laser sintered material SEM was carried out. In this type of electron microscopy the sample surface is scanned with a high energetic beam of electrons in a raster scan pattern. In our case the secondary electrons are detected and give us information of

the sample surface topography. The device employed was a LEO 1530 Gemini (Zeiss, Germany). The working distance varied from 5 to 6.1 mm and an acceleration voltage of 5 to 10 kV was applied to the electron gun. Images with a pixel resolution of $1024 \times 768 pixel^2$ were acquired by collecting the emitted secondary electrons by an in-lens detector.

5.3 X-ray computed tomography

The computed tomography (CT) is an imaging method widely used in bio-medicine (Muller et al. [102], Viot and Bernard [153]), in material science (Agliozzo and Cloetens [2], Elmoutaouakkil et al. [44], Petrasch et al. [114]) and in various other engineering applications (Haussener et al. [67], Olurin et al. [105], Stampanoni et al. [140]). It allows the three-dimensional digital representation of the inside of an object. Therefore a stack of two-dimensional images is taken around a single axis of rotation and recombined to the three-dimensional geometry by applying digital image processing. In this study a system of Viscom (RH 104) was used with a Hamamatsu detector (Flatpanel 7942 CA-02) with a cross sectional resolution of $1032 \times 1000 pixel^2$ for transmission microtomography. This technique was first reported by Flannery et al. [48] who obtained tomographic reconstructions with a digital resolution of 1 μm using parallel, monochromatic synchrotron radiation. The limitation of today's conventional x-ray tubes is given by the size of the focal spot (Parish and Casson [107], Sasov and Van Dyck [131], Trefler and Gray [152]). But nowadays even sub-micron tomography is possible. The idea using microtomography to characterize the streamwise periodic structure investigated within this study originates from a work performed at ETH Zurich. Petrasch et al. [115] scanned ceramic foams to use the geometry for simulation purpose and characterization. CT has recently used increasingly to obtain geometric data as input for numerical simulations (e.g. Flin et al. [49], Maire and Buffiere [98], Petrasch et al. [115], Spanne et al. [139]). For our purpose different scans of the laser sintered structure made of stainless steel and a stereolithographic model were performed. The parameters for the scans are listed below.

A stack of images of a tomographic scan of a solid structure has usually a bimodal gray value histogram with two distinct peaks (Petrasch [113]).

Table 5.1: CT parameters for the scan of the designed structure made of different materials.

Parameter	**Stainless steel**	**WaterShed®**
Acceleration voltage [keV]	140-150	40
Nominal cathode current [μA]	60-64	225
Distance source-detector [mm]	220	220
Focal spot size [μm]	7, 10	7
Number of projections	901	901
Exposure time [s]	1	1
voxel edge length [μm]	5-6.5	5

One of those represents the void phase and the other one represents the solid phase. These maxima are called modes, the minimum between the maxima is called anti-mode. In the mode method of Weszka [161] the gray value corresponding to the anti-mode is chosen as the threshold value 0. The mode method is used within the current work for the three-dimensional reconstruction of the porous media investigated.

5.4 BET

For the determination of the mass specific surface of a material the procedure after Brunauer, Emmet and Teller (BET) can be applied. Therefore the adsorption of a gas is recorded at different relative pressures to get the BET isotherm. In most of the cases nitrogen is used. First the adsorption isotherm of the sample is estimated at the boiling temperature of nitrogen ($T_s = -196°C$). By the following equation the specific amount of nitrogen is estimated which is needed to cover the surface of the solid sample material with a monomolecular layer.

$$\frac{\left(\frac{p}{p_0}\right)}{n_{ads}\left(1-\frac{p}{p_0}\right)} = \frac{1}{n_m C} + \frac{C-1}{n_m C}\frac{p}{p_0} \tag{5.1}$$

where p is the equilibrium pressure of the adsorbent, p_0 the saturation vapor pressure of the adsorbent, n_{ads} the adsorbed specific amount, n_m the amount of material in the monolayer and C the BET constant $e^{\frac{H_1-H_i}{RT}}$ with H_1 the enthalpy of adsorption within the monolayer and H_i the enthalpy of adsorption within the layer i. The specific surface of the sample is then given by

$$S_{BET} = n_m \cdot S \cdot N_L \tag{5.2}$$

where S is the space needed of a single molecule of the adsorbent and N_L the Avogadro constant. It has to be mentioned that the resulting data of the method are strongly dependent on the applied procedure and not the real surface of the sample will be measured. e.g. Krypton as adsorbent delivers much smaller values compared to nitrogen or contaminations on the sample can lead to much higher values than expected. But the method is the most common used to determine specific surfaces because it is highly reproducible. However BET measurement may only be compared among each another.

Chapter 6

Experimental results

The experiments performed within this thesis are aimed at the demonstration of the feasibility to apply sintered reactors by design for the continuous handling of fast and exothermic reactions. For this reason the reactor is characterized in terms of mass and heat transfer by means of a single phase water flow at Reynolds numbers based on the empty tube diameter ranging from 600 to 7600 corresponding to volumetric flow rates up to 2.5 l/min. Water was chosen based on the simple handling of the fluid and the reproducible properties at its demineralized state in the laboratory. The chapter is subdivided in four parts. First the different porous structures are characterized by means of the analytical methods described in chapter 5. Then the results concerning radial and axial mass transfer are presented in the sections 6.2 and 6.3 followed by the characterization of the convective heat transport in the different porous media.

6.1 Characterization of porous media

6.1.1 Commercial metal foam

In the huge class of solid foams one differentiates in between closed and open cell metal foam. Only the open cell type is continuous and can be applied as static mixing element. It consists of interconnected solid

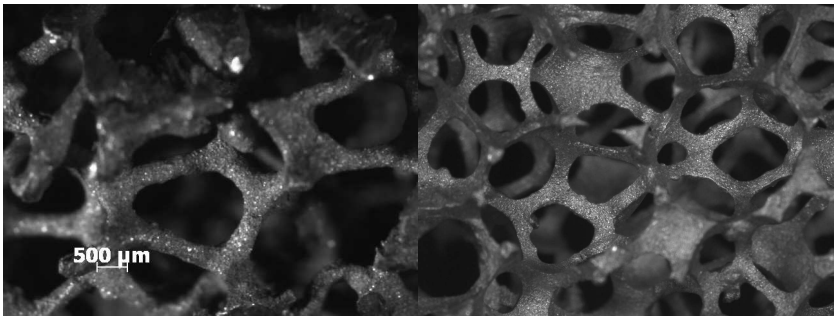

Figure 6.1: Microscopic images of a commercially available copper foam (20ppi) in comparison to aluminum foam (20ppi).

struts. The shape of a unit cell is the so called tetrakaidecahedron, a 14-faceted polyhedron, which represents the most energetically favorable shape of a single bubble in a network. Basically solid foams can be characterized by the pore size, which is the size of the windows in the cells as depicted in Fig 2.1, the porosity, the cross sectional shape of the ligaments and the material. In Figure 6.1 metal foam made of Aluminum (right) and Copper (left) is depicted. Both versions were used within this study. In the microscopic images one can clearly see the difference in the shape of the ligaments. Whereas the struts of the Copper foam exhibit a circular cross section the ligaments of the Aluminum foam show a triangular geometry. The cross sectional shape is associated with the relative density of the solid foam. The shape is continuously changing from triangular ($\rho^* \approx 3\%$) to circular ($\rho^* \approx 15\%$). The equivalent pore size is given as the number of pores per inch (ppi). For the foam used in this study Hackeschmidt [61] proposed the following equation to calculate the hydraulic ligament diameter d_l and the real pore size d_p.

$$d_l = \frac{1}{\sqrt{3}} \frac{0.0254m}{\gamma} \sqrt{(1-\varepsilon)\frac{2.244}{\pi}} \tag{6.1}$$

$$d_p = \frac{\varepsilon d_l}{1-\varepsilon} \tag{6.2}$$

where γ is the number of pores per inch and ε is the porosity, which was identified by a gravimetrical measurement for the commercial Copper foam of the pore sizes 20 and 30 ppi. Values of 83% and 86% were found with very small standard deviations which is in agreement with the circular ligament shape.

6.1.2 Designed porous media

For the basic geometry, depicted in Figure 2.3, the objective was to reproduce the structure of commercial foam as accurate as possible to compare the simulation with available experimental results. In our case the manufacturing of the model came to the fore, as we started with the digital model. We had to ensure the stability of the structure and coincidental take over the major advantages of metal foams like the specific surface area. The finally developed geometry is the negative pattern of tetrahedral overlapping spheres. The spheres with a diameter of 2.9 mm and a distance of 2.75 mm were subtracted from a cylinder with a diameter of 7 mm to describe a tubular reactor. Whole the domain consists of 3 layers of cells in axial direction, which depicts the periodic unit length of 6.74 mm as shown in Figure 6.3. The 12 windows of a single cell, the so called pores, have a diameter of 0.92 mm and connect the centered cell with the 12 neighboring. The shape of the resulting ligaments is triangular which is favorable in terms of heat and mass transfer as shown by Hackeschmidt [61]. The foam was build by two different manufacturing methods explained in section 2.2.2. The stainless steel model was provided for the characterization of the heat transfer and the axial dispersion and as catalyst support for a chemical synthesis. For flow investigations and optical radial scalar transport measurements a transparent plastic foam was generated. The different manufacturing types offer different tolerances leading to deviations in comparison to the digital model. Therefore a geometric characterization was performed.

Microscopy

By the verification of the fully sintered reactor (stainless steel) a very good agreement of the manufactured device to the model was found. The basic shape could be reproduced with a high accuracy. Figure 6.2

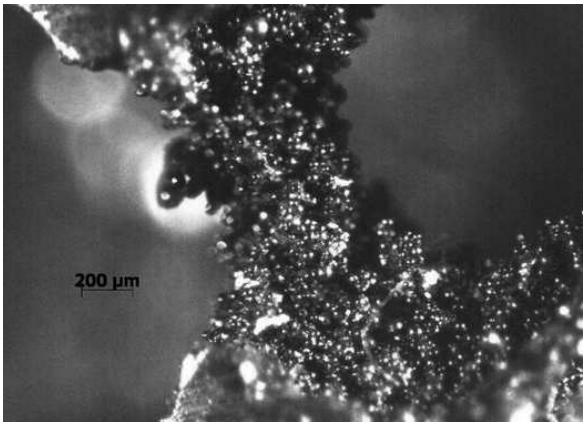

Figure 6.2: Microscopic images of a stainless steel ligament sintered by SLS. The small spheres correspond to the feedstock particles (diameter of 20 μm).

depicts a single ligament. A high roughness of the surfaces was found as a result of the manufacturing process. The roughness was assumed to be in the order of the feedstock particles (diameter of 20 μm) by examining the microscopic images. Although this surface offers a good opportunity as catalyst support it was adjudged to be insufficient for an experimental comparison with numerical results. Therefore we decided to use two different materials as already explained above. The sample made by SL is presented exemplary in Figure 6.3. It was found that the geometry is much smoother but it reveals a wavy surface. This effect can be ascribed to the hardening process, where layer by layer of a liquid resin is hardened to build the three-dimensional geometry. The heat impact of the laser leads to a slight flow of the top layer. Due to this effect a further geometry mismatch occurs. The edges of the ligament are rounded compared to the CAD model. This has to be taken into account for the numerical investigations. A statistical analysis of the microscopic images lead to a mean edge diameter of 0.065 mm. Given that with the microscopy only the bottom and the top layer could be taken into account another method had to be applied.

X-ray tomography

X-ray tomography allows the three-dimensional digital representation of the inside of an object. Figure 6.3 depicts a microscopic top view of the geometry in comparison to a slice image of the tomogram and the original geometry. It can be clearly seen that the information of the x-ray scan is of a much better quality as the edges can be higher resolved and this also within the structure. There is a clear difference of the designed geometry to the manufactured plastic sample which has an axial extend of 53.89 mm, corresponding to 8 periodic elements in series. The sharp edges are clearly rounded and the ligaments exhibit an enhanced hydraulic diameter. These obviously small changes in the geometry have a strong influence on the flow field and the turbulence induced. Therefore the CAD model was adapted corresponding to the x-ray tomogram in order to quantify the influence of the diversity of the geometry and to compare the simulation with the experimental results. The best agreement of the manufactured structure and the CAD model was achieved by decreasing the diameter of the cells to 2.78 mm and by rounding the resulting edges with a diameter of 0.12 mm. All other geometric parameters described above remained the same. The resulting periodic computational domain is depicted in Figure 6.3. The porosity of the structure changes from 0.84 to 0.78 compared to the original geometry and the resulting pore size is 1.01 mm. A three-dimensional reconstruction of an array of multiple cells is depicted in Figure 9.10. This test case was generated to demonstrate the ability to perform simulations within the scanned structure for a running project.

SEM

In order to have a closer look on the surface of the untreated sintered material a flat sample was manufactured with the SLS technique. A small probe of this was then characterized by means of SEM. In Figure 6.4 two SEM images with a fivehundredfold and a twothousandfold magnification are presented. The circular shaped particles of the feedstock can be seen on the top of the sample. This is due to the fact that some particles sinter with the hot surface of the top layer during manufacturing. The specification of a mean particle diameter of 20 μm given by

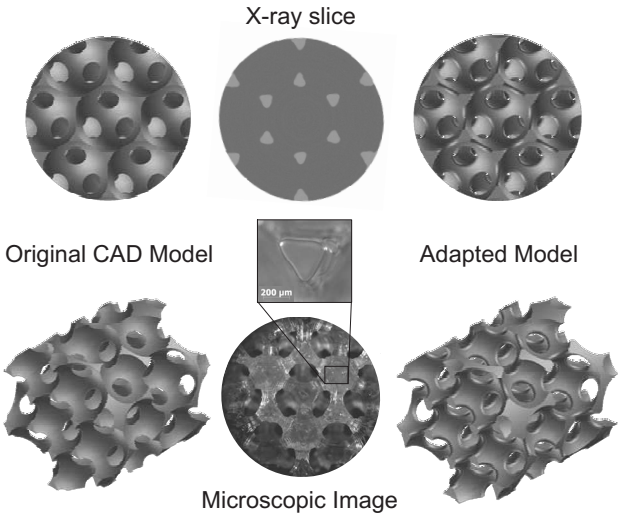

Figure 6.3: In the left column the original CAD model is depicted which was adapted by the aid of an x-ray scan to the manufactured model which is shown in the middle column. The geometry on the right is the one finally used for the LES with the best match to the plastic model.

the supplier of the material is in a good agreement with our observations. For other applications the rough surface is pretreated by different methods, like sand blasting, to achieve a smooth surface. In our case of the porous media this is not possible and also not requested. The rough surface offers better properties as catalyst support as the coating area is strongly increased.

BET

To get an idea about the specific surface of the different foam samples used in the experiments a BET analysis was performed. The dimensions of the sample were limited by the experimental setup to foam elements of a diameter of 7 mm and a length of 100 mm. This corresponds to a sample mass up to 10 g. Two commercial copper foams of 20 and

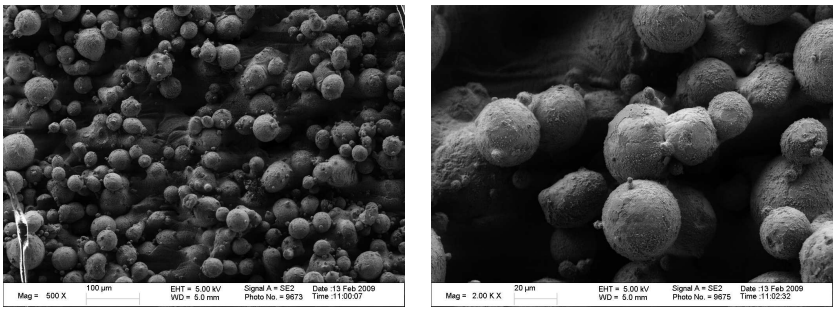

Figure 6.4: SEM images of a flat laser sintered stainless steel sample with a magnification of 500 (left) and 2000 (right).

30ppi and the sintered structure were investigated. For the cooper foam the specific surface area was too small to detect. A compression of the foam would be possible as more foam could be placed in the sample holder. But this procedure would falsify the results completely and we therefore decided to only measure the surface of the sintered sample. The sample used was without wall which means that the specific surface area is slightly decreased in comparison to the fully sintered reactor. A total area of $0.101\,\mathrm{m}^2$ was found which corresponds to a specific surface of $26'244\,\mathrm{m}^2/\mathrm{m}^3$. By comparing this area to the theoretically calculated surface according to Kozeny [81], who assumes the pores as uniform, parallel cylinders with constant diameters d_p, a very good agreement is found.

$$A_S = \frac{4\varepsilon}{d_p(1-\varepsilon)} \tag{6.3}$$

With the porosity ε and the pore diameter d_p from the CAD model a value of $22'800\,\mathrm{m}^2/\mathrm{m}^3$ can be determined. As the sintered parts exhibit a very rough surface a higher value for the specific surface of the experiment compared to the theoretical consideration could be expected. Nevertheless as mentioned in the description of the method, BET results can only be compared among each other. Richardson et al. [128] found for ceramic foams of similar pore sizes (20-45ppi) surfaces which are again two orders of magnitude higher then the one we measured for

the sintered reactor. He ascribes this to pores in the material. In fact he did not take into account that ceramic foams are hollow due to the manufacturing process. This inner structure is indeed accessible but there is no flow through these pores during operation. For those reasons reference performance measurements of other catalyst supports are needed in the coated state during operation as this is of importance for the final reaction. A nice comparison of the specific surface of solid foams with monoliths, different structured packing and trickle beds is presented in Stemmet [141]. At the absolute highest porosities (more than 90%) they reach specific surfaces in the order of monoliths and higher which make them favorable as catalyst supports.

6.2 Radial transport of a passive scalar

To characterize the hydrodynamic performance of porous metal foam structures simultaneous PIV and PLIF measurements were performed in two different planes orthogonal to the axial and radial coordinates as shown in Figure 4.7. The Reynolds number based on the empty tube diameter and the bulk velocity was ranging between 600 and 7600. First the influence of metal foams on the mean velocity field will be described qualitatively by the PIV measurements in the plane orthogonal to the z axes. We further discuss the flow behavior behind metal foams in detail by comparing the velocity profiles in Figure 6.7 and 6.8 extracted from the plane orthogonal to the x coordinates at the positions $0.4D$ and $2D$ downstream of the foam outlet. The turbulent kinetic energy, depicted in Figure 6.9, is averaged over the first domain (see Figure 4.7) which has an extent of $0.5D$. This graph describes the turbulence induced by the metal foams of different pore sizes and the streamwise periodic structure. The decrease of the turbulent kinetic energy k with increasing distance from the foam elements is clarified in Figure 6.10. Therefore four equally sized regions (domains 1-4) were defined to obtain spatially averaged data of k. The excellent mixing properties of solid foams are demonstrated in Figure 6.12 by the contour plots of the mean concentration field and quantified in Figure 6.13 by the coefficient of variation. At the end the overall performance of the different metal foams is assessed by the pressure drop and the product of the friction factor with the coefficient

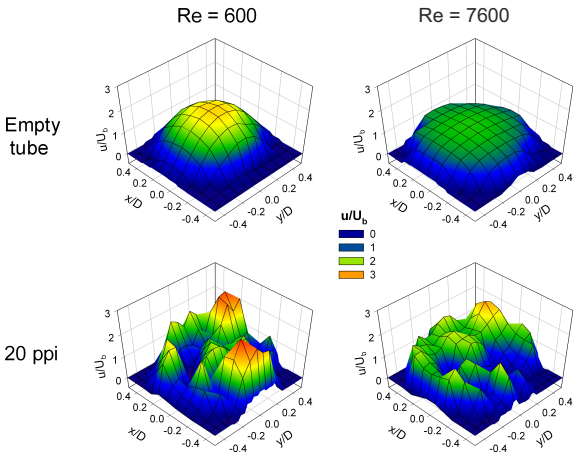

Figure 6.5: Streamwise velocity component $0.25D$ downstream the outlet of the test section for the empty tube and the 20 ppi foam case at the Reynolds number 600 and 7600.

of variation in Figure 6.14 and 6.15.

6.2.1 Velocity profiles and turbulent kinetic energy

PIV measurements in the plane orthogonal to the flow direction were performed to further characterize the radial components of the velocity field but it was impossible to fully resolve both components of interest. The radial component in x direction (see Figure 4.7) was overlapped by the velocity in axial direction due to the tracer particle motion out of the plane of measurement as explained in section 4.2.1. This leads to a very strong interference of the measurement by the axial velocity component which is an order of magnitude higher than the radial one. Although those measurements have only a qualitative character they are very helpful for the understanding of the influence of metal foam on the mean flow field. Also comparisons of the normalized quantities within the

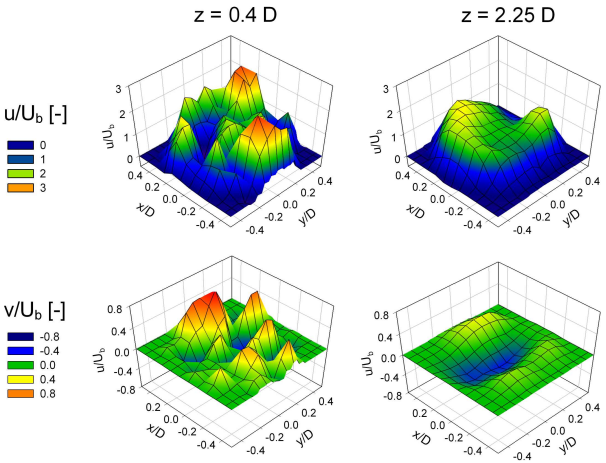

Figure 6.6: Streamwise and radial velocity component $0.4D$ and $2.25D$ downstream the outlet of the test section for the 20 ppi foam case at the Reynolds number 600.

measurement series are valid. Figure 6.5 depicts the streamwise velocity field measured at a distance of $0.25D$ downstream the outlet of the test section for an empty tube case and a case with inserted metal foam elements with a pore size of 20 ppi. A laminar and a turbulent profile based on the empty tube diameter are shown. For the laminar empty tube case the typical Hagen-Poiseuille flow field can be observed where in the turbulent case the profile is clearly flattened. Both velocity fields are well developed which indicates a sufficient length of the test section to stabilize the flow. In addition one can observe a high accuracy and reproducibility of the measurement method even near the wall. In case of inserted metal foam of 20 ppi the mean axial velocity component is clearly diversified compared to the empty tube. Jets of high velocity are observed indicating pores in the outlet cross section of the foam which lead to a random characteristic of the velocity field. A quantitative statement on the effect of the Reynolds number based on the data of the xy-plane is not suitable because of the influence of the timing. Especially

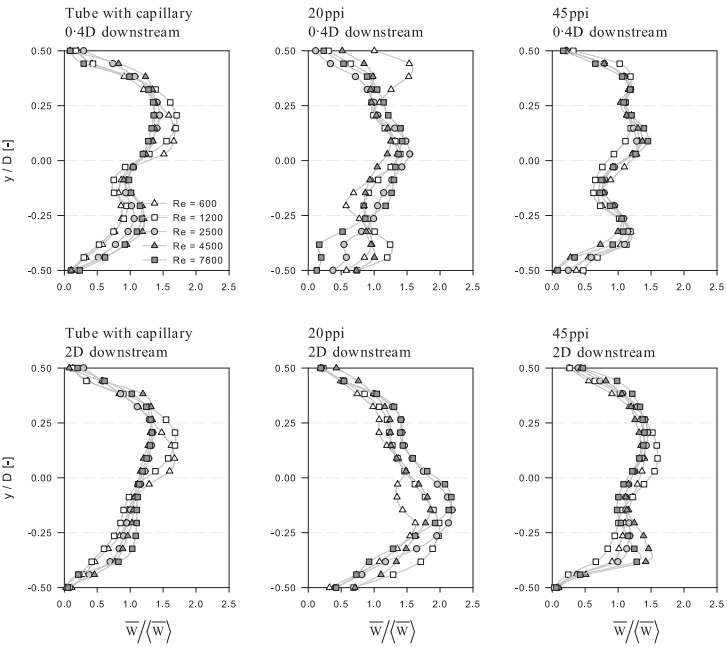

Figure 6.7: Mean axial velocity profiles measured at $0.4D$ (upper row) and $2D$ (lower row) downstream of the inserted foam element, respectively the end of the capillary, for the case of an empty tube (left column), a 20 (middle column) and a 45ppi foam element (right column).

when high velocity gradients occur a huge amount of tracer particles can leave the light sheet during the recording of the double frame for cross correlation. In Figure 6.6 the velocity components u and v are presented, measured at two different positions $0.4D$ and $2.25D$ downstream the 20 ppi metal foam element. The radial component in y direction, which is not falsified by the streamwise velocity, is randomly distributed over the whole cross section. This indicates the plug flow behavior caused by metal foam inserts. By comparing the velocity profiles at the two different positions a fast development back to an empty tube case can be seen. This results in a decrease of the radial velocity component and

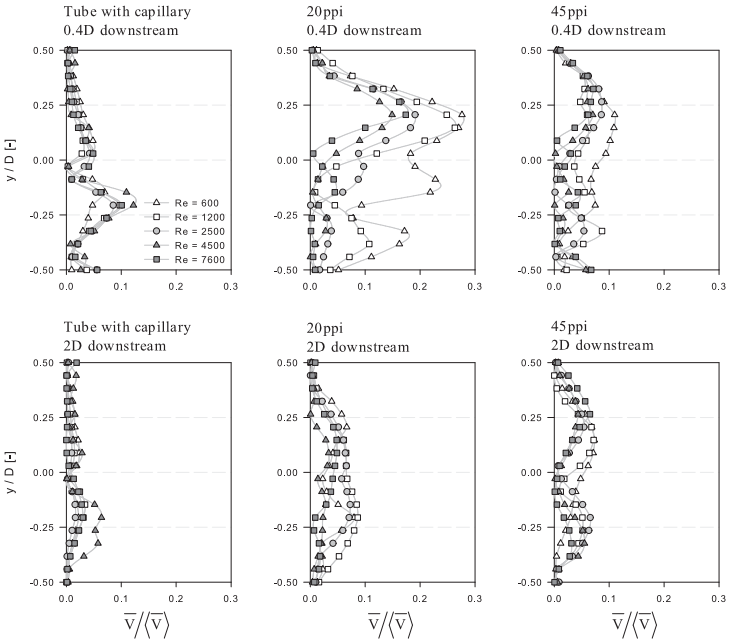

Figure 6.8: Absolute mean radial velocity profiles measured $0.4D$ (upper row) and $2D$ (lower row) downstream of the inserted foam element, respectively the end of the capillary, for the case of an empty tube (left column), a 20 (middle column) and a 45ppi foam element (right column).

also a fast decrease of turbulent kinetic energy with increasing distance to the foam as shown below (Figure 6.10).

Figure 6.7 depicts the mean axial velocity component for a tube with inserted capillary without foam and the tube with inserted foam of 20 and 45 ppi $0.4D$ and $2D$ downstream of the metal foam. The empty tube with inserted capillary is presented in the upper left corner of Figure 6.7. The asymmetry of the wake in the velocity profile indicates that the capillary is not centered perfectly in the tube. The typical shape for a flow field in an annular channel is still observed. The maximum velocity is found at a radial position of $0.25D$. The turbulent and laminar

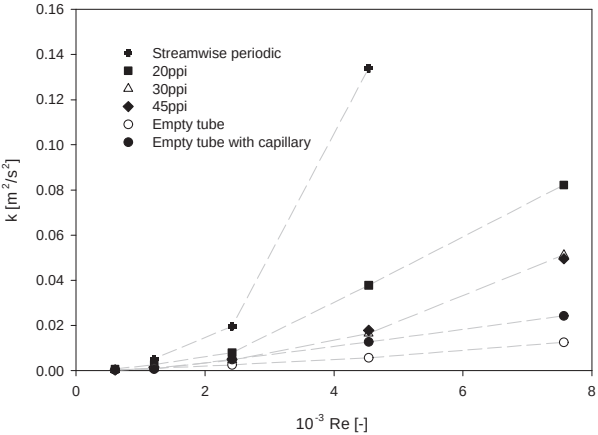

Figure 6.9: Turbulent kinetic energy subject to the Reynolds number. The quantity was averaged in an area up to $0.25D$ (domain 1) downstream of the foam, respectively the end of the capillary.

(based on the empty tube diameter) velocity profiles differ in their shape. The turbulent profiles are flattened and exhibit steeper gradients near the wall. The mean velocity profiles behind the metal foams (20 and 45 ppi) exhibit completely different characteristics. Random velocity profiles can be observed over the whole range of investigated Reynolds numbers. In addition no difference between turbulent and laminar profiles is found. The interplay between jets and wakes depends mainly on the cross section at the outlet of the foam and reveals where open pores (jets) and where ligaments are present (wakes). The observed velocity peaks are randomly distributed in radial direction and lead to the assumption that the velocity profile is similar to turbulent plug flow in an empty tube over the whole range of Reynolds numbers. By comparing the axial velocity profiles at the two different positions $0.4D$ and $2D$ one can observe a development of the velocity profiles towards the empty tube case. This leads concurrently to a fast decrease of the mean radial velocity component as depicted in Figure 6.8. The largest values of

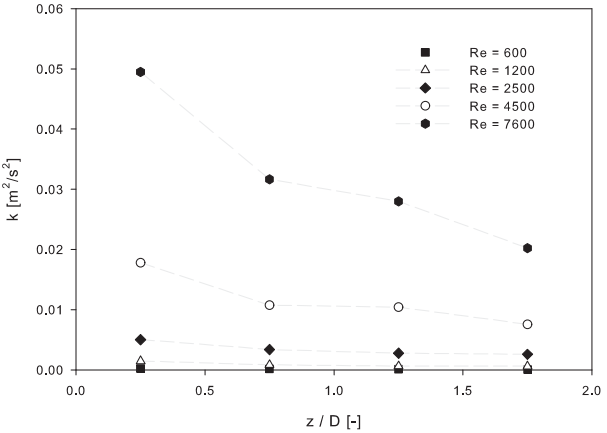

Figure 6.10: Axial development of the turbulent kinetic energy downstream of a 45 ppi foam element.

the normalized absolute mean radial velocity were measured behind the metal foam with the largest pore size of 20 ppi. This leads to a strongly enhanced radial scalar transport shown in the next section.

Figure 6.9 shows the overall mean turbulent kinetic energy versus the Reynolds number at the outlet of the different porous media and the empty tube. The kinetic energy is increased behind the metal foam elements, compared to the empty tube. The increase of the turbulent kinetic energy is monotone with the Reynolds number. No transition region from laminar to turbulent flow can be seen according to these data. We therefore expect an intermittent flow within the pores of the investigated porous structures independent of the Reynolds number. In addition the turbulent kinetic energy is changing with the pore size for the commercially available metal foam. The highest velocity fluctuations were observed behind the 20 ppi foam which leads to a very good mixing efficiency by convective scalar transport. The differences between the 30 and the 45 ppi foam are very small but still a very high turbulent kinetic energy is induced. Our investigations are in accordance with the

measurements of Ferrouillat et al. [47]. In this paper a decreasing micro mixing time with increasing pore size was observed. This is explained by an increased turbulence induced by the thicker ligaments which supports the formation of vortices. The assumption is based on the investigations of Lu et al. [94] where the metal foam is regarded as an arrangement of vertical and horizontal tubes. Comparing the spatially averaged turbulent kinetic energy of the designed periodic domain and the commercial metal foams, enhanced values for the rapid prototyped structure are observed. Although the pore size of the designed structure is smaller compared to the commercially available metal foams. This contrary behavior of the designed structure can be explained by the difference in the geometry. The ligaments of the streamwise periodic domain are thicker than the ones of the commercially available metal foams and additionally their pore size is decreased.

The axial development of the turbulent kinetic energy of the flow behind a 45 ppi metal foam is presented in Figure 6.10. The radial and axial velocity fluctuations are decreasing with increasing distance to the foam and therefore the turbulent kinetic energy is decreasing. The reduction of kinetic energy results in a strongly reduced downstream mixing efficiency.

6.2.2 Mixing efficiency

To characterize the mixing efficiency of the different metal foams, a tracer dye (water-Rhodamine B solution) was injected into the main stream. Planar laser induced fluorescence was performed in a plane normal to the axial direction $0.4D$ downstream of two foam elements as depicted in Figure 4.7. The total length of the mixing elements of 50 mm was kept constant during all experiments. 600 single frame images were recorded showing the concentration distribution of a tracer dye. The distortion for the cross section of the tube is more complex and a perspective mapping method was applied as explained in section 4.2.1. A resulting snapshot of the concentration field is presented in Figure 6.11. Although the snapshot depicted in Figure 6.11 is representing a very homogeneous concentration distribution the small differences in concentration can be fully resolved by the CCD chip of the digital camera applied. This could be shown by measuring a completely homogeneous reference concentra-

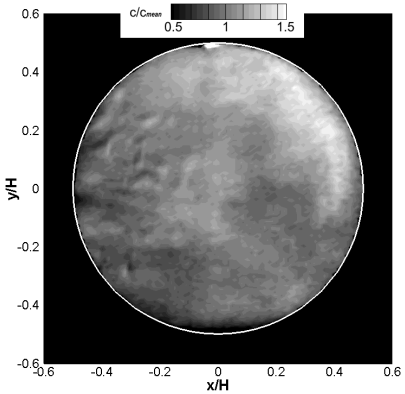

Figure 6.11: Snapshot of the concentration field during the experiment with a 45ppi foam at Re=7600

tion field like described in section 4.2.2. The circular shape illuminated by the laser light sheet was observed clearly after the perspective mapping indicating that the applied method is valid. One only has to pay attention to gas bubbles while degassing the system at the beginning of an experiment and deposited seeding particles which would affect the measurements.

To discuss the influence of the porous media on the radial distribution of the scalar, contours of the mean concentration fields are presented in Figure 6.12 exemplary for the commercially available metal foam of different pore sizes. The concentration is normalized by the mean concentration $\langle \overline{c} \rangle$ of the pipe cross section. For the empty tube at a Reynolds number of $Re = 600$ no spatial dispersion of the scalar is observed. The cross-section of the two scalar plumes, which originate from the two injection points in the capillary, can be clearly distinguished. For increasing Reynolds numbers the dispersion of the scalar increases and the two plumes are no longer distinguishable. The increase in mixing is promoted by the increasing turbulence intensity towards higher Reynolds numbers. However, peak values of the concentration are still observed in the plane of measurement which indicates that the mixing process due to turbulence is not completed in the plane of measurements. The results

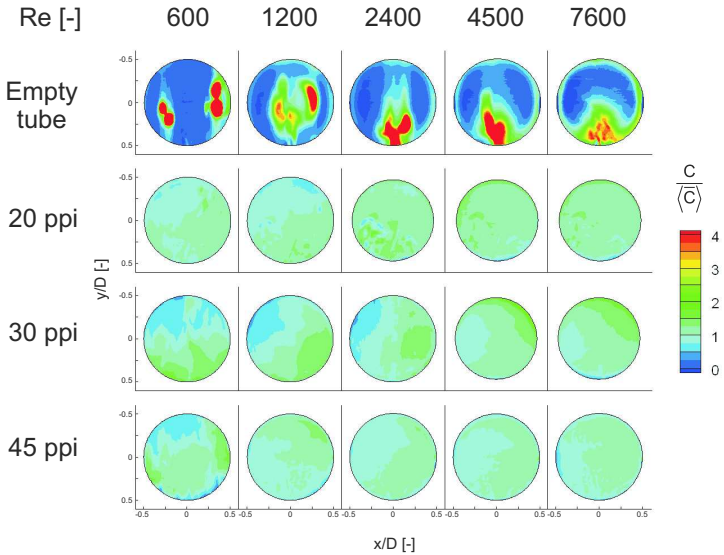

Figure 6.12: Contours of the mean concentration field in the cross section $0.4D$ downstream of the foam elements, respectively the capillary.

of the three different foams exhibit a much smoother mean concentration field in the tube cross-section. In contrast to the empty tube no peak values of the concentration are observed irrespective of the Reynolds number. This clearly demonstrates the mixing enhancement due to the presence of the metal foams. Although the injected side stream was kept constant at 6 ml/min a slightly enhanced degree of homogenization can be observed when increasing the Reynolds number. To quantify the mixing performance, the coefficient of variation (Edward [43], Hiby [69]) was used, which is defined in section 3.2.

Figure 6.13 represents the CoV with respect to the corresponding Reynolds number for the empty tube and the metal foams of 20, 30 and 45 ppi. To describe the general behavior of the mixing efficiency with respect to the Reynolds numbers a correlation of Fasano [46] used for Kenics static mixing elements was applied to our experimental re-

Table 6.1: Coefficients calculated from Eq.6.4 by fitting the experimental data set Fasano [46]. The different samples are commercially available foams of 20, 30 and 45 ppi and the selective laser sintered structure (SLS).

Sample	a	b
20 ppi	0.54	0.16
30 ppi	0.41	0.18
45 ppi	0.61	0.15
SLS	1	0.11

sults. Since the length of the mixer was kept constant at all experiments the correlation can be transformed to the following simple equation:

$$-log\left(\frac{CoV}{CoV_0}\right) = a \cdot Re^b \tag{6.4}$$

$$CoV_0 = \sqrt{\frac{Q}{q}} \tag{6.5}$$

a and b are constants corresponding to the different setups, CoV_0 is the initial mixture quality, q denotes the injected side stream and Q the main stream. The computed curves are fitted with the data points for empty tube Reynolds numbers above 1200 (fully turbulent regime) and are illustrated in Figure 6.13 as dotted lines. Table 6.1 shows the corresponding constants for the foams of 20, 30, and 45 ppi. For all cases the CoV is decreasing with increasing Reynolds number, due to enhanced turbulence. A remarkable change in the coefficient of variation is observed when using metal foams compared to the empty tube. Values up to 0.3 after a constant mixing length of 50 mm were measured. In addition an influence of the pore size is found. The best mixing performance for commercially available foam is achieved with the 45 ppi foam, as the CoV is below 0.1. The 20 ppi foam exhibits better mixing compared to the 30 ppi foam. This can be explained by the higher turbulence intensity induced by the structure with bigger ligament thickness, which leads to a better mass transfer in radial direction. The streamwise periodic

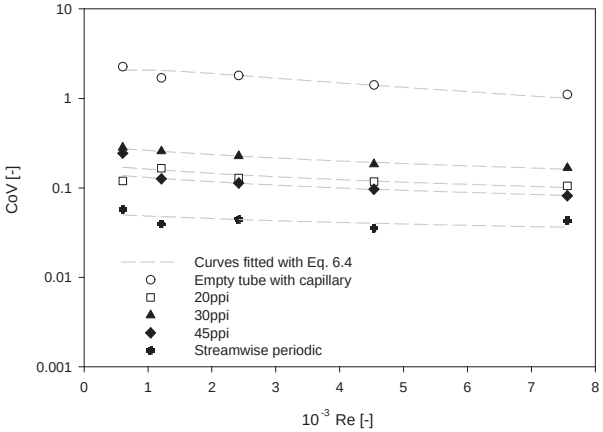

Figure 6.13: coefficient of variation (CoV) for the empty tube case and the cases of inserted 20, 30 and 45 ppi foams.

structure exhibits much smaller values of the CoV than the commercial metal foams. A slight decrease with the Reynolds number can still be observed due to the enhanced turbulence at higher velocities. But obviously this effect is comparatively small and the designed geometry is already very efficient at small velocities. With values below 0.05 for the CoV the tracer is nearly completely homogenized over all Reynolds numbers investigated. We assume on the basis of the present results that the mixing in metal foams on macro scale level is controlled by two different effects: First the flow lamination which occurs due to the separation of the flow at every ligament of the foam. This effect is intensified for commercial foams with smaller pore sizes since more ligaments per volume are present. The second effect is the turbulent mixing which takes places in the cells of the foam. This effect is dependent on the ligament thickness and the ligament shape. The thicker the ligaments are the more turbulence is induced and as a result a better mixing efficiency is observed. This therefore leads to the assumption that the interplay of those two mechanism results in an optimum pore size which is depen-

dent on the application of the metal foam. The decoupling of the pore size and the ligament thickness is achieved by the application of SLS. The meso scale reactors by design enable therefore a scaling independent from a basic cell geometry which is a big advantage compared to the commercially available solid foam.

The comparison of the CoV with literature results is difficult since there are no data available for this rather small tube diameter range. Compared to the measurements of Wadley and Dawson [155] who uses larger tube diameters we obtain the same degree of homogenization by using much shorter static mixing elements. The comparison with the combined numerical and experimental study of Hirschberg et al. [71] addressing SMX static mixers with larger diameter reveals lower values of the coefficient of variation for shorter mixing elements using metal foams. The designed structure however reaches the efficiency of commercially available static mixing elements.

6.2.3 Pressure drop

The measured pressure drop of the test section subject to the bulk velocity is depicted in Figure 6.14. Since the setup was slightly different for the designed porous media, described in section 4.2.3, only the pressure drop of the commercially available foam is compared for these experimental series. A detailed comparison of the different porous media will be presented in section 6.3.4. The pressure drop of the empty tube case, the tube with inserted capillary and with inserted metal foams of different pore sizes is shown. A small influence of the capillary on the pressure drop is observed. When inserting metal foams the pressure drop is strongly increased compared to the empty tube. This increase with the velocity follows the correlation suggested by Dupuit [39] which yields a quadratic relation for the pressure drop to the velocity. As the measurements of the pressure drop were performed over the whole test section the drag coefficient as well as the permeability of the foam could not be evaluated by simply fitting this correlation to the measurements and will therefore not be presented here.

The highest pressure drop of about 0.6 bar was observed for the 45 ppi foam. The pressure drop is increasing with decreasing pore size, also shown by Boomsma and Poulikakos [24], Dukhan [37], Hackeschmidt

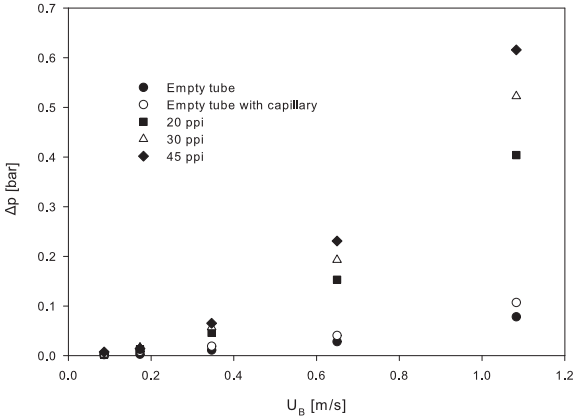

Figure 6.14: Pressure drop subject to the bulk velocity.

[61]. This opposing trend of the pressure drop and the turbulent kinetic energy is a crucial advantage for the technical application of metal foams and is a typical behavior for micro structured devices. Due to the small dimensions the flow is mostly laminar while the pressure drop is strongly increased.

To characterize the overall performance of a static mixing device the mixing performance described by the CoV and the pressure drop has to be taken into account. A dimensionless value which describes the pressure drop is the friction factor defined corresponding to Boomsma, Poulikakos and Zwick [26]:

$$f = \frac{\triangle p}{4 \cdot \frac{L}{D} \cdot \frac{\rho U_B^2}{2}} \tag{6.6}$$

L is the length of the mixing element of 50 mm, D the inner diameter of the tube, ρ the density of the fluid and U_B the bulk velocity. The product of the friction factor with the CoV is a measure to compare the overall performance of the investigated systems. This product versus the Reynolds number based on the tube diameter and the bulk velocity is

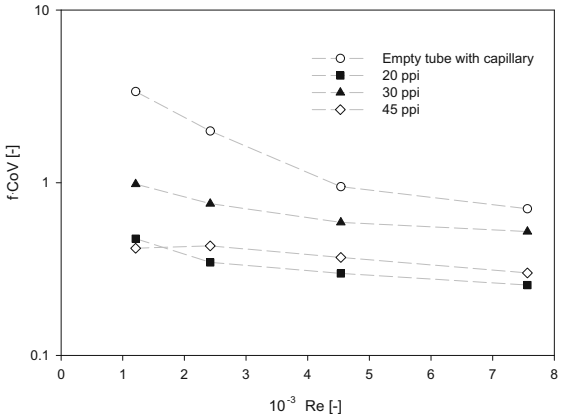

Figure 6.15: Product of the friction factor and the coefficient of variation as a measure of the overall performance of the metal foams subject to the Reynolds number.

depicted in Figure 6.15. Although the pressure drop in the empty tube with inserted capillary is much smaller the metal foams show strongly decreased values for the product $f \cdot CoV$ due to the very good mixing behavior of metal foam. The smallest value and therefore the best overall performance is found for the foam with the biggest pore size of 20 ppi in spite of the smaller mixing efficiency compared to the 45 ppi foam. Among the investigated commercially available foams the 20 ppi foam is the best tradeoff for a chemical reactor if one additionally assumes that the heat transfer is also increased with increasing pore size as shown in other applications e.g. Hackeschmidt [61].

6.2.4 Conclusions

In this experimental series we examine the mass transfer within metal foams and the designed streamwise periodic structure. As a first step we assessed the mixing performance in a single phase flow system. We performed experiments at Reynolds numbers between 600 and 7600 based

on the empty tube diameter and the bulk velocity. Commercially available foams of different pore sizes (20, 30 and 45 ppi) and the streamwise periodic structure were investigated and compared to the empty tube case. The mean flow field is clearly distorted by the metal foam. As a consequence the radial dispersion of a tracer dye, injected in front of the foam elements, is strongly increased. This leads to an enhanced mixing efficiency quantified by the coefficient of variation. The designed porous media achieved after a short mixing length of 50 mm values below 0.05, which is comparable to commercially available static mixing elements. The flow field measured downstream the porous media leads to the assumption of a distinct plug flow behavior within the structure which is favorable for the design of continuous chemical reactors. This point will be addressed in the next section by investigating the axial dispersion and the consequential residence time distribution within the different devices.

6.3 Axial dispersion

Experiments were performed at four different flow rates ranging from 0.2 l/min to 1.5 l/min, which corresponds to values of the Reynolds number up to 4500 based on the empty tube diameter. Metal foams made of copper with pore sizes 20 and 30 ppi were investigated and compared to the SLS structure. In the following sections the results will be analyzed. An overview of the tracer pulse experiments performed is given in Table 6.2. First the mean residence time distributions will be discussed exemplary for the case of the short tube assembly. Then the mean residence time will be presented to check the accuracy and reproducibility of the test section and to exclude dead volumes in the reactor. This section is followed by the discussion of the axial dispersion including a comparison of solid foams to packed beds and common packing materials. In the last part the pressure drop of the different investigated porous media is compared.

Table 6.2: Overview of different experiments performed with the corresponding parameters

This work	**Solvent**	**Solute**	**Sc**	**Packed bed**	**L (m)**	$\mathbf{d_p}$**(mm)**	$\mathbf{L/d_p}$	ε	$\mathbf{Re_p}$
20 ppi	Water	KCl	527	Metal foam	0.2, 1	1.498	134, 668	0.83	156-1170
30 ppi	Water	KCl	527	Metal foam	0.2, 2	1.14	176, 878	0.86	115-860
SLS	Water	KCl	527	SLS	0.2, 3	0.92	217, 1087	0.84	95-947

6.3.1 Residence time distributions

From the recorded tracer concentrations at the inlet and outlet of the different reactor setups the residence time distribution $E(t)$ is calculated by deconvolution. The resulting data for the short tube assembly are presented in Figure 6.16. The dots correspond to the post processed measurement data of one single measurement and the lines are fitted curves to the complete measurement series using the dispersion model. The model approach reproduces the measured data with a very high accuracy and only slight differences between the different setups are observed. For all cases the peaks are uniformly distributed over time, since the porosities and therefore the mean residence times are similar for all investigated porous media. A slight difference in the width of the peaks can be seen resulting in different vessel dispersion numbers. An increased dispersion coefficient and therefore broader peaks are observed for the sintered structure but even more for the 20ppi foam compared to the 30ppi foam at a given bulk velocity. The negative values which primarily appear in front of the residence time distribution of the highest investigated velocity, result from the applied deconvolution. The method becomes sensitive to noise if the inlet and outlet concentration distributions of the tracer pulse become more equal. The interstitial bulk velocity of about 0.8 m/s is the highest which still could be resolved properly. In general the measured residence time distributions are very narrow for all investigated foam structures. This strongly supports the assumption of a global plug flow behavior within these geometries.

6.3.2 Mean residence time

By fitting the axial dispersion model to the measured data the mean residence time τ is estimated. In all measurement series τ is accurately reproducible over all five independent experiments, demonstrated by the standard deviation depicted as error bars in Figure 6.17. A mean deviation of 0.08 s was calculated which corresponds to a mean relative deviation of less than 2%. The mean residence time is a very important variable for the characterization of a reactor. In case of unintentional dead volumes it is clearly decreased compared to the theoretical value. In Figure 6.17 the mean residence time per unit length measured in all

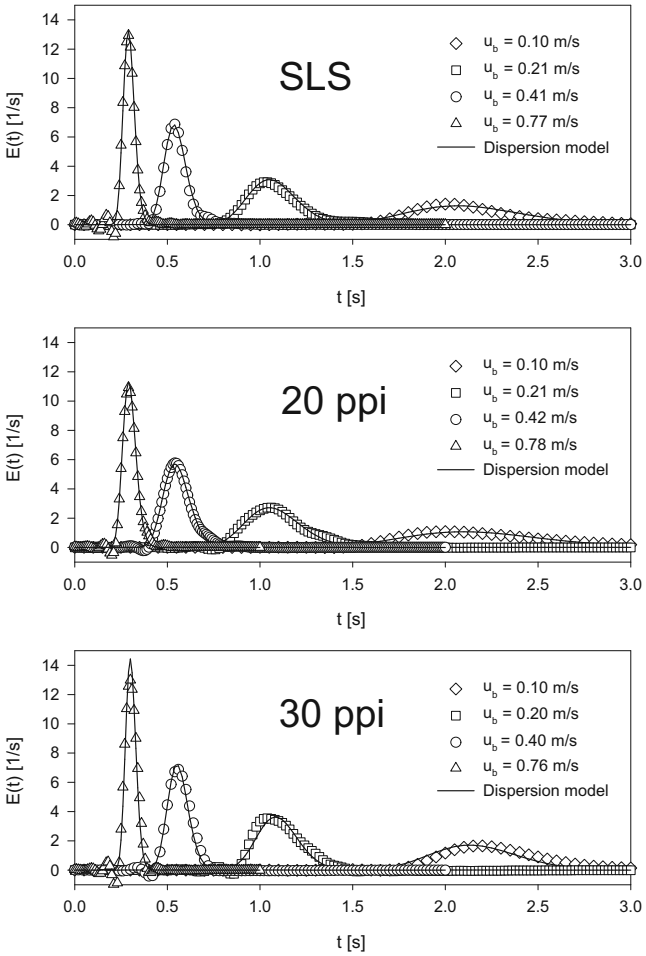

Figure 6.16: Estimated residence time distributions (dots) for the short tube experiments and the corresponding curves fitted with the axial dispersion model (continuous lines). From the top: The sintered structure, the 20 ppi metal foam and the 30 ppi metal foam.

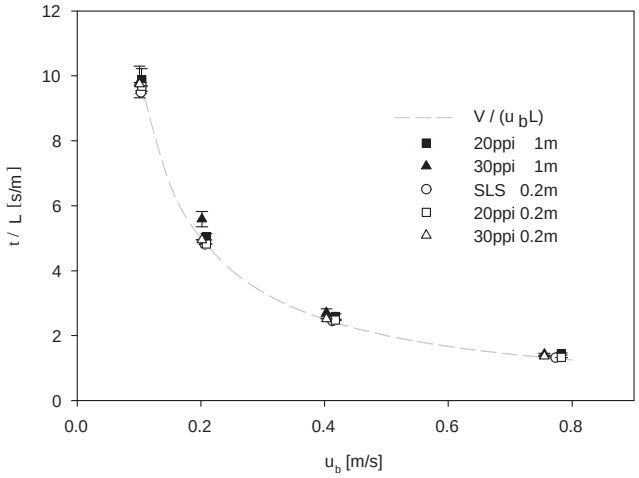

Figure 6.17: The mean residence time per unit length for all experiments (dots) in comparison to the theoretical consideration (dashed line)

experiments is compared to the theoretical residence time. All measurements correspond to the theoretical consideration and as a result no dead volumes are present in the entire reactor volume. In addition, no difference of the measurements in the longer tube arrangement compared to the short pipe can be observed. This indicates that the analytical method is not sensitive to the parameter τ and strongly reproducible.

6.3.3 Axial dispersion coefficients

In Figure 6.18 the dispersion coefficients are depicted versus the interstitial bulk velocity. The presentation of the data without taking into account the characteristic length scale of the investigated media is unusual but allows the comparison to earlier published results and it reflects the major specification for later industrial applications namely the mass flow rate. The dispersion coefficients for all experimental setups are

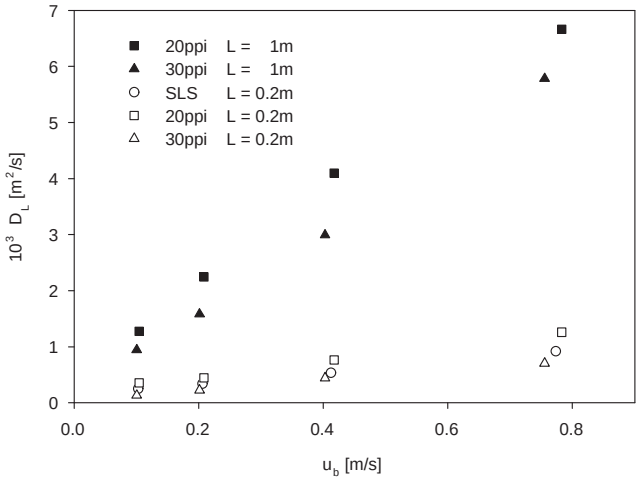

Figure 6.18: The axial dispersion coefficients are depicted versus the interstitial bulk velocity.

increasing with increasing velocity. This effect is explained by the enhanced level of induced turbulent kinetic energy and the corresponding higher mass transfer in axial but also in radial direction. The absolute values of the measured dispersion coefficients in the $1m$ setup clearly differ from the data of the short tube assembly. This influence of the length of the investigated porous media is well known from literature (Delgado [35], Han et al. [64]) but unfortunately only for fixed beds and packed columns. Different criterions were developed to define when the axial dispersion becomes independent from the column length. Han et al. [64] observed no dependency of the axial dispersion on the length of the bed for small Peclet numbers, but above $Pe_p = 700$ they observed an increase in the values of dispersion coefficients with increasing distance down the column. This can be explained by the following considerations: The Peclet number describes the ratio of the rate of advection to the rate of diffusion. With increasing Pe_p the advection, i.e. the trans-

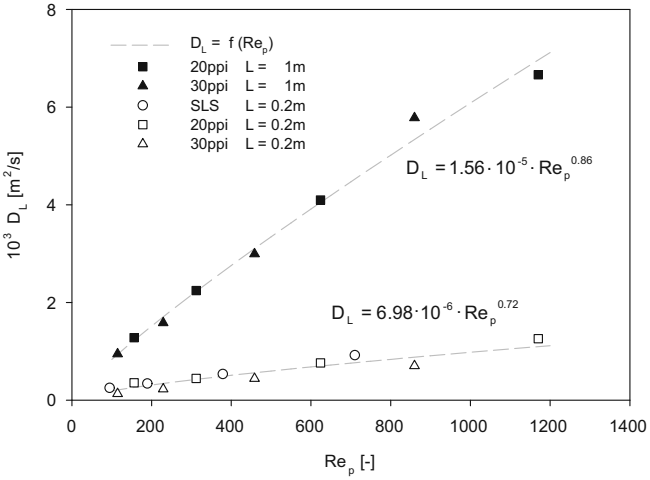

Figure 6.19: The dispersion coefficients are depicted versus the pore Reynolds number.

port of a substance by the fluid motion, becomes the dominant mass transfer mechanism. Because of the hydrodynamic entrance length it is a function of the axial position in the porous media. Thereby the mass transfer is increasing with increasing distance from the inlet as the turbulent kinetic energy is steadily increasing to its final value. Due to the high porosity of our media and the application driven high velocities we run our experiments at $Pe_p > 5 \cdot 10^4$. This high value of the Peclet number indicates that the entrance length has to be taken into account. Unfortunately there are no correlations available in literature so far, to estimate the entrance length in foam-like structures. In section 7 a very good agreement between the turbulent kinetic energy measured downstream the designed porous media of 50 mm length and the streamwise periodic large eddy simulation can be demonstrated. Since the simulation resembles the fully developed flow situation we therefore conclude that the entrance length is very short in the investigated designed porous

structure. It leads to the assumption that a length of the test section of 1 m is enough to reduce any entrance length effects. This is further confirmed by the comparison with the literature data presented in Fig. 6.20 and explained later on.

When comparing the results of the commercially available metal foams of 20 and 30 ppi at equal mass flow rates an increase of the dispersion coefficient with increasing pore size is found. This effect was also observed for the radial dispersion (see section 6.2), where the 20 ppi foam demonstrated a better mixing efficiency than the 30 ppi foam. As the foams used in those experiments were from the same supplier but slightly different in the geometry (Aluminum foam with triangular shaped ligaments) a detailed comparison of the results is not possible. Nevertheless the influence of the pore size for solid foams with the same porosity and the same ligament shape could be highlighted.

The values of the dispersion coefficients of the designed porous structure with triangular shaped ligaments were found to lie in between the values of the two commercial foams which exhibit circular strut cross sections. Due to its anisotropy the correlation between axial and radial scalar transport is not obvious. In addition there is a certain restriction in the manufacturing process for the length of the reactor and therefore only the short tube assembly could be investigated. Nevertheless an effect of the ligament shape can be seen according to the presented data. Although the porosity of the designed media is similar to the commercial foam and the pore size is decreased, it exhibits an increased axial dispersion. This is in accordance to the LES presented in section 7 observing an enhanced induced turbulent kinetic energy for triangular shaped ligaments with sharp edges compared to the ones with rounded ligaments.

To compare our results with the available literature we calculate characteristic dimensionless numbers, e.g. the Peclet number previously defined in section 3.2.3. The pore size d_p is chosen as characteristic length scale and is calculated for the circular shaped ligaments of the commercial metal foam according to Hackeschmidt [61] defined in equation 6.2. For the sintered geometry the pore size of the CAD model was used without taking into account the tolerance of the manufacturing process. Making now use of the Buckingham theorem according to Delgado [35]

it may be concluded that

$$\frac{D_L}{D_m} = \Phi\left(\frac{L}{D}, \frac{D}{d_p}, Pe_p, Sc\right) \tag{6.7}$$

The Schmidt number is constant and can be estimated for a temperature of $20°C$ as $Sc = \frac{\nu}{D_m} \approx 530$. The pore size and the ratio of the tube diameter and the length of the investigated media are also constant within a measurement series. Therefore only the effect of the Reynolds number on D_L is represented by the present data set. In Figure 6.19 the axial dispersion coefficients are depicted versus the Reynolds number based on the pore size. It is observed that the different experimental series for each setup with a certain length are similar, especially for the one meter tube case the data points show clearly the same trend with the Reynolds number. To represent the data by an empirical correlation we follow the approach of Harleman et al. [66] who proposed the dispersion coefficients as a function of the Reynolds number.

$$D_L = cRe_p^n \tag{6.8}$$

where the Reynolds number is defined as $Re_p = \frac{\rho u_B d_p}{\mu}$. The parameters c and n can be estimated under the assumption of a similar behavior of the dispersion coefficient with increasing Reynolds number by fitting equation 6.8 to the experimental data of both measurement series. The empirical correlation represents the data points of the long tube arrangement very well at pore Reynolds numbers below 700 which supports this assumption. The deviations observed at higher Reynolds numbers can be explained by the increasing measurement error at higher velocities as mentioned in section 6.3.1. In the shorter tube arrangement, where the ratio L/d_p is small, the data are more scattered. One reason could be the difficulty to install the commercial metal foam within the tube setting since it needs to be forced in. Hence small differences in the spatial porosity can occur which influences the measurement especially for short assemblies. Also the fact that the sintered structure exhibit another ligament shape has to be taken into account. This explains that the dispersion coefficients for this geometry show the largest values. However, the main reason for the data scattering is that the entrance length of a porous media is depending on its geometry. Nevertheless the fitted

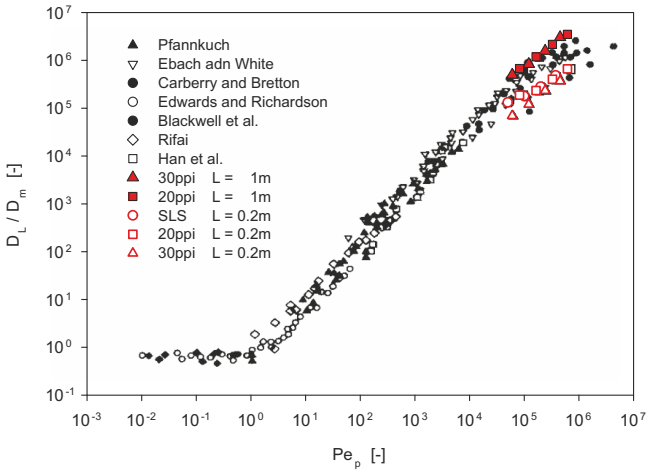

Figure 6.20: The normalized longitudinal Dispersion coefficient vs the Peclet number: A comparison of this study and data from literature collected by Han et al. [64].

curve reflects the tendency of an increasing dispersion coefficient with increasing Reynolds number with a good agreement to the experimental data.

As seen in section 2.3.2 only few studies dealt with the investigation of axial dispersion in solid foams. Most of them were performed in packed beds and due to the much smaller porosities of such systems (normally up to 40%) the investigated velocities are very small. For Raschig rings, one of the most common packing material, the situation is more comparable but still the velocities are small even for porosities ranging up to 75%. A summary of several studies is presented in Table 2.3 and a comparison to our measurements is depicted in Figure 6.20. Since our geometry features a smaller pressure drop compared to fixed beds and therefore higher velocities our data are recorded at high Peclet numbers. In general there is a good agreement with our experiments. This strongly supports the choice of the pore size as characteristic length

scale for porous media. The values of the dispersion coefficient measured for the short tube setup are smaller than the the previously published results. These values are strongly decreased due to the small L/d_p ratio. The ratio in the range of 100 to 1000 is similar to the lowest ratio reported by Carberry and Bretton [30]. These data points are represented by the full circles and it is observed that the corresponding measurements exhibit comparable values. The results of the long tube setup are slightly larger compared to literature data. This indicates that the dependency of the axial dispersion coefficient on the position in the porous media is negligible for a test section length of 1 m. Furthermore the normalized axial dispersion coefficient increases monotone with the Peclet number and we do not observe a curvature for Peclet numbers greater than 10^4, which is ascribed to turbulence effects in the porous media (Bear [3]). It is worth noting that the data showing this curvature are characterized by a low L/d_p ratio of 102 and 226 (Carberry and Bretton [30] and Ebach and White [40]). In this range we also observed decreased values for the dispersion coefficient.

6.3.4 Pressure drop

Pressure drop measurements were performed in the short tube arrangement comparing the different porous media. Different approaches to describe the pressure drop in porous media are available in literature. Since the focus of this study is not a detailed description of the pressure drop we restrict ourselves to discuss our data with respect to the Forchheimer equation (Forchheimer [51]) defined as follows

$$\frac{\Delta p}{L} = a\mu u_b + b\rho u_b^2 \tag{6.9}$$

where μ is the dynamic viscosity and ρ is the density of the fluid. Thus the frictional pressure drop consists of a viscous part, proportional to the superficial fluid velocity, and an inertia part, proportional to the square of the interstitial fluid velocity. According to Ergun and Orning [45] the constants a and b are related to the porosity ε of the investigated media and its specific surface area A_S for flow through packed beds.

$$a = \frac{\alpha A_S^2 (1-\varepsilon)^2}{\varepsilon^3} \tag{6.10}$$

$$b = \frac{\beta A_S (1-\varepsilon)^2}{\varepsilon^3} \tag{6.11}$$

where A_S is defined as the surface area per unit volume of solid. The parameters α and β depend on the geometry and the packing of the particles. Macdonald et al. [95] proposed the universal constants $\alpha = 5$ and $\beta = 0.3$ for smooth and $\beta = 0.667$ for rough particles. But most of the authors dealing with pressure loss in porous media agree, that the parameters α and β depend on the investigated media. Therefore the common procedure to assume $\alpha = 5$ and to calculate the specific surface according to equation 6.10 by means of permeametry measurements is not valid in this case. An estimate of the specific surface area is therefore needed and in this study the approach of Kozeny [81] is applied, which assumes the pores as uniform, parallel cylinders with constant diameters d_p.

$$A_S = \frac{4\varepsilon}{d_p(1-\varepsilon)} \tag{6.12}$$

Richardson et al. [128] compared this hydraulic diameter model to two other equations and found it to be the closest to the averaged values of all of them. Even if it is a simple model it arose to be sufficient for this application. The resulting specific areas are listed in Table 6.3 and they are in the same order of magnitude as the one estimated from Richardson et al. [128] for ceramic foams of comparable pore sizes. In Figure 6.21 the pressure drop for the commercial foam of 20ppi and 30ppi and for the streamwise periodic structure is depicted. As expected the pressure drop is increasing with decreasing pore size. Therefore the 20ppi foam has the smallest pressure drop followed by the 30ppi foam. The highest energy input to pump the same amount of fluid through the device was obtained for the designed porous media. The dashed lines in Figure 6.21 represent the fitted Forchheimer equation. The calculated parameters α and β are listed in Table 6.3. The absolute values correspond well with the data of Richardson et al. [128] and they are in the range suggested by Ergun and Orning [45]. Unfortunately only the results of one pore size can be directly compared. The pressure drop in case of water flowing through the device (continuous line) could be estimated by means of the parameters obtained by Richardson et al. [128] and compared to our

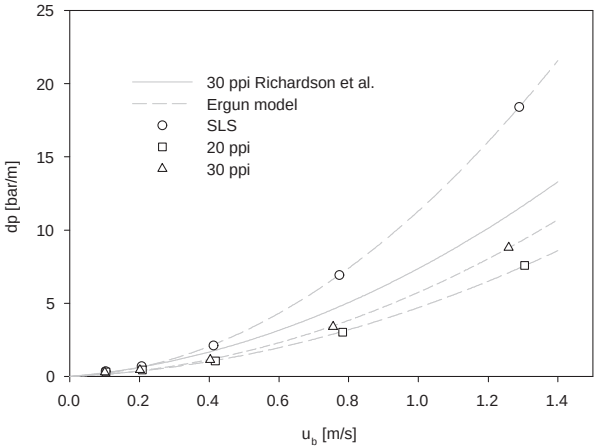

Figure 6.21: The pressure drop of the different investigated porous media is depicted vs the interstitial bulk velocity.

results. The ceramic foam has a slightly smaller pore size but a higher porosity than the metal foams investigated in this study. The pressure drop of the ceramic foam is higher compared to metal foams due to the decreased pore size resulting from the manufacturing process. By comparing all results one can see an opposite trend for the parameters α and β with respect to the pore size. α is increasing with increasing pore size and β is decreasing. While the α-values correspond to the values estimated for fixed beds, the parameter β is lower than predicted for particle beds or at the lowest range of those values. This was also established by Richardson et al. [128] who ascribed this behavior to the dependency of the parameters to the characteristics of the porous media. The clearly increased value of β observed for the laser sintered structure can be explained by the huge surface roughness compared to the commercial foam. In general the results clearly show that the approach of Ergun and Orning [45] represents well the pressure drop in solid foam or foam-like structures.

Table 6.3: Overview of the estimated Ergun coefficients and the theoretical specific surface area.

	Structure	$\mathbf{A_s \cdot 10^{-3}}$	α	β
Richardson et al. [128]	30 ppi	33.6	7.72	0.084
This study	20 ppi	13	13.23	0.092
	30 ppi	21.5	6.92	0.100
	SLS	22.8	4.64	0.167

6.3.5 Conclusions

Commercially available metal foams of two different pore sizes (20 and 30ppi) were investigated in terms of the longitudinal dispersion behavior and compared to a designed streamwise-periodic structure for mass flow rates ranging from $0.2 - 1.5\,\mathrm{l/min}$. In all cases narrow residence time distributions were observed indicating a global plug flow behavior of the investigated structures. Due to the high porosity of the material and the thereby enabled high velocities, the applied Peclet numbers are clearly in the upper range compared to studies available in literature. Dispersion coefficients in the range of $1.3{\cdot}10^{-4}\,\mathrm{m^2/s}$ to $6.7{\cdot}10^{-3}\,\mathrm{m^2/s}$ were observed. They follow the trend of packed beds and common packing materials and increase monotone with the Peclet number Pe_p. A strong influence of the length of the investigated foam elements was observed which is a known effect from literature. The pressure drop in the porous media follows the Forchheimer equation and could be described by the conventional Ergun model. The fitted parameters are in good agreement to literature results.

6.4 Heat transfer

Measurements were performed at five different flow rates ranging from 200 ml/min to 2500 ml/min. The corresponding empty tube Reynolds numbers varied from 600 to 7600, while Reynolds numbers based on the pore size varied from 95 to 1950. Four different configurations were tested with the experimental setup described above. Commercial foam

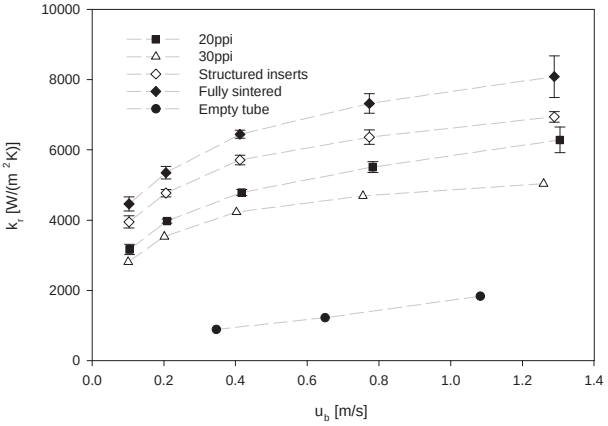

Figure 6.22: The total heat transfer coefficient as a function of the interstitial bulk velocity. The error bars indicate the standard deviation from five independent experiments, each taking the post processing of the data into account.

made of copper with 20 and 30 ppi and a designed laser sintered porous medium were inserted into the empty tube arrangement. A fully sintered reactor was also tested in the same way as the other foam elements. The Richardson numbers, calculated from $Ri = \frac{g d_p}{u_b^2}$, ranged from 0.007 to 0.14 indicating that buoyancy forces were negligible in the given forced convection regime.

6.4.1 Heat transfer coefficient

In Figure 6.22 the total radial heat transfer coefficient k_r is depicted versus the interstitial bulk velocity. Values up to about $8\,\mathrm{kW/(m^2K)}$ ($4.5\,\mathrm{MW/(m^3K)}$ based on fluid volume) were achieved and this represents an increase of 3 orders of magnitude compared to conventional batch reactors ($0.2-5\,\mathrm{kW/(m^3K)}$). The heat transfer for inserted porous media is more than four times higher, over the whole range of flow rates,

compared to the empty tube reference case. This is explained by the higher specific surface area and the greater fluid turbulence, leading to enhanced forced convection. For the commercially available foam the heat transfer is observed to increase with increasing pore size, and also ligament thickness, which corresponds to the hydrodynamic investigations presented in section 6.2 and 7.3. We found that the turbulent kinetic energy is enhanced in structures with thicker ligaments, leading to enhanced mass transfer in the axial and radial directions. The additional increase ($> 10\%$) in the total heat transfer coefficient for the fully sintered structure was not expected, even though Hackeschmidt [61] observed an effect of the wall connection on the heat transfer efficiency.

In Figure 6.23, the pseudo convective heat transfer coefficient is presented versus the pore Reynolds number. Similar to the conclusion of the axial dispersion measurements (section 7.4, the use of the pore size as the characteristic length scale seems to be valid also in the case of heat transfer. The data series match well over the investigated range of Reynolds numbers and show exactly the same trend approximated by a power law for visualization purposes. The comparison of commercial metal foam with the designed porous media yields some surprising results. Although copper has a high heat conductivity (more than $200\,\mathrm{W/(mK)}$) in comparison to the high alloyed steel ($13\,\mathrm{W/(mK)}$), the pseudo convective heat transfer coefficient of the sintered structure is much higher, even without wall connection. The strongly elevated convective heat transfer for the designed structure can first be ascribed to the triangular shape of the ligaments, which are favorable in case of heat transfer as already observed by Hackeschmidt [61] and further discussed in more detail by means of a large eddy simulation in section 7.3. The triangular shaped ligaments of the designed media were found to induce more turbulence compared to the circular struts of the commercial metal foam. This led to an enhanced mass transfer characterized by the homogenization of a tracer dye in water, visualized by applying a laser induced fluorescence technique. The analogous increase in heat transfer is secondly affected by the bigger surface area of the sintered foam. The basic geometry, which is somehow the negative pattern of a packed bed, exhibits an enhanced specific surface. In addition, the manufacturing process produces a rough surface as depicted in Fig. 1.2. The structure is covered by stainless steel particles with a mean diameter of $20\,\mu\mathrm{m}$. These particles are

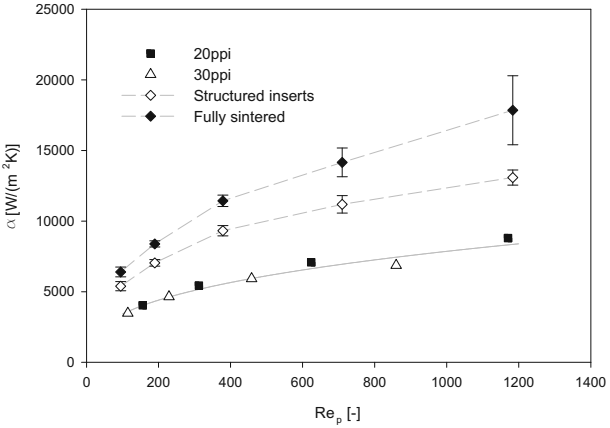

Figure 6.23: The pseudo convective heat transfer coefficient as a function of the pore Reynolds number. The error bars indicate the standard deviation from five independent experiments each taking the post processing of the data into account.

derived from the metal powder used to generate the three dimensional geometry by SLS.

Finally the fully sintered reactor exhibits a convective heat transfer coefficient which is more than two times higher compared to the commercial metal foam. This is attributed to improved heat dissipation through the sintered elements. The designed ligaments have a larger cross section with equivalent porosity compared to commercial foam. The gap between commercial foam elements and the tube wall is an additional heat transfer resistance. This results in a lower steady state temperature of the solid foam during operation as the heat conduction from the wall towards the center of the tube is limited and leads to a decrease in convective heat transfer.

6.4.2 Comparison with literature data

The experimental configurations reported in literature vary considerably and this accounts for much of discrepancy between experimental results. The parameters controlling the heat transfer through solid foams were summarized in section 2.3.3. Due to the standard manufacturing process for commercially available foam, most of those parameters are linked to each other. Changing one parameter leads to different heat transfer mechanisms and this makes it difficult to predict the impact of variations in geometry. In general the heat transfer is strongly case specific and only a qualitative comparison is possible for similar cases.

We first compare our results with the experiments of Hackeschmidt [61] who investigated the same commercially available foams used in this study. Many of his conclusions are consistent with the results in this work. The increased heat transfer for the 20 ppi foam in comparison to the 30 ppi foam can be ascribed to the higher turbulence induced by this structure due to the thicker ligaments. The effect of the wall connection, investigated by Hackeschmidt [61] was also discussed in this study, by the aid of a reference geometry. The strongly elevated heat transfer coefficient for the fully sintered structure in comparison to the structure without wall connection could be ascribed to improved heat conduction from the wall towards the center of the tube. Hackeschmidt [61] addressed the impact of the ligament shape on the heat transfer coefficient by comparing commercial metal foams with differently shaped cross sections. He concluded that the heat transfer was strongly elevated for triangular shaped ligaments compared to circular ones, which is consistent with our experimental results. The comparison of those results is, however, qualitative as the basic cell structures differ from each other.

[26] investigated the effect of foam compression on thermal performance. Comparison of the present work with their study requires calculation of the Nusselt number with the hydraulic diameter d_h of the test section:

$$Nu = \frac{\alpha d_h}{\lambda_f} \tag{6.13}$$

where α is the convective heat transfer coefficient and λ_f is the heat conductivity of the fluid, in this case water. In Figure 6.24, the Nusselt numbers are depicted as a function of the clear channel velocity. In the

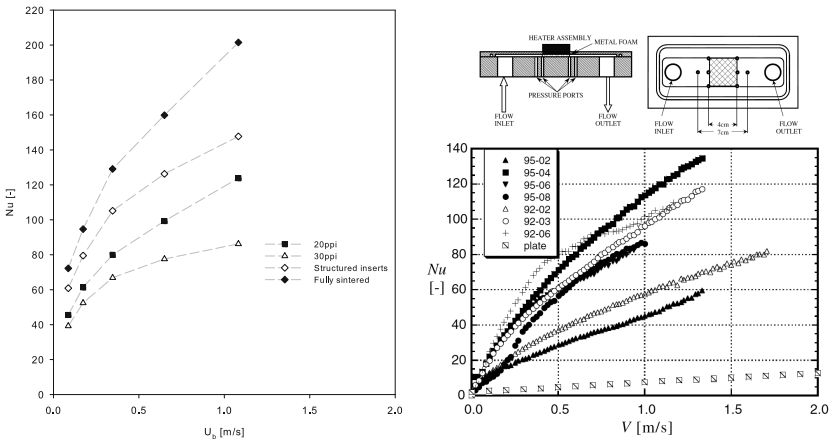

Figure 6.24: Comparison of Nusselt numbers estimated according to the method of Boomsma, Poulikakos and Zwick [26]. Values from this study are depicted on the left, data from Boomsma and Poulikakos are on the right. In the legend of the reference data the first two digits of the sample name designate the porosity of the foam in pre-compressed form. The second pair of numbers after the hyphen signifies the compression factor. In the upper right corner the setup used by Boomsma and Poulikakos is depicted.

present work, the Nusselt number increases in the range of 40 to 200 with increasing velocity. The same trend is observed in the reference data but the range of values is somewhat lower (< 140).

The influence of foam compression is hard to interpret and the authors do not comment on this in detail. The heat transfer increases with increasing compression up to a certain point but then it decreases. This can be explained by different mechanisms. The interstitial bulk velocity increases with decreasing pore size and therefore the convective heat transfer is enhanced. At the same time, the surface area increases leading to an enhancement of the heat transmission. The effective thermal conductivity also increases due to the higher density of the solid

material. The decrease in heat transfer at higher pore densities could be ascribed to the increasing laminar flow with decreasing characteristic length. It is nevertheless a fact that compression of the foam produces a very undefined structure with inhomogeneities in the porosity. Therefore, there is a certain optimum degree of compression that would be however difficult to reproduce.

At the highest velocity used in this study (1.1 m/s), the maximum Nusselt number obtained is around 1.7 times higher than the corresponding maximum value reported by Boomsma, Poulikakos and Zwick [26]. However, direct comparison such as this is difficult as the experimental setups were completely different. The setup for the reference data consists of a metal foam sample with dimensions of $40 \times 40 \times 20mm^3$ (Figure 6.24 above). The foam is heated from the top by a heating block made of copper. The convective heat transfer was calculated according to

$$\alpha = \frac{\dot{m} c_p (T_{out} - T_{in})}{A_{con}(T_{pl} - T_{in})} \tag{6.14}$$

where A_{con} is the interfacial area between the foam sample and the heat spreader plate, T_{in} and T_{out} the fluid inlet and outlet temperatures and T_{pl} the plate temperature. In our setup, the heat exchange surface is the whole inner wall of the tube. This surface area was used to calculate the convective heat transfer coefficient (equation 3.53) and explains the difference in the absolute values. Furthermore, Kurtbas and Celik [88] showed in their investigation that the cross sectional aspect ratio of the porous media influences the thermal performance. A circular cross section can be assumed to be superior to the rectangular surface used by Boomsma, Poulikakos and Zwick [26] (aspect ratio of 0.5).

6.4.3 Pressure drop and efficiency

In Figure 6.25, the pressure drop data of inserted commercially available foams and designed sintered inserts are compared to the fully sintered reactor. The pressure drop for the sintered insert is intermediate to the fully sintered structure, which exhibits the highest pressure drop, and the commercial metal foam. Although the structure of the designed insert matches the dimensions of the tube within a tolerance of 0.1 mm, the pressure drop is much lower compared to the fully sintered device.

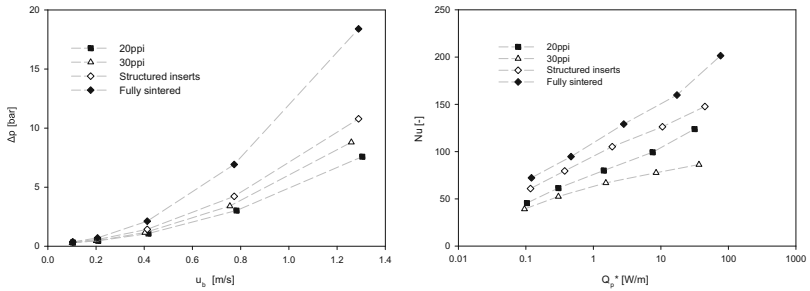

Figure 6.25: Pressure drop data of the different solid foams versus the interstitial bulk velocity on the left. On the right, the Nusselt number is presented versus the pumping power needed to convey the fluid through a tube of 1 m length.

The porosity of the designed insert increases near the wall and a small gap allows fluid to pass through. This by-passing leads to a decreased pressure drop. In addition the roughness of the inner wall is much smaller for the inserted structured elements, as a commercial stainless steel tube was used. This partially explains also the smaller pressure drop for the commercial metal foams. But the main reasons for the decreased pressure drop of commercially available foams compared to the designed structure is the slightly increased porosity and the smoother surface of the foam.

The heat transfer efficiency can also be demonstrated by taking into account the energy consumed to pump the fluid through the device. The pressure drop data can be used for this purpose. Figure 6.25 also shows the Nusselt number versus the pumping power calculated from the pressure drop $\triangle p$ and the volumetric flow rate $\dot{V}$ according to equation:

$$\dot{Q}_p = \dot{V} \triangle p \tag{6.15}$$

The energy required to pump the fluid is relatively small compared to that transferred to the fluid. The Nusselt number increases with increasing flow rate and pumping power, since the energy input to the flow induces turbulence and a much higher convective heat transfer.

However, there is no direct correlation between the energy consumed and the energy transferred. For example the 20 ppi foam exhibits a smaller pressure drop than the 30 ppi foam, but features a better heat transfer performance. Thus the heat transfer is partially decoupled from the pressure drop which was also observed in the mass transfer studies of Ferrouillat et al. [47] and the investigations presented in section 6.2. The same is true for the inserted sintered structure which however exhibits a slightly higher pressure drop. It performs best of the investigated inserts although the copper has much higher heat conductivity in comparison to stainless steel. Due to the wall connection, the fully sintered reactor exhibits the best overall performance and offers the highest Nusselt number at constant pumping power.

6.5 Conclusion

The heat transfer enhancement by metal foam inserts was studied in a range of empty tube Reynolds numbers ranging from 600 to 7600 in the forced convection regime. Compared to the empty tube case the metal foam inserts lead to an increase in heat transfer, which is up to 10 times higher. A strong influence of the geometry of the structure was shown. For commercially available metal foam an increase of the pseudo convective heat transfer with increasing pore size, ascribed to the bigger ligament thickness, could be observed. Also the shape of the ligaments was found to have a huge influence on the heat transfer performance. The effect of a fixed wall connection was studied by the aid of a reference geometry with and without wall connection. A big difference in the heat transfer rate was found. In case of the fully sintered device the pseudo convective heat transfer rate was found to be in average 30% higher compared to the sintered structure without wall connection.

Chapter 7

Numerical simulation

Within this section we present the results of a dynamic large eddy simulation and compare them to data originating from PIV in terms of induced turbulent kinetic energy and to pressure drop measurements. After the discussion of the grid convergence we validate the LES approach by means of a reference simulation case where to the periodic computational domain an empty tube domain is added with an axial extent of 2D as depicted in Figure 7.1. Afterwards we compare the experimental results with the simulation downstream the porous media and we discuss the results for the different simulations with periodic conditions in comparison to experimental results from the streamwise periodic media and commercial metal foams. Finally we analyze the strong impact of the geometry on the pressure drop and the turbulence induced by means of comparing the original geometry with the adapted one which corresponds to the final transparent polymer model.

7.1 Grid convergence

An unstructured tetrahedral grid was applied to all of the streamwise-periodic configurations presented due to the complexity of the porous geometry. The mesh was generated with the commercial Software Gambit®. In order to apply periodic boundary conditions the surface

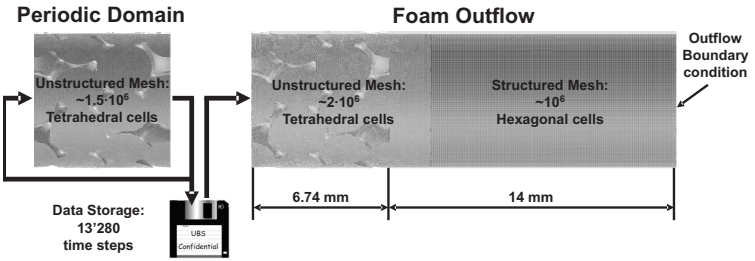

Figure 7.1: Schematic illustration of the procedure for the calculation of the empty tube reference case. 13250 transient velocity fields were stored from the corresponding periodic domain and read into the reference case at every time step at the inlet boundary.

mesh of the inlet and outlet of the computational domain has to match. To quantify the quality of the grid size the volume of the computational cells were compared to the Kolmogorov scale.

$$\frac{\Delta V^{1/3}}{\eta} \tag{7.1}$$

where the Kolmogorov scale was estimated by replacing the energy dissipation rate ϵ by $\frac{U_b^3}{d_p}$ where U_b is the bulk velocity and d_p is the pore size.

$$\eta = \left(\frac{\nu^3}{\epsilon}\right)^{1/4} \tag{7.2}$$

The ratio between the cell size and the Kolmogorov scale was always below 10 for all performed simulations. For the basic reference geometry described in section 6.1 different mesh sizes were studied to assure the grid convergence. The coarsest grid is grid 1 with a characteristic length of 0.09 mm. Half of this length was set for grid 2 which increases therefore the number of tetrahedral cells in the computational domain by a factor of 8. For grid 3 an adaptive grid (based on grid 1) was used with y^+ as control variable. If y^+ exceeded a critical value of 5 the characteristic length of the corresponding cell was bisected. All cases were compared in terms of pressure drop and fully developed flow field. Despite the decrease of the y^+ values for the higher resolved computational

domains the pressure drop was reproduced for all cases with an accuracy of about 5%. Therefore all simulations were performed with a mesh size corresponding to grid 1 which allows to set the biggest time step. The characteristic values for the different cases are listed in Table 7.1.

7.2 Solution procedure

To solve the numerical problem the commercial software Fluent® was used. The simulation was parallelized on 8-16 CPUs (Quad-Core AMD Opteron Processors 8380, with 2500 MHz CPU speed) of the Brutus Cluster at ETH Zurich. The simulations were performed with a pressure based solver and a specified mass flow rate. The detailed description of the numerical model applied is described in section 3.1.3. The time step was estimated by the Courant-Friedrichs-Lewy (CFL) condition (Pope [120])

$$CFL = \frac{|\mathbf{u}|\Delta t}{\Delta V^{1/3}} \leq 1 \tag{7.3}$$

where $\Delta V^{1/3}$ is the characteristic length of a mesh volume. The purpose of the CFL condition is to guarantee stability and temporal resolution. The resulting time steps for the simulations are in the order of 10^{-6} s. The LES model in Fluent® automatically adjusts the bounded second-order central differencing scheme for convection discretization. Diffusion terms are discretized by the central second-order differencing scheme. For the time integration a fully implicit second-order scheme was chosen. Pressure and velocity were coupled by SIMPLE scheme (*FLUENT 6.3 User's Guide* [50]). Gradients were discretized by the Green Gauss cell based method. After initializing the computational domain with an isotropic turbulent flow field the simulation runs for about $4 \cdot 10^4$ time steps to develop the flow field. The velocity was monitored at several coordinates of the computational domain to observe the transient response of the simulation. After reaching a fully developed flow field the collection of turbulent statistics (velocity fluctuations, turbulent kinetic energy, energy dissipation rate) was started over a similar period of time until the values were stable. Table 7.1 shows an overview of all computational cases with the corresponding Reynolds numbers, time steps and the number of mesh volumes.

Table 7.1: Overview of all different computational domains.

Computational domain	Re	Re_p	Cell volumes	y^+_{max}	Time step [s]
Adapted periodic	1200	220	1110092	4.2	$2 \cdot 10^{-5}$
Adapted periodic	2400	450	1110092	6.3	$1 \cdot 10^{-5}$
Adapted periodic	4500	840	1439502	8.1	$5 \cdot 10^{-6}$
Original periodic	4500	760	1027124	12.0	$5 \cdot 10^{-6}$
Empty tube case	4500	840	2853113	8.1	$5 \cdot 10^{-6}$

7.3 Results

Within this section we discuss the simulation results and compare them to data originating from PIV and PLIF measurements. After the validation of the numerical results we first address the complex velocity field inside the porous structure as predicted by the LES. In addition we analyze the strong impact of the geometry on the pressure drop and the turbulence induced by means of comparing the original geometry with the adapted one corresponding to the final plastic model. This is followed by the comparison of the experimentally and numerically obtained turbulent kinetic energy downstream of the porous structure. And finally the mixing efficiency of the designed foam is addressed.

7.3.1 Validation

A major problem of the experiments is the available measurement domain. PIV can only be performed downstream of a static mixing element and always only two components can be resolved in the plane of measurement. The comparison of the simulation results performed within the structure with the experimental data measured downstream has to be examined. Therefore a computational domain was designed combining a streamwise periodic structure with an empty tube, depicted in Figure 7.1, in the following called empty tube case. The empty tube domain had to be restricted to a length of 2 times the diameter due to the computational costs as the domain already consists of 2.9 Mio cells. The comparison to the experimental results was done for the highest Reynolds number investigated ($Re = 4500$). Therefore a set of about 13000 temporal velocity fields were stored from the periodic simulation

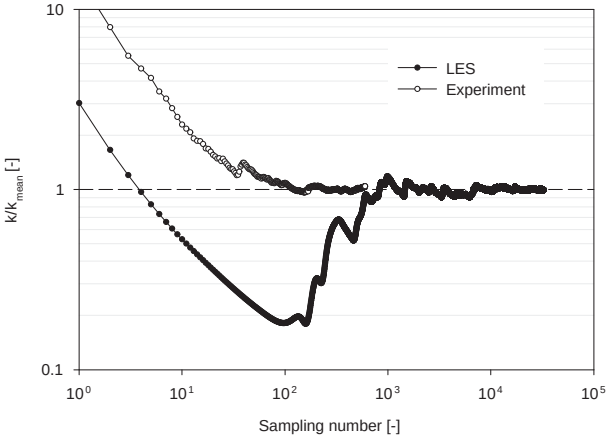

Figure 7.2: Development of the turbulent kinetic energy with the sampling number for the case of Re=4500 at a point 12 mm downstream the porous media in the center of the tube.

of the foam. Those data were used as inlet condition for every single time step for the empty tube case. The outlet of the tube was defined by an outflow condition. In Fig 7.1 the procedure is clarified. By comparing the velocity field two major challenges has to be taken into account. First the computational domain is limited in its length and the outflow condition influences the downstream flow field. The comparison of the experimental data should be performed away from the outlet. A second problem are the different time scales of the experiments compared to the simulation. On one hand we record a set of 600 double frames for PIV analysis with a frequency of 4 Hz. For the simulation on the other hand statistics are collected over about $4 \cdot 10^4$ time steps which have a total duration in the order of 10^{-1} s. This difference in the examined time window of 3 orders of magnitudes has to be discussed. Therefore the velocity fluctuation in the simulation of a point in the center of the empty tube domain 12 mm downstream the porous media is compared to the experimental fluctuation from one image to another at the same lo-

cation. An oscillating flow mechanism can be described by the Strouhal number defined as follows.

$$Sr = \frac{f \cdot l}{u_b} \tag{7.4}$$

where f is the frequency of vortex shedding, l the characteristic length of the object disturbing the flow and u_b the interstitial bulk velocity. For the simplified assumption of a cylinder in a flow field the Strouhal number is 0.2. By defining the pore size as characteristic length scale for the porous media the frequency for Re=4500 result in 302 Hz. A value of 300 Hz could also be estimated by the consideration of the spectrum of the turbulent kinetic energy of the numerical time series at a well defined point. This means that the simulation fully resolves the velocity fluctuation but not the experiment. The experimental data is a random sampling of the velocity field and therefore depending on the number of images used for the analysis. We discussed in chapter 4.2.1 that a set of 600 double frames is adequate to describe the present flow situation. The following consideration fully supports this statement. In Figure 7.2 the normalized mean turbulent kinetic energy is depicted versus the sampling number for the experiment (number of frames) and the simulation (time steps) at the above defined location in the center of the tube. The energy is calculated according to equation 3.52 using the two different velocity components resolved in the plane. The radial component is therefore added twice in assumption of locally isotropic turbulence. One can see clearly that in both cases a stable value is reached. The mean kinetic energy runs through a minimum in case of the simulation and for the experiments it decreases virtually monotone to the final value. It is obvious that the random sampling strategy used in the experiment is very efficient and the set of 600 double frames is clearly enough to estimate a mean turbulent statistic. For the simulation which exhibits a high temporal resolution a much higher amount of snapshots is needed to calculate the mean statistics as the frequency of the velocity fluctuation is much smaller than the frequency of the sampling. In addition the mean velocity field is continuously calculated for every time step. It takes several iterations as it becomes stable. Even the time window of the simulation is on the lower end to calculate mean turbulent statics the results correspond very well to the experimental data, presented in

detail in the following chapters.

7.3.2 Velocity fields and pressure drop

Figure 7.3 depicts a sliced quarter of the computational domain showing the LES results for the case of Re = 4500 and periodic boundary conditions. In the upper image two different planes orthogonal to each other with the corresponding mean velocity fields are depicted. The contour plot in the background represents the axial velocity component. In the lower representation an isosurface of the axial velocity component at a value of 1.2 m/s is shown. At every ligament the flow is separated and accelerated through the pores into the neighboring cells in flow direction. This lamination of the flow is often used in static mixing elements to recombine two fluid streams to decrease the mixing length. In those cells the jets of all neighboring cells upstream are decelerated leading to vortex formations and a very complex three-dimensional flow. Due to this deceleration and vortex formation the recombined fluid streams are intensively mixed before the fluid is accelerated into the following cells downstream. The observed flow characteristics with alternating velocity combined with the lamination effect leads to a very good mixing efficiency. The numerically obtained pressure drop is compared to measurements of the laser sintered and the stereolithographic manufactured foam for a range of Reynolds numbers ranging from 600 to 7600. In Figure 7.4 the results are depicted versus the interstitial bulk velocity. The porosities of the SL model was assumed to be equal to the one of the adapted CAD model (78%). For the sintered geometry a gravimetric method was applied to estimate the porosity to 84%. The pressure drop calculated by the periodic LES is smaller than the one estimated by means of measurements. It is about 20% decreased compared to the plastic model and around 40% lower compared to the sintered case. By comparing the roughness of the different samples the difference in pressure drop becomes evident. In the simulation no additional surface roughness was defined, i.e. the simulated model has a completely smooth surface, whereas the plastic model exhibits a wavy surface due to the manufacturing process. Even a bigger impact on the surface roughness is given by the SLS where a powder with a mean grain size of about 20 μm is melt to the final geometry. This process leads to a surface with

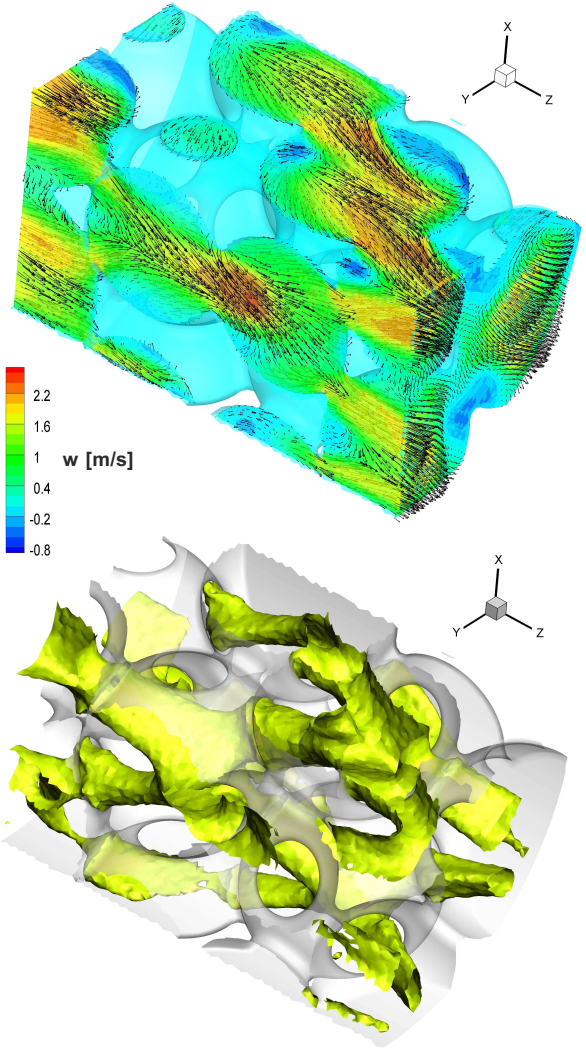

Figure 7.3: A quarter slice of the computational periodic domain for a Reynolds number of 4500. In the upper illustration the velocity field is depicted for two different planes with the contour plot of the streamwise velocity component in the background. The lower image shows the isosurface of the streamwise velocity component at a value of 1.2 m/s.

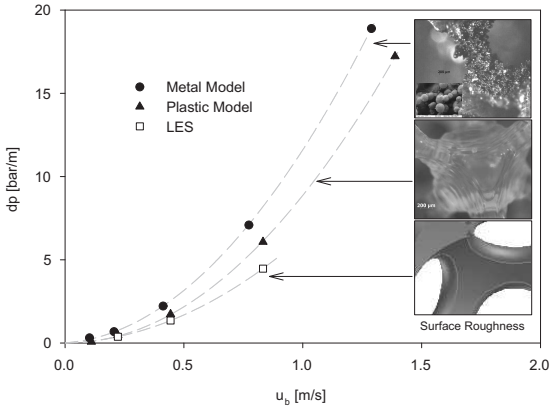

Figure 7.4: Comparison of pressure drop depicted versus interstitial bulk velocity.

a roughness in the order of the grain size as the grains of the top layer are not fully molten and only stick to the surface. In addition to the difference in surface roughness the shape of the ligaments is also important. The pressure drop for the triangular shaped geometry at a Reynolds number of 4500 was estimated to 14.87 bar/m. This value is remarkably larger compared to the one observed for the adapted geometry. Hence the pressure drop is increasing with decreasing pore size which was also observed for commercial metal foam elements. A major objective of the LES performed is to describe and analyze the flow characteristics caused by the structure to deliver optimization parameters. As seen the influence of slight changes in the geometry is huge when comparing the pressure drop of the original structure with the adapted one. In Figure 7.5 we first compare the velocity fields within the two different geometries in the two planes orthogonal to the radial direction. A difference in the resulting velocity fields is evident which can be related to the changes in geometry. For the sharp edged case the momentum of the flow by the jets is locally larger compared to the geometry with round edges due to the prevailing smaller pore size. However, it has to be stated that the

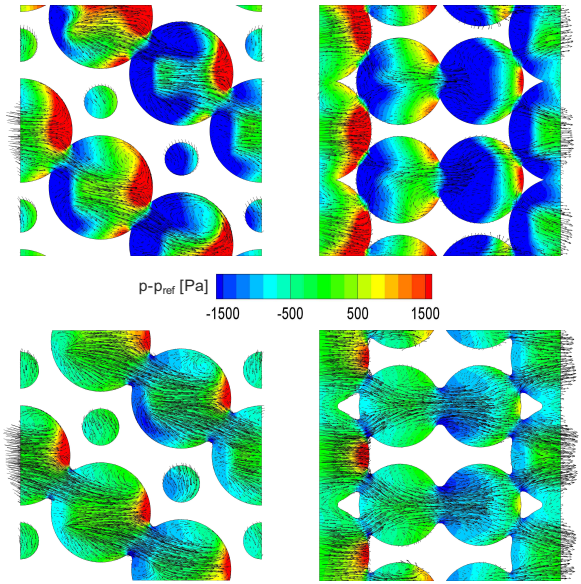

Figure 7.5: Above the velocity field of the original structure in comparison to the adapted model below. The relative pressure is depicted as contour plot in the background.

decrease of the pore size is only marginal between these two cases, and therefore the difference in pressure drop cannot be solely attributed to this change in geometry. In addition the wakes downstream of the sharp pores are much further developed compared to the rounded edges which leads to stronger vortex formation around the ligaments. This has an strong impact on the pressure field which is shown as contour plot in the background. In the narrow pore channels and following expansion zones the pressure is strongly decreased in respect to the reference pressure of $1.0133 \cdot 10^5$ Pa. Those regions of decreased pressure are bigger in case of sharp edges due to the stronger separation at the ligaments. This effect is visualized in Figure 7.6 where the differences in streamlines with respect to the ligament shape are depicted. For the sharp edged ligaments the stagnation points of the flow upstream of the ligament and the

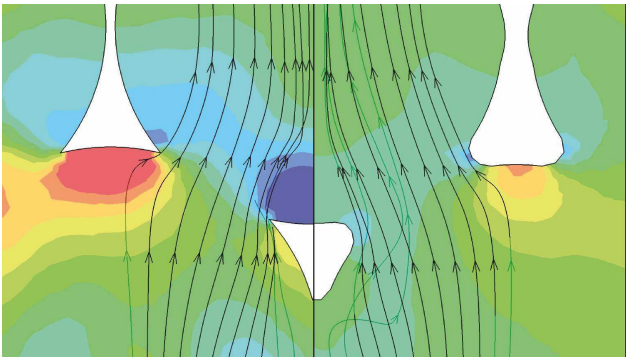

Figure 7.6: Difference in streamlines with respect to the ligament shape. The relative pressure is depicted as contour plot in the background.

recirculation zone downstream are clearly defined by the geometry and are identified by the large zones of increased (red) and decreased (blue) pressure compared to the reference pressure of $1.0133 \cdot 10^5$ Pa. These regions are less prominent for the ligaments featuring round edges since the streamlines are able to attach to the geometry and therefore flow separation is delayed. Thus we conclude that the shape of the ligaments has a dramatic influence on the hydrodynamics. To describe the influence of the geometry on the induced turbulence the root mean square (RMS) values of the streamwise velocity component w are presented in Figure 7.7 for both geometries. Zones of high velocity fluctuations are replicated with the periodic length. In every cell not adjacent to the wall three zones of strongly increased RMS values can be seen arising from the jets entering the cells. Those zones are bigger and more intensive in case of sharp edges and smaller pores. The assumption of Ferrouillat et al. [47] that the turbulence is increased with increasing hydraulic diameter of the ligaments is supported by our results. For the rounded edges a hydraulic diameter of 0.52 mm was estimated which increases to a value of 0.56 mm for the geometry with sharp edges. However, as stated above, the influence of the geometry of the cross section itself on the hydrodynamics plays an important role as well. The sharp edges lead to an enhanced mass and heat transfer which was observed

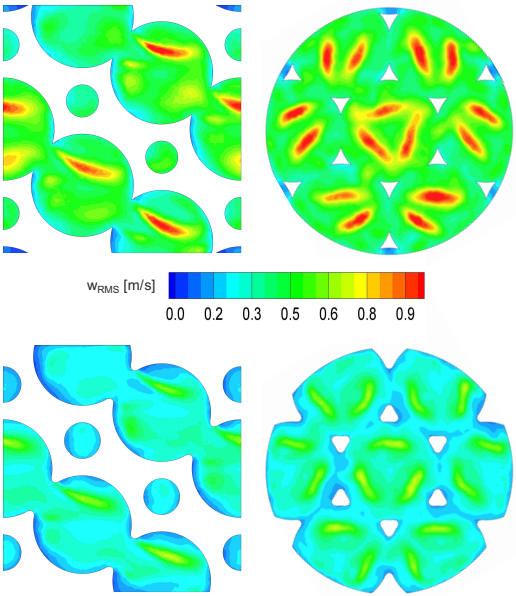

Figure 7.7: Above the root mean square of the axial velocity component of the original structure in comparison to the adapted model below.

by Hackeschmidt [61] in a study investigating commercial metal foams with circular shaped ligaments in comparison to triangular shaped ones. The latter exhibit a much higher convective heat transfer which can be explained by the stronger wakes and the induced turbulence. As shown in the next section a comparison of the spatially averaged turbulent kinetic energy yields an increase by a factor of about 3 comparing the geometries with sharp and rounded edges.

7.3.3 Turbulent kinetic energy

The contour plot of the mean temporal turbulent kinetic energy for the simulation and for the experiment is depicted in Figure 7.8. The same plane of interest was chosen for both cases and the turbulent kinetic energy was calculated only by the resolved velocity components, therefore

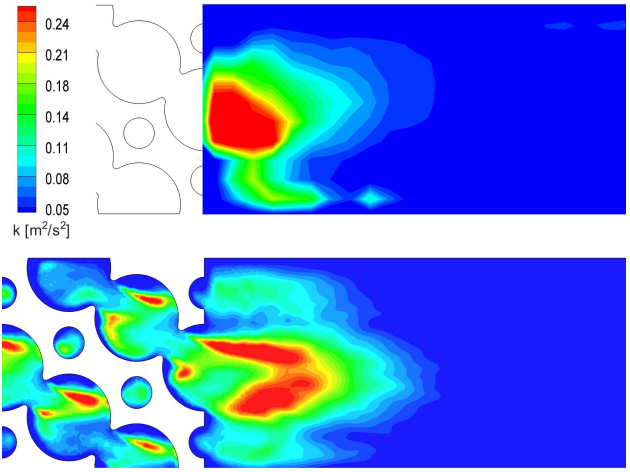

Figure 7.8: Comparison of the contour plot of the spatially resolved turbulent kinetic energy for the experiment (above) and the LES (below) at Re=4500.

for the LES the RMS values of the fluctuations were defined as

$$u_{rms} = \sqrt{\frac{1}{n}\sum_{i=1}^{n}(u_i - \overline{u})^2}. \tag{7.5}$$

The root mean square of the velocity fluctuations is averaged over the time of the experiment, i.e. the number of images n. The mean spatially resolved turbulent kinetic energy is in good agreement between the simulation and the experiment. The jet leaving the foam element in the center of the tube is strongly present. It leads to a zone of maximum kinetic energy downstream the foam element in the tube center which can be observed in the simulation respectively the experiments. The three different graphs (full dots) in Figure 7.9 depict the spatially averaged quantity within three consecutive equally sized regions (with an axial extend of 0.5D) downstream of the porous media for Reynolds numbers of 1200, 2400 and 4500. As expected the turbulent kinetic energy is increasing with increasing Reynolds number. In axial direction a

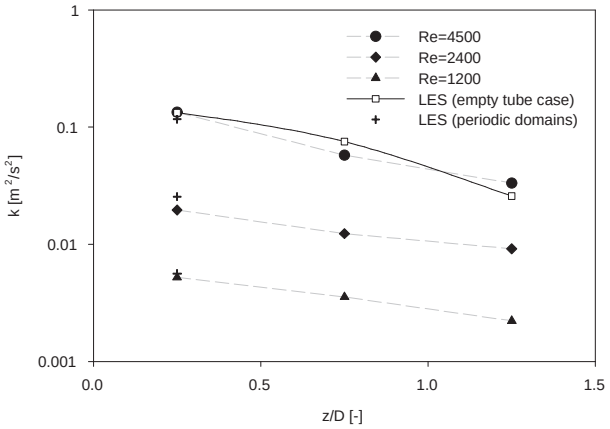

Figure 7.9: The turbulent kinetic energy versus the position downstream the streamwise-periodic media. The experimental data (full symbols) are compared to the reference LES case (empty symbols).

fast decrease of the kinetic energy with increasing distance to the foam can be observed. This was already shown in section 6.2 addressing the velocity field behind commercial metal foams of different pore sizes and the designed porous media. Since PIV only resolves one radial velocity component we assume for the calculation of the turbulent kinetic energy that the unresolved radial component equals the resolved component. We adopt this procedure for the calculation of the turbulent kinetic energy from the LES data for comparison purposes. The difference between these values and the fully three-dimensional turbulent kinetic energy resolved by the LES is about 5%. This difference is caused by the fact that the velocity fluctuation normal to the investigated plane is smaller and therefore the fully resolved mean turbulent kinetic energy is slightly decreased. Nevertheless the simulation and the experiments are very consistent. The kinetic energy is decreasing with increasing distance from the outlet in a linear way as observed in the experiments. The cross symbols in Figure 7.9 depict the values of the turbulent kinetic energy of

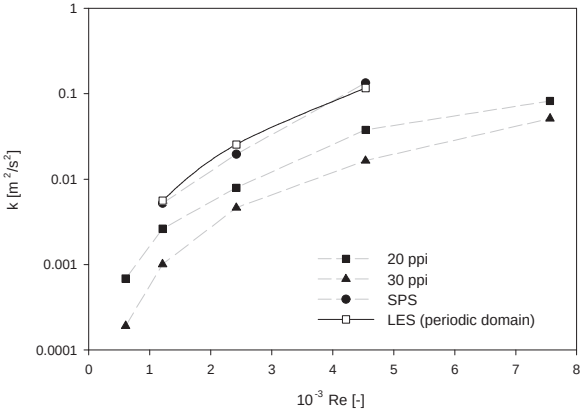

Figure 7.10: Turbulent kinetic energy of the streamwise-periodic structure versus the Reynolds number in comparison to commercial metal foams.

the periodic foam simulations spatially averaged over the computational domain for the three different Reynolds numbers. Comparing these values with the spatially averaged experimental results a small deviation is observed. However, the turbulent kinetic energy measured immediately downstream of the porous structure reflects the kinetic energy within the porous media in a satisfying manner. This can also be seen in Figure 7.10 where the turbulent kinetic energy is depicted versus the Reynolds number. Comparing the spatially averaged turbulent kinetic energy of the periodic computational domain and the corresponding experiment with the measurements of commercial metal foams of 20 and 30 ppi enhanced values for the designed structure are observed. The pore size of the designed structure is smaller compared to the commercial metal foams for which we observed in section 6.2 an increase of the turbulent kinetic energy with increasing pore size. This contrary behavior of the designed structure was explained by the difference in the geometry of the porous media. Ferrouillat et al. [47] ascribed the decreasing micromixing time measured for different foams with increasing pore size to

an increased turbulence induced by the thicker ligaments which supports the formation of vortices. This assumption is based on the investigations of Lu et al. [94] in which the metal foam is regarded as an arrangement of vertical and horizontal tubes. The ligaments of the designed porous media studied in this work are thicker than the ones of the commercial metal foams and additionally their pore size is decreased.

The increased values for the turbulent kinetic energy lead to an enhanced mixing efficiency addressed in section 6.2.2. The results have shown that the mixing efficiency is strongly influenced by the geometric characteristic of the considered metal foams. The two effects of flow lamination and convective mixing were assumed to be the major reason for the enhanced scalar transport. The enhanced turbulent kinetic energy induced for the designed streamwise periodic structure leads to an increased mixing efficiency compared to commercial metal foams which was finally proven by the LIF experiments.

7.4 Conclusions

A dynamic large eddy simulation of a streamwise periodic porous structure for three different Reynolds numbers ranging from 1200 to 4500 was performed. The flow field within the porous structure was turbulent and the level of turbulence was characterized by calculating the turbulent kinetic energy. The results of the simulations compare well to experiments performed downstream of a plastic model consisting of 8 periodic domains in series. The scalar transport of a tracer in the designed porous media was found to be clearly increased compared to commercial metal foams. The good mixing efficiency of the designed media can be attributed to the enhanced turbulence induced by the structure and the observed flow lamination effect. The turbulent kinetic energy measured downstream of the structure manufactured by stereolithography is strongly increased compared to the values found for the commercial metal foams. A fast decrease of this value was observed with increasing distance downstream of the porous media which is consistent with the experimental results for commercial metal foams presented in the previous chapter. The numerical results for the turbulent kinetic energy downstream of the porous media is in good agreement with the measure-

ments. For the investigated geometries with comparable porosity and pore size a change of the ligament shape from sharp edges to rounded edges results in a decrease of the turbulent kinetic energy and the pressure drop of about 30%. The ligament shape and thickness seems to be a key parameter in the scaling of a porous media for the use as a static mixing element. Therefore we conclude that there exists an optimum for the pore size and the size and the shape of the ligaments in terms of favorable pressure drop and induced turbulent kinetic energy. Furthermore the numerical results support the investigation of Hackeschmidt [61] with respect to the influence of the ligament shape, and the LES as a tool is able to provide more insight into the findings. The simulation revealed the interplay between the details of the geometry of the porous structures and the resulting hydrodynamic characteristics.

Chapter 8

Conclusions

In this thesis the heat and mass transfer properties of single-phase flow through highly porous media in the forced convection regime have been addressed. Different experimental methods were applied to study the axial and radial transport of a passive scalar and the convective heat transfer in commercially available foams of different pore sizes (20, 30 and 45 ppi) and a designed streamwise periodic structure at Reynolds numbers based on the empty tube ranging from 600 to 7600. This corresponds to volumetric flow rates ranging from $0.2 - 2.5\,\mathrm{l/min}$.

As a first step we assessed the mixing performance of the different porous media by means of PLIF and PIV measurements. The mean flow field is clearly distorted by the porous inserts. As a consequence the radial dispersion of a tracer dye, injected in front of the foam elements, is strongly increased. The homogenization is driven by combined flow lamination and turbulent transport processes. An increased induced turbulent kinetic energy was found with increasing ligament thickness. As a result the best mixing efficiency was estimated for the designed periodic structure. After a short mixing length of 50 mm values for the CoV below 0.05, corresponding to a nearly fully homogeneous radial distribution, were achieved. This is comparable to commercially available static mixing elements.

The longitudinal dispersion of a salty tracer dye was investigated by means of tracer pulse experiments. The narrow residence time distribu-

tions indicate a global plug flow behavior of the investigated structures ascribed to the turbulent flow within the cells. The estimated dispersion coefficients ranging from $1.3 \cdot 10^{-4}\,\mathrm{m^2/s}$ to $6.7 \cdot 10^{-3}\,\mathrm{m^2/s}$ were found to scale with the pore Reynolds number Re_p. In agreement to the radial mass transfer the axial dispersion of the the 20 ppi foam is increased compared to the 30 ppi foam, as expected while assuming an isotropic structure. The dispersion coefficients increase linearly with the Peclet number based on the pore size which is in agreement with literature data of packed beds and common packing materials.

The heat transfer was characterized by means of calorimetric measurements. The huge specific surface of metal foam and the turbulent flow lead to an increase in heat transfer which is up to 10 times higher compared to an empty tube case. In agreement to the mass transfer studies an increase of the convective heat transfer with increasing pore size, increasing ligament thickness respectively, is observed for commercially available metal foam of 20 and 30 ppi. The triangular ligament shape and the rough surface of the designed media accounts for an additional increase in heat transfer. By a fixed wall connection the performance of the device was found to be 30 % higher compared to the sintered structure without wall connection.

Finally the turbulent flow within the designed streamwise periodic porous structure was investigated by means of a dynamic large eddy simulation for three different Reynolds numbers ranging from 1200 to 4500. The numerical results for the turbulent kinetic energy downstream of the porous media compare well with experimental results. For the investigated geometries with comparable porosity and pore size a change of the ligament shape from sharp edges to rounded edges results in a decrease of the turbulent kinetic energy and the pressure drop of about 30%. The ligament shape and thickness were found to be the scaling parameters for porous media. We conclude that there exists an optimum for the pore size and the shape of the ligaments in terms of favorable pressure drop and induced turbulent kinetic energy. The LES provide an insight in the complex interplay between the details of the geometry of the porous structures and the resulting hydrodynamic characteristics.

The findings of this thesis show a high potential of continuous plug flow reactors by design. They provide the same surface area per volume of catalyst bed while generating a pressure drop over 10 times smaller

than corresponding particles. The associated high velocities lead to turbulent flow within the structure resulting in a strongly increased heat and mass transfer. The applied manufacturing process enables the optimization of the reactor geometry in terms of induced turbulence and specific surface depending on the application. By the fixed connection to the wall of the selective laser sintered device no restriction in heat transfer will be observed and no bypassing of the fluids flowing through the device occurs. Even hollow structures for optimized heat transfer are thinkable without loosing stability of the system. SLS is found to be a new tool for PI to further develop continuous processing in the chemical and pharmaceutical industry.

Chapter 9

Outlook

Based on the presented results and the conclusions, this chapter outlines further investigations on the topic. The outlook is divided in three parts. Within an experimental section future studies on single and multiphase flow through highly porous media will be presented. For example we suggest within a SNF proposal to conduct fundamental investigations on scalar transport within simplified grid structured elements to develop the basic understanding of the flow dynamics in porous media. First single phase flow experiments will be conducted, followed by the increase of the complexity of the flow situation to end up with multiphase flow through foam like structures. In parallel a multi electrode device will be developed further to characterize also gas-liquid flows. The experimental section is followed by the introduction of future numerical investigations on heat and mass transfer by applying new modeling approaches. Within the last section the investigation of the chemical performance of the device as a consequential further step and related projects are shown. A CTI (Comission of technology and innovation, BBT, Bern) proposal covers the chemical characterization by means of a hydrogenation reaction.

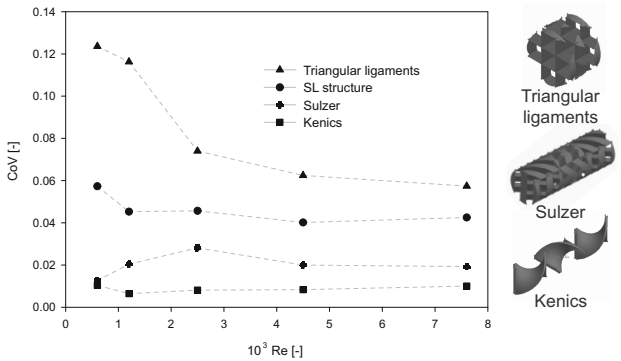

Figure 9.1: Comparison of mixing efficiency of the designed structure manufactured by SL with a reference geometry and two standard static mixing elements.

9.1 Experimental flow studies

9.1.1 Single-phase flow

Radial and axial dispersion

In order to compare the radial mixing performance of the designed structure to commercially available static mixers three additional geometries were manufactured from a transparent material by stereo lithography based on commercially available mixing elements. LIF experiments similar to the ones described in section 6.2 were performed downstream those geometries, all with a length of about 50 mm. The scattering of the data series depicted in Figure 9.1 can be ascribed to the small intensity differences to be resolved due to the very homogeneous concentration distributions and the geometric arrangement of the capillary with side injection. As expected the results show a clearly decreased CoV for the commercially available static mixing elements. Mainly the Kenics mixing unit performs well over the whole range of investigated Reynolds numbers. With a CoV below 0.01 the flow is completely homogenized.

Also the Sulzer packing performs very well with all measurements below 0.03. The reference geometry persisting of displaced grids with triangular ligaments delivers worse results then the designed foam. In general the designed structure, originally developed for the purpose of combined simulation and experiment, reaches the mixing performance of the commercially available static mixers much better then expected. With its huge specific surface it has a big advantage compared to all other geometries investigated, in terms of heat transfer and as catalyst support. Nevertheless an optimization is still possible as shown by these results.

To test the functionality of the WMS, described in section 4.5, it was installed to the presented setup to characterize the radial dispersion of a tracer. In comparison to the LIF results the WMS delivers decreased values for the CoV due to the decreased resolution, which leads to an averaging of structures, smaller then the sampling volume. Although the radial resolution is limited, enabling only qualitative in-situ measurement of the radial dispersion, it is a major advantage compared to commercial electrodes. It enables local instead of volumetric information about the fluid resistance with a high temporal resolution. The device discloses e.g. the possibility to measure the RTD of the liquid phase in a gas-liquid flow, which is very difficult with standard electrodes, due to the noise caused by the gas flowing through the device. The intrusive nature of the sensor is in our case negligible compared to the disturbance of the flow field by the porous media. Its very short axial fitting length allows to measure quasi inside the structure.

In a first step we applied the sensor for tracer pulse experiments in a single phase flow, similar the ones described in section 3.2.3. The test section was a sintered reactor with a length of 200 mm made of stainless steel. At the inlet and outlet a WMS was installed, as depicted in Figure 9.2. In order to avoid the effect of the entrance length, described in section 6.3, we additionally placed in front of the first sensor a sintered reactor of 200 mm length. The assumption that the flow is fully developed after this length is based on the results of the LES. In Figure 9.2 the results are compared to the measurements with standard electrodes. The estimated dispersion coefficients show a clear trend and increase monotone with the pore Reynolds number. They are higher than the results made for the short tube assembly and compare very well with the results made for the long tube assembly with commercial

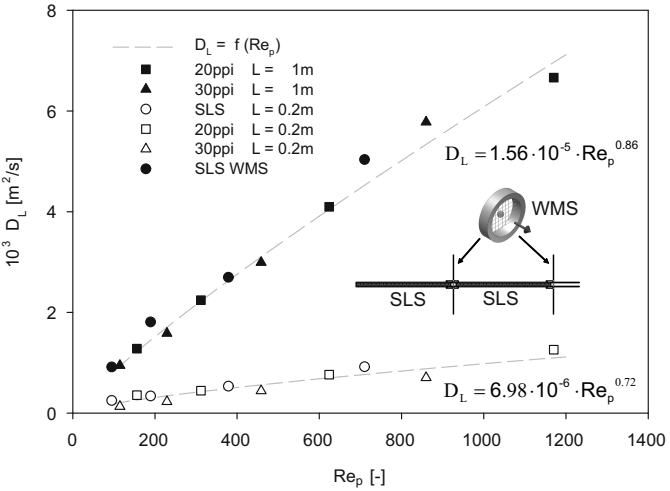

Figure 9.2: Comparison of dispersion measurements estimated by WMS and standard electrode devices.

metal foam (length of 1 m). This shows that the the assumption of a short entrance length is correct and that the dispersion coefficient of the designed porous media scales with the pore size, similar to commercially available metal foam. In this measurement series the WMS was found to be a good alternative in-situ measurement device with an extremely high temporal resolution of 10 kHz. The developed measurement procedure can also be applied to multiphase flow described in section 9.1.2.

Flow characterization in grid structured elements

The complexity and the small scales of the designed geometry, which fulfilled the specifications of this study, made inside optical measurements difficult. But based on the experiments on momentum and mass transfer downstream the porous media and numerical simulations within the structure we found that the ligaments have a huge influence on the flow behavior. Therefore we propose in the following to investigate the velocity field and the scalar concentration field in simple grid-structured

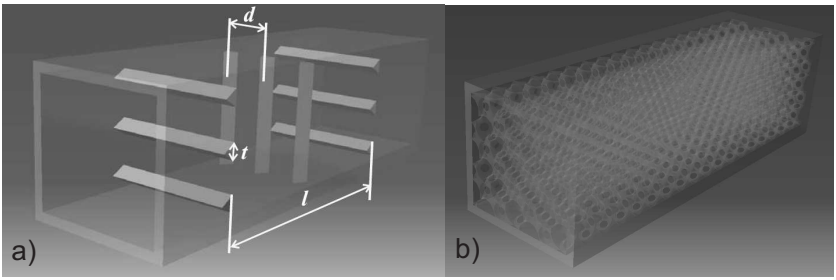

Figure 9.3: Sketch of the different mixing elements proposed for a fundamental study on the flow around ligaments in highly porous media.

mixing elements and then to slightly increase the complexity of the system. These first mixing elements will be streamwise periodic and will consist of several grid planes separated by a specific distance l (see Figure 9.3 a). They will be inserted in a rectangular channel in a way that PIV measurements between the different planes and behind the whole mixing element are possible. We will vary the distance d in between the ligaments, the ligament thickness t and the distance between the individual grid planes l to assess their influence on the induced level of turbulence intensity and turbulent kinetic energy. Furthermore we will be able to describe the spatial distribution of the Reynolds stresses and their relationship to the geometry. In addition, we will also investigate the concentration field of a scalar injected in front of the mixing element by applying LIF. The transport processes and the mixing processes will be evaluated by simultaneously measuring the velocity and concentration fields through a combination of PIV and LIF.

Index matching method

An increase of the complexity of the mixing elements towards foam-like structures (Figure 9.3b) requires the introduction of a new experimental technique. Index-matching will be used to enable measurements inside the complex porous media as the flow is no longer accessible from two orthogonal views. The investigated geometry will be manufactured from WaterShed XC 11122, a transparent material which can be used for stere-

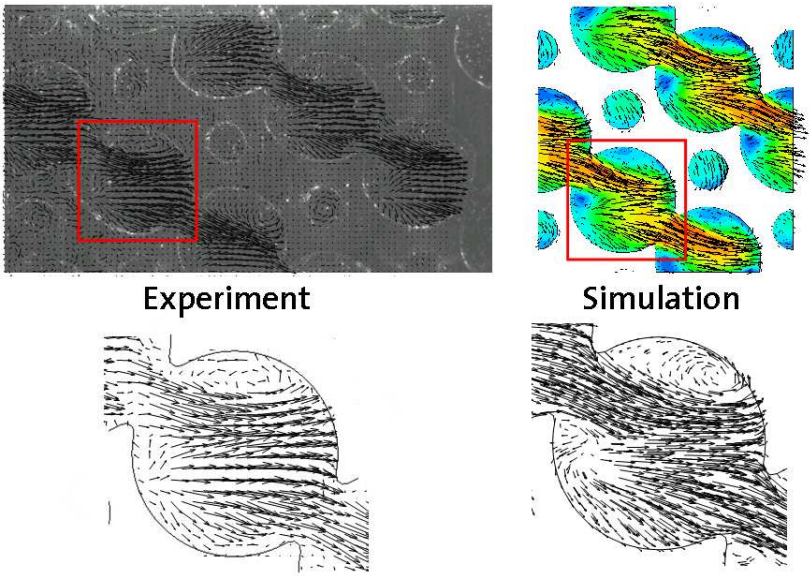

Figure 9.4: A velocity field measured within the porous structure by means of index matching method in comparison to LES results.

olithography. With this method a three-dimensional object of nearly any shape can be manufactured as described in section 2.2.2. The index of refraction of the transparent material is in the range of 1.512 - 1.515, which is higher than the one of water (1.33). Three different approaches were investigated in preliminary tests for the use as indexed matched fluids. As for the water-potassium iodide-glycerine system one come across the saturation of KJ, Natrium-iodide with water was used. Preliminary measurements however showed that precipitated iodine leads to a coloring of the transparent material. The index of refraction could also be matched by a mixture of the two oils turpentine and tetraline, which also enables Reynolds analogous experiments. A linear correlation was found between the volume fraction of turpentine and the refractive index. A major disadvantage of this mixture is the high viscosity and the associ-

ated high pumping power needed to convey the fluid. The best solution to match the index was found with the liquid anisole. In its pure state it has a refractive index of 1.517 meaning that no additional fluid has to be added. With a dynamic viscosity of 0.992 mPas and a density of 988.9 kg/m^3 it is in addition nearly identical to water in its hydrodynamic properties. Unfortunately the solvent is flammable and corrodes the plastic model slowly, which is a major drawback of all solvents. Using a lacquer to protect the plastic material is a possible solution, which was offered by the supplier. Although the lacquer delivers no ultimate protection against corrosion, we were able to apply the PIV technique to measure the velocity field inside the porous structure. A preliminary sample flow field in comparison to the LES is presented in Figure 9.4. A very good agreement can be seen by comparing those results. The LES represents the mean flow field within the structure with a high accuracy. In addition to further PIV studies investigating the entrance length in the porous media and the onset of turbulence, we will also assess the concentration field of a scalar injected in front of the mixing element by applying LIF. The scalar transport processes will be evaluated by simultaneously measuring the velocity and concentration fields through a combination of PIV and LIF.

9.1.2 Two-phase flow

Liquid-Liquid: Momentum and mass transfer

Based on the single phase flow investigations and the identified impact of the geometric parameters of the mixing elements on scalar transport, a static mixing element will be manufactured and its applicability to two-phase flow will be assessed. As the two liquids the use of either water and oil, or water and a water-sucrose mixture is intended. The water-sucrose dissolution has the advantage that the density and viscosity difference can be adjusted by the amount of added sugar. For applications in multiphase flows the simultaneous measurement of the velocity of each phase is of interest. Therefore we aim at transferring the PIV and LIF techniques to the liquid-liquid two-phase system. In a liquid-liquid system velocity measurements are achieved by applying PIV with two cameras simultaneously. The first phase is seeded with

regular seeding particles scattering the laser light with $\lambda_{scat} = 532nm$, the second phase with Rhodamine B coated particles scattering emitted light with $\lambda_{scat} = 580nm$. By applying filters to each camera the signals can be separated from each other and the cross-correlation yields the individual velocity of each phase. This information is combined for the whole field of view in the post-processing by using an appropriate mapping function. In addition the interfacial mass transfer can be investigated by using LIF with one phase including a tracer dye and the second phase without it. Thus we will be able to fully address the mixing processes in two-phase flows using static mixing elements. We are aware that we will not be able to apply the whole-field measurement techniques to measurements inside the porous structure, since the index-matching technique will not work for two-phase flow. Therefore we propose to measure the velocity and scalar fields of the individual phases in a cross-section behind a mixing element or in an optically accessible domain within a simplified element. Furthermore, we intend to apply point-measurement techniques like LDA to characterize the two-phase flow in a cross-section within a complex structure, similar to the study of Hall and Hiatt [62] who investigated single-phase flow.

Gas-liquid: Holdup, radial dispersion and RTD

Gas-liquid flow through the designed streamwise periodic media made by stereolithography was characterized by measuring the transient void fraction at the in- and outlet of the structure. Therefore the WMS technology described in detail in section 4.5 was applied. The sensor concept allows to perform in situ measurement of multiphase flow with a high temporal resolution of 10 kHz. Preliminary results are promising and will be presented in the following.

In order to investigate a well defined gas-liquid flow, the gas flow rate was kept constant at a value of 100 Nml/min, corresponding to the volumetric gas flow rate at the outlet of the test section with a length of 50 mm. The liquid flow rate was varied from 500 to 2500 ml/min. The highly dispersed gas phase, observed for all investigated flow configurations, is favorable for the later application of the reactor, namely gas liquid reactions. For every flow configuration snapshots were taken with a CCD camera to compare the results of the WMS with an optical

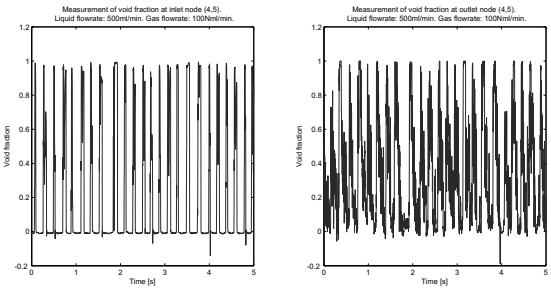

Figure 9.5: Inlet and outlet signal at a single node (4,5) for a liquid flow rate of 500 ml/min and a gas flow rate of 100 Nml/min

method. In Figure 9.5 the void fraction recorded at a single node (4,5) corresponding to Figure 4.14 is depicted for the WMS upstream and downstream the reactor for the smallest liquid flow rate of 500 ml/min. At the inlet a plug flow is observed leading to a signal with clearly separated peaks indicating the air bubbles flowing through the device. For the temporal mean void fraction the average value of the curve can be calculated. The small peaks running below the 0 level after each bubble are ascribed to water bridges forming in between the wires, but the effect is still not fully discussed. The influence on the mean void fraction is however insignificant. Downstream the reactor a clear decrease of the bubble size can be seen. This is first described by the strongly decreased time scale of the single peaks and the increase in the number of peaks. The second indication for smaller air bubbles is that not all peaks reach a void fraction of 1 meaning that their characteristic size is typically smaller than the control volume. Given that the velocity of the air bubbles is not known, a quantitative description of the bubble size distribution is not possible and only qualitative statements are allowed. Nevertheless the quantitative measurement of the mean temporal void fraction could be shown by Prasser et al. [122], who found a systematic error of 8% for his device ascribed to the deformation of the wires during operation.

For the highest liquid volume flow rate of 2500 ml/min the signals at the same location (node (4,5)) are depicted in Figure 9.6. Still the bub-

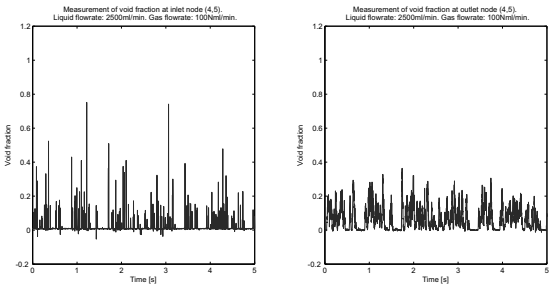

Figure 9.6: Inlet and outlet signal at a single node (4,5) for a liquid flow rate of 2500 ml/min and a gas flow rate of 100 Nml/min

bles can clearly be separated from each other. A pulsation of the flow is observed and swarms of bubbles flow in invariant time steps through the sensor upstream. Those gas accumulations are also recorded by the second sensor downstream. They are slightly broadened but still clearly separated. The short mixing zone of about 50 mm is to small for a complete axial homogenization of the flow. Nevertheless a strong decrease of the bubble size within the investigated structure can be observed resulting in a decreased absolute void fraction. By considering the temporal mean void fraction distribution over the cross section of the two velocities, depicted in Figure 9.8, a huge change in the flow behavior can be seen. In case of the small liquid velocity of 500 ml/min at the inlet of the test section the huge bubbles flowing with a certain regularity through the device. Hence the bubbles are clearly seen at the upper wall of the tube in the mean temporal void fraction distribution, which is lower than 0.5, due to the liquid holdup of the flow. Downstream of the reactor the gas is more dispersed in the liquid phase but the effect of gravity is still observed. The gas phase is more present in the upper part of the tube which can be seen in a locally increased void fraction. The higher mean void fraction of the cross section downstream compared to upstream is explained by the pressure drop over the test section and the therefore increasing gas volume. For the higher liquid flow rate of 500 ml/min again the elevated static pressure in front of the foam and the higher liquid flow rate entail an increase of the void fraction over the whole cross section

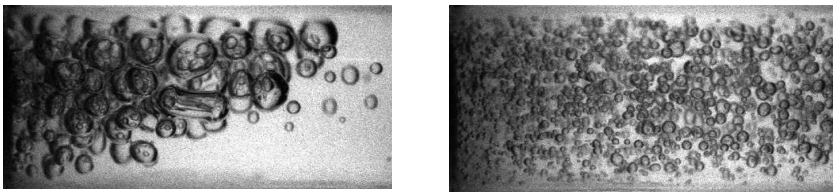

Figure 9.7: Snapshot of the multi-phase flow with a gas flow rate of 100 ml/min and a liquid flow rate of 500 ml/min (left) und 2500 ml/min (right).

of the pipe. But still huge bubbles seem to enter the test section along the upper wall. Downstream the reactor a highly dispersed gas phase is determined in terms of a very homogeneous void fraction distribution. The effect of the gravitational force is of minor importance which is also observed in the snapshots of the flow field at the outlet of the test section depicted in Figure 9.7. Interesting is also the fast coagulation downstream of the foam elements depending on the fluid velocity. This indicates the huge impact of the porous structure on the flow behavior and the good ability of radial mixing of the system like already observed for single phase flow. This impression is clarified by the consideration of the side plots demonstrated in Figure 9.8. These images are generated by simply plotting the signal of a single receiver line versus time. This results in a side view of the tube which has to be treated carefully as the gas phase possess a different velocity as the liquid phase. This slip leads to a distortion of the bubble as only the measurement frequency but not the displacement of the bubble during this time step is known. The plots are therefore only of qualitative manner. Nevertheless the illustration is very helpful to demonstrate the effectiveness of the reactor. The plugs entering the system leave it dispersed in the liquid phase. Ones again one can see that the effect of gravitation nearly disappear at the highest flow rate investigated.

By examining the mean temporal and spatial void fraction versus the volumetric transport fraction of the gas phase a linear increase is observed downstream the test section as illustrated in Figure 9.9. The increased volumetric flow rate downstream, due to the decreased pressure,

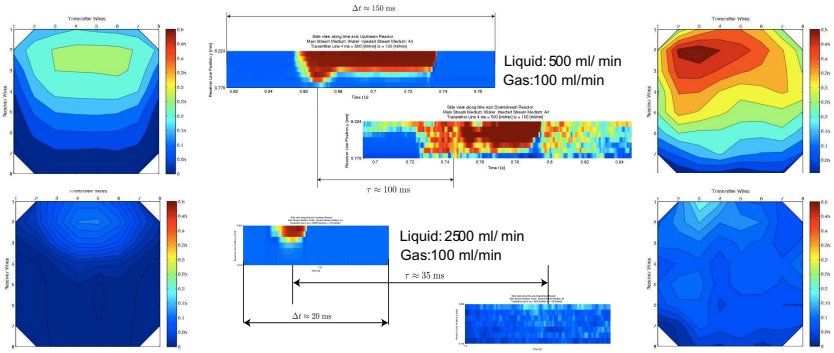

Figure 9.8: Time series for two different liquid velocities depicted as a side view from the center of the tube (center column) with the corresponding mean temporal void fraction distributions at the inlet (left column) and the outlet (right column).

leads to an increased mean void fraction compared to the measurements upstream. Those data don't exhibit a linear increase with the volumetric flow rate. This is due to the description of the data by the volumetric transport fraction, which is only valid downstream of the reactor, where an ambient pressure is assumed. The non-linear increase of the pressure drop with the applied liquid velocity entails a non-linear increase of the void fraction with increasing volumetric transport fraction in front of the test section. The data set is to small for a detailed analysis but a rough estimation of the error of the device can be done as follows. By fitting the results downstream the reactor with a linear regression, a positive displacement of the straight line with respect to the coordinate origin indicates a positive error of the void fraction measured. The deviation is very small and corresponds to an absolute value of 0.02 indicating that the device works very properly.

From the void fraction the slip of the gas phase can be calculated according to equation 3.61. This is only valid downstream the test section as the pressure upstream was not measured during operation and therefore the volumetric flow rate upstream is unknown. Nevertheless the

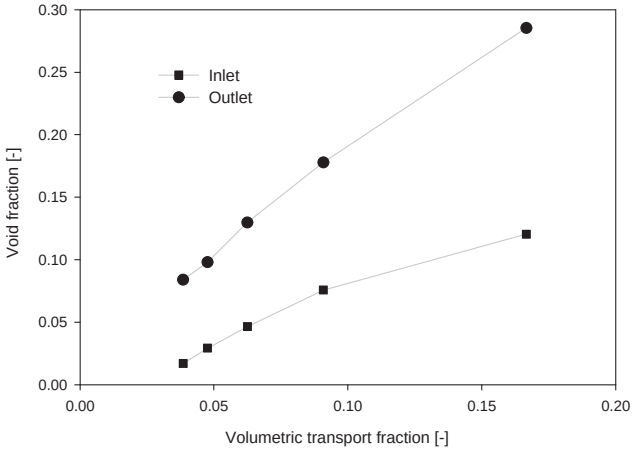

Figure 9.9: Void fraction versus volumetric transport fraction at the inlet and outlet of the test section

absolute value of the slip was nearly constant at about 0.5. This leads to the assumption of a permanent decrease of the air bubble size with increasing liquid flow rate, which was also observed in the snapshots of the different experiments.

Another interesting application of the WMS is the characterization of the axial dispersion in multiphase flows. The idea in case of the investigated gas-liquid flow is to measure the residence time of the liquid phase, which is important for the characterization of a chemical reaction performed. A measurement of the residence time by means of the standard electrodes, like applied for the single phase system, failed due to the highly distorted signal caused by the gas bubbles. This made a convolution of the in- and outlet concentration impossible. In contrast the WMS delivers information over the whole cross section, instead of volumetric information. For the preliminary experiments performed, all spatially resolved signals were simply averaged with the assumption of a homogeneous mixture at the inlet and outlet of the tube. By this a

very smooth concentration signal was achieved enabling to resolve very small time scales. As a next step also other pretreatment of the data, e.g. baseline tracking, will be implemented to further improve the measurement device allowing simultaneous gas fraction and concentration measurements.

9.1.3 Suspensions and high viscous flows

A big motivation for the up-scaling of micro reactors is given by the difficulties in handling particle laden or high viscous flows. Small scale reactors tend to clog after a short time of operation due to the small scales and the predominantly laminar flow. The reactor by design developed within this study offers the big advantage of an individually designed structure. Parameters like porosity, specific surface and geometric length scales can be adjusted to the particular requirements and they are fully scalable in all three dimensions. Simulations can be applied to design a basic geometry and the fast manufacturing enable a fast process optimization by means of experiments. Problems appearing during operation can be taken into account in the following reactor generation. Thereby also the assembly of new geometries on top of existing parts is possible.

9.2 Numerical flow studies

9.2.1 Large eddy simulation

Simulation in x-ray scan

In order to compare experimental and numerical results, the original CAD model of the designed structure was adapted according to an x-ray scan (section 6.1.2) to take the tolerance of the manufacturing method into account. A good agreement of the simulation within this revised geometry and the experiment could be achieved. From a scientific point of view it is also of interest to fully understand the influence of the surface roughness, which was made responsible for the deviations in pressure drop and the turbulent kinetic energy comparing the simulation and the experiment. One possibility to study this is the detailed implementation

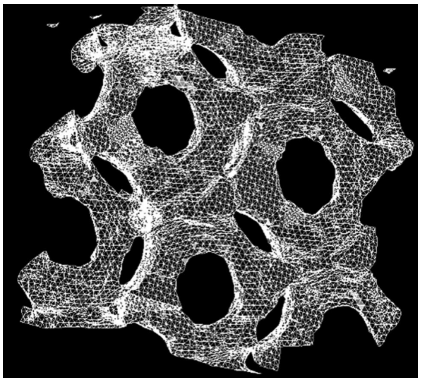

Figure 9.10: Surface mesh of the solid material of the stereo lithographically manufactured polymer model calculated from an x-ray scan.

of the x-ray scan to the computational fluid dynamic software. Despite the difficulties, e.g. threshold detection for the raw images and near wall mesh generation, a fluid domain could be compiled. An illustration of a test mesh is depicted in Figure 9.10. The challenge of a real domain is the implementation of periodic boundary conditions since the inlet cross section will differ slightly from the outlet. To overcome this problem a new method to treat pseudo convective boundary conditions will be developed and implemented in the fluid dynamic software by means of user defined functions.

Investigation of heat transfer mechanism

In literature a lot of different studies dealt with the numerical estimation of heat transfer in solid foam structures. In analogy to the flow through porous media the detailed reconstruction of the geometry for modeling purpose is a bottleneck for the basic understanding of the heat and mass transfer mechanisms. The authors dealing with this topic are constrained to work with macroscopic models or simplified geometries. An overview of different modeling approaches used to estimate pressure drop and heat transfer in solid foams is presented from Mahjoob and Vafai [97]

who characterized the pertinent correlations in three main topics.

- Correlations for pressure drop and heat transfer coefficient based on the microstructural properties of the metal foam
- Correlations specialized for metal foam tube heat exchangers
- Correlations specialized for metal foam channel heat exchangers

Underneath the simple model of cubic cells for open foams is presented which was e.g. also used by Lu et al. [94] or Ghosh [56]. Thereby the foam is assumed as a structure of cylinders crossing each other in an angle of 90 degrees. Also two-dimensional approaches are shown like the one of Dukhan et al. [38] which applied simplified equations from the literature and adapted those to the problem. All of these macroscopic modeling approaches imply strongly simplified boundary conditions like constant heat flux or constant wall temperature. Hence limitations of the heat transfer like local overheating of the solid foam or the connection of the foam with the surrounding wall cannot be estimated. It is of interest to expand our LES by solving the conservation of energy equation for the fluid domain and the adjacent solid foam. Therefore an x-ray scan of the sintered reactor made of stainless steel is already available. The numerical results could be evaluated by the experiments presented in this study.

9.2.2 k-ε model for wall adjacent flow

To perform numerical experiments by means of LES is very expensive in terms of computational costs. But to study the fluid dynamics within the porous media it is still a fast tool compared to direct numerical simulation (DNS). A solution to further reduce computational cost is given by using Reynolds averaged Navier-Stokes equations (RANS). A disadvantage of such modeling approaches is the “missing” transient information which is of interest while studying time dependent phenomena like e.g. entrance lengths. In addition such models are mainly developed to handle isotropic turbulence and they run into problems at strongly

wall adjacent flows. The most common RANS model, the standard k-ε, is known to fail when estimating the level of turbulent kinetic energy around a stagnation point. The reason is found in the modeled production rate of k where the second derivative of the velocity attains a quite large value for the decelerating flow in front of an obstacle leading to an overestimated value. This effect is comprehensively presented in Kuwahara et al. [89] who compared numerical results of a k-ε model with the ones of a LES. The designed structure is in this point of view a worst case scenario for the application of the standard k-ε model. In front of every ligament the flow is strongly decelerating. In order to overcome this difficulties an adapted k-ε approach will be applied to our problem based on the study of Hanjalic and Kenjeres [65]. We will compare the results to our experimental work and the LES.

9.2.3 Macroscopic k-ε approach - a fast scaling tool

To study basic phenomena within the porous structure macroscopic models cannot be applied as mentioned above. Nevertheless those models are very interesting, ones the basic mechanisms of heat and mass transfer are understood, because of the strongly decreased computational costs. They allow fast parameter studies and that's why a fast scaling of the reactor for a given purpose. For this reason we develop together with the laboratory of thermodynamics in emerging technologies a macroscopic k-ε model based on the numerical results from the LES. The basic idea is to describe the source term of the turbulent kinetic energy and the energy dissipation rate with a correlation, estimated from the available numerical results of the LES. The model will then be validated by simulating the transport of a passive scalar through the designed porous media and comparing the results to the experimental data of this study.

9.3 Reactive flows

Heterogeneous catalyzed gas flows through solid foams were widely studied in literature (e.g. Giani et al. [57, 59], Pestryakov et al. [112], Richardson et al. [128]). Those investigations are dealing with catalytic combustion, selective catalytic reduction (SCR-DeNOx), and

automotive exhaust gas after treatment. In Ferrouillat et al. [47] the investigation of a liquid reaction system is conducted in order to characterize the mixromixing efficiency in solid foams. They proposed to use the parallel-competing Villermaux reactions (iodide-iodate test) ,developed by Fournier et al. [52]. Investigations on multiphase reactions through solid foam were only performed by Stemmet [141] investigating the hydrodynamics and mass transfer in packed columns.

9.3.1 Single-phase flow: Micro mixing

For chemical reaction processes it is of interest to understand the mass transfer mechanisms in detail. Although the simultaneous measurement of the mixing progress at the macro- and the microscale is to aspire. This can be enabled by e.g. two color laser induced fluorescence technique. A mixture of an inert and a reacting fluorescent dye is injected into the reactor. The dyes are required to be excitable at the same wavelength and the emission characteristics must be distinguishable (Kling and Mewes [80]). The inert dye is the tracer for the macro mixing in analogy to the LIF experiments performed within this work. An indirect visualization of the micro mixing is given by the reactive dye since the chemical reaction requires mixing on the molecular scale.

9.3.2 Two-phase flow: Hydrogenation in SLS reactor

The developed reactor approach was mainly characterized during this work with a single phase flow due to the well defined conditions. But in the final application proposed by our industrial partner one has certainly to deal with multi-phase flow. A huge potential is seen for heterogeneous catalyzed gas liquid reactions. The designed structures offers a porosity of about 80% and a specific surface comparable to a fixed beds. The idea to coat an immobilized catalyst on its surface is therefore obvious. The very good mixing behavior, the good dispersion of a gas in a liquid phase and the metallic catalyst support enables to run an exothermic reaction at quasi isothermal conditions in a continuous way. For the industrial partner mainly hydrogenations are of superficial interest as they are very common in the vitamin synthesis. For further investigations of

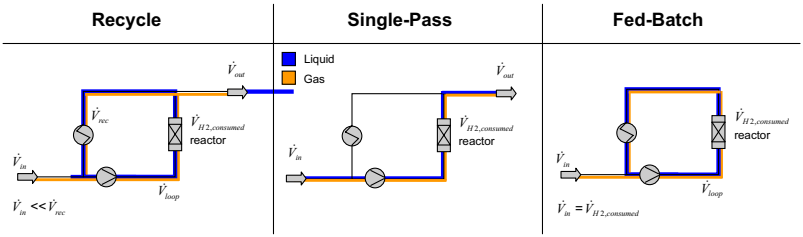

Figure 9.11: Simplified scheme of the laboratory plant at the site of DSM Nutritional Products showing the different modes of operation.

this purpose a laboratory scale loop reactor was installed at the cite of the industrial partner. A simplified scheme of the facility is depicted in Figure 9.11. The reactor itself has a length of 200 mm and it is fully sintered. The facility can be operated in three different operation modes to screen the catalyst performance. The major objective in doing so is to clearly enhance the selectivity compared to the conventional batch process as the reaction investigated leads to an over hydrogenation to an unintentional product. The first results acquired within a Master thesis show that the Palladium catalyst could be successfully coated on top of the designed stainless steel surface and a high selectivity could be observed but not yet under the final reaction conditions. Further investigation and optimization of the process will be performed within a follow up project sponsored by the innovation promotion agency CTI and DSM Nutritional Products®.

9.3.3 Plasma assisted Pd coating

As oxide catalyst support possess poor heat conductivity, supports of metal would suit better to highly exothermic reactions. Nevertheless, common techniques to precipitate and attach catalytic particles to a metal are accompanied by several disadvantages. Wash-coating (Giani et al. [57]) and sol-gel (Breitscheidel et al. [28]) techniques embed the catalytic particles into to non-metallic matrices. As a result, the catalytic

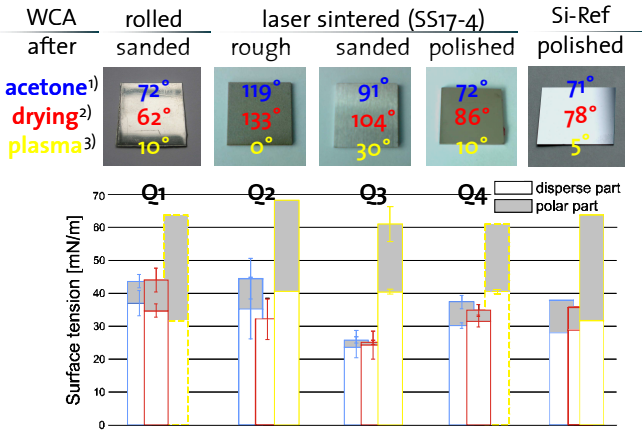

Figure 9.12: Disperse (white) and polar (grey) surface tension of the coarse cleaned, annealed and plasma treated samples.

particle active sites are largely reduced. Furthermore, wet-impregnation (Navio et al. [104]) typically leads to a broad size distribution of the catalytic particles. Lately, Wyrwa and Schmid [163] have overcome these disadvantages by attaching pre-prepared catalyst particles in plasma. However in view of the complexity of pre-preparation and handling of nanoparticles, a simple wet-impregnation is most appealing. Therefore, senior assistant Dr. A. Sonnenfeld of our laboratory came up with the idea to perform a study on the plasma activation of stainless steel prior wet-impregnation for the synthesis and the attachment of Pd nanoparticles. Some preliminary results of this collaboration will be presented in the following.

Plasma treatment

Fine cleaning and activation of polished stainless steel samples (9.14) and three other stainless steel qualities are obtained by means of capacitive RF discharge in a vacuum reaction vessel at a pressure of 4 Pa. The Plasma facility is described in detail in Sonnenfeld et al. [138]. O_2 or Ar (20 sccm) are feed to the plasma. Together with Si wafers, 4 steel samples

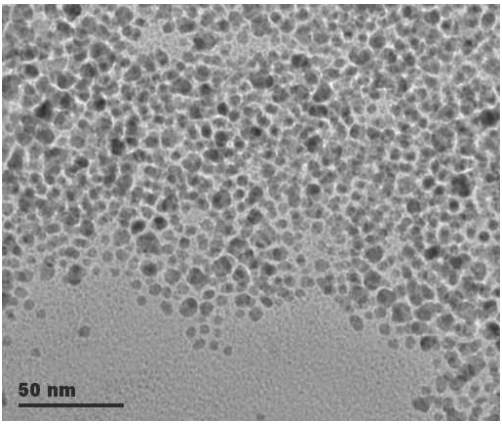

Figure 9.13: Transmission electron micrograph of an extract of the colloidal dispersion of Pd particles synthesized in the wet-impregnation solution.

of different surface quality were exposed to the plasma for 15 s to 5 min (plasma powers: 50 W to 450 W). Prior the plasma treatment, coarse cleaning in an acetone ultrasonic bath for 5 min was applied to remove lubricants. Figure 9.12 depicts preliminary contact angle measurements (according to Owens and Wendt [106]) on smooth silicon wafer samples and the 4 different stainless steel qualities. In all cases the effect of the Plasma treatment is clearly seen. The strong increase of the polar part is ascribed to the formation of hydroxyl groups on the sample surface leading to a good wettability. In case of the sintered device without pretreatment, which correspond to the final surface quality, the wettability was found to be best after plasma treatment. After every plasma treatment, the reaction vessel was vent applying an O_2 feed of 100 sccm for 30 min. The reactor was then vent by Ar to reach ambient pressure.

Wet-impregnation

Immediately after plasma treatment, simultaneous impregnation and decomposition of the precursor $Pd_2(dba)_3$ (dissolved in THF containing the

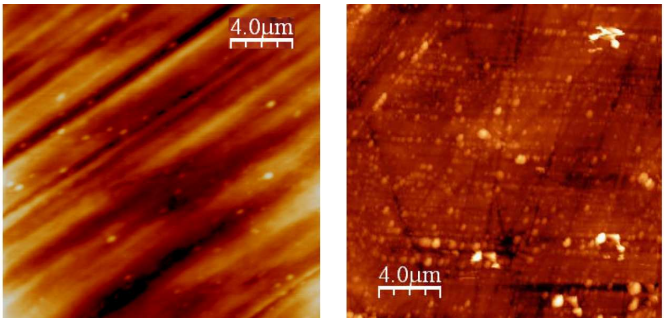

Figure 9.14: Atomic force micro graph of (a) the coarse cleaned stainless steel surface and (b) the coarse cleaned reference samples after wet-impregnation functionalization.

stabilizing ligand (hexadecylamine, HDA) and pressurized by 3 bar of H_2 for 20 h) was performed. Transmission-electron micrographs of the impregnation solution reveal a size distribution of 6 to 10 nm of the Pd nanoparticles (Figure 9.13). AFM in tapping mode reveals the presence of nanoparticles attached to the steel surfaces at a characteristic size comparable to those observed in colloidal dispersion. Thus their surface adhesion is facilitated and coagulation at the surface is hindered due to the plasma pre-treatment. In order to evaluate the influence of the plasma pre-treatments, all samples impregnated were compared to a reference sample which was coarse cleaned only (see Figure 9.14 a). Complementary, the effect of plasma treatment was monitored by surface tension measurements on the plasma treated samples prior the impregnation.

Bibliography

[1] Adrian, R. J. [1991]. Particle-imaging techniques for experimental fluid-mechanics, *Annual Review of Fluid Mechanics* **23**: 261–304.

[2] Agliozzo, S. and Cloetens, P. [2004]. Quantification of micrometre-sized porosity in quasicrystals using coherent synchrotron radiation imaging, *Journal of Microscopy-Oxford* **216**: 62–69.

[3] Andrews, J. R. [2004]. Deconvolution of system impulse responses and time domain waveforms, *Application Note AN-16a (www.picosecond.com)* .

[4] Annapragada, S. R., Murthy, J. Y. and Garimella, S. V. [2008]. Permeability and thermal transport in compressed open-celled foams, *Numerical Heat Transfer Part B-Fundamentals* **54**(1): 1–22.

[5] Anxionnaz, Z., Cabassud, M., Gourdon, C. and Tochon, R. [2008]. Heat exchanger/reactors (hex reactors): Concepts, technologies: State-of-the-art, *Chemical Engineering and Processing* **47**(12): 2029–2050.

[6] Ashby, M. F., Evans, A., Fleck, N. A., Gibson, L. J., Hutchinson, J. W. and Wadley, H. N. G. [2000]. *Metal Foams A Design Guide*, Elsevier Inc.

[7] Ashby, M. F. and Lu, T. J. [2003]. Metal foams: A survey, *Science in China Series B-Chemistry* **46**(6): 521–532.

[8] Azzi, W., Roberts, W. L. and Rabiei, A. [2007]. A study on pressure drop and heat transfer in open cell metal foams for jet engine applications, *Materials and Design* **28**(2): 569–574.

[9] Baker, O. [1954]. Simultaneous flow of oil and gas, *Oil Gas Journal* **53**: 184–195.

[10] Baldyga, J. and Bourne, J. R. [1999]. *Turbulent mixing and chemical reaction*, John Wiley and Sons Ltd., Chichester.

[11] Banhart, J. [2001]. Manufacture, characterisation and application of cellular metals and metal foams, *Progress in Materials Science* **46**(6): 559–U3.

[12] Banhart, J. [2005]. Aluminium foams for lighter vehicles, *International Journal of Vehicle Design* **37**(2-3): 114–125.

[13] Batchelor, G. K. [1959]. Small-scale variation of convected quantities like temperature in turbulent fluid .1. general discussion and the case of small conductivity, *Journal of Fluid Mechanics* **5**(1): 113–133.

[14] Baumgartner, F., Duarte, I. and Banhart, J. [2000]. Industrialization of powder compact foaming process, *Advanced Engineering Materials* **2**(4): 168–174.

[15] Bennia, A. and Nahman, N. S. [1990]. Deconvolution of causal pulse and transient data, *Ieee Transactions on Instrumentation and Measurement* **39**(6): 933–939.

[16] Bhattacharya, A., Calmidi, V. V. and Mahajan, R. L. [2002]. Thermophysical properties of high porosity metal foams, *International Journal of Heat and Mass Transfer* **45**(5): 1017–1031.

[17] Bhattacharya, A. and Mahajan, R. L. [2006]. Metal foam and finned metal foam heat sinks for electronics cooling in buoyancy-induced convection, *Journal of Electronic Packaging* **128**(3): 259–266.

[18] Bieberle, M., Fischer, F., Schleicher, E., Koch, D., Menz, H. J., Mayer, H. G. and Hampel, U. [2009]. Experimental two-phase flow measurement using ultra fast limited-angle-type electron beam x-ray computed tomography, *Experiments in Fluids* **47**(3): 369–378.

[19] Blevins, R. [1984]. *Applied fluid dynamic handbook*, Van Nostrand Reinhold Co, New York.

[20] Bockhorn, H., Mewes, D., Peukert, W. and Warnecke, H.-J. [2010]. *Micro and Macro Mixing*, Springer Verlag, Berlin Heidelberg.

[21] Bohnet, M. [2005]. Multiphase fluid flow, *Dubbel*, Vol. 21, Springer Verlag, Berlin Heidelberg, pp. 28–36.

[22] Bonnet, J. P., Topin, F. and Tadrist, L. [2008]. Experimental study of two-phase flows through open-celled metallic foams, *in* L. P. Lefebvre, J. Banhart and D. C. Dunand (eds), *Porous Metals and Metallic Foams: Metfoam 2007*, Destech Publications, Inc, Lancaster, pp. 467–470.

[23] Boomsma, K. and Poulikakos, D. [2001]. On the effective thermal conductivity of a three-dimensionally structured fluid-saturated metal foam, *International Journal of Heat and Mass Transfer* **44**(4): 827–836.

[24] Boomsma, K. and Poulikakos, D. [2002]. The effects of compression and pore size variations on the liquid flow characteristics in metal foams, *Transactions of the ASME. Journal of Fluids Engineering—Transactions of the ASME. Journal of Fluids Engineering* **124**(1): 263–72.

[25] Boomsma, K., Poulikakos, D. and Ventikos, Y. [2003]. Simulations of flow through open cell metal foams using an idealized periodic cell structure, *International Journal of Heat and Fluid Flow* **24**(6): 825–834.

[26] Boomsma, K., Poulikakos, D. and Zwick, F. [2003]. Metal foams as compact high performance heat exchangers, *Mechanics of Materials* **35**(12): 1161–1176.

[27] Boyer, C., Duquenne, A. M. and Wild, G. [2002]. Measuring techniques in gas-liquid and gas-liquid-solid reactors, *Chemical Engineering Science* **57**(16): 3185–3215.

[28] Breitscheidel, B., Zieder, J. and Schubert, U. [1991]. Metal-complexes in inorganic matrices .7. nanometer-sized, uniform metal particles in a sio2 matrix by sol-gel processing of metal-complexes, *Chemistry of Materials* **3**(3): 559–566.

[29] Calvo, S., Beugre, D., Crine, M., Leonard, A., Marchot, R. and Toye, D. [2009]. Phase distribution measurements in metallic foam packing using x-ray radiography and micro-tomography, *Chemical Engineering and Processing* **48**(5): 1030–1039.

[30] Carberry, J. J. and Bretton, R. H. [1958]. Axial dispersion of mass in flow through fixed beds, *Aiche Journal* **4**(3): 367–375.

[31] Charlaix, E., Hulin, J. P. and Plona, T. J. [1987]. Experimental-study of tracer dispersion in sintered glass porous materials of variable compaction, *Physics of Fluids* **30**(6): 1690–1698.

[32] Cooley, J. W. and Tukey, J. W. [1965]. An algorithm for machine calculation of complex fourier series, *Mathematics of Computation* **19**(90): 297–and.

[33] Corporation, E. M. and Aerospace [n.d.]. www.ergaerospace.com.

[34] Danckwerts, P. V. [1953]. Continuous flow systems - distribution of residence times, *Chemical Engineering Science* **2**(1): 1–13.

[35] Delgado, J. [2006]. A critical review of dispersion in packed beds, *Heat and Mass Transfer* **42**(4): 279–310.

[36] Dimopoulos Eggenschwiler, P., Tsinoglou, D., Seyfert, J., Bach, C., Vogt, U. and Gorbar, M. [2009]. Ceramic foam substrates for automotive catalyst applications: fluid mechanic analysis, *Experiments in Fluids* **47**(2): 209–222.

[37] Dukhan, N. [2006]. Correlations for the pressure drop for flow through metal foam, *Experiments in Fluids* **41**(4): 665–672.

[38] Dukhan, N., Picon-Feliciano, R. and Alvarez-Hernandez, A. R. [2006]. Heat transfer analysis in metal foams with low-conductivity fluids, *Journal of Heat Transfer-Transactions of the Asme* **128**(8): 784–792.

[39] Dupuit, J. [1863]. Etudes theoriques et pratiques sur le mouvement des eaux., *Dunod, Paris* .

[40] Ebach, E. A. and White, R. R. [1958]. Mixing of fluids flowing through beds of packed solids, *Aiche Journal* **4**(2): 161–169.

[41] Edouard, D., Huu, T. T., Huu, C. P., Luck, F. and Schweich, D. [2010]. The effective thermal properties of solid foam beds: Experimental and estimated temperature profiles, *International Journal of Heat and Mass Transfer* **53**(19-20): 3807–3816.

[42] Edouard, D., Ivanova, S., Lacroix, M., Vanhaecke, E., Pham, C. and Pham-Huu, C. [2009]. Pressure drop measurements and hydrodynamic model description of sic foam composites decorated with sic nanofiber, *Catalysis Today* **141**(3-4): 403–408.

[43] Edward, P. L. [2003]. *Handbook of industrial mixing: Science and Practice*, John Wiley and Sons, New Jersey.

[44] Elmoutaouakkil, A., Fuchs, G., Bergounhon, P., Peres, R. and Peyrin, F. [2003]. Three-dimensional quantitative analysis of polymer foams from synchrotron radiation x-ray microtomography, *Journal of Physics D-Applied Physics* **36**(10A): A37–A43.

[45] Ergun, S. and Orning, A. A. [1949]. Fluid flow through randomly packed columns and fluidized beds, *Industrial and Engineering Chemistry* **41**(6): 1179–1184.

[46] Fasano, J. B. [1991]. Kenics hev mixer sets a new standard for turbulent flow mixing efficiency., *Mixing XIII*, Banff, Canada.

[47] Ferrouillat, S., Tochon, P. and Peerhossaini, H. [2006]. Micromixing enhancement by turbulence: Application to multifunctional heat exchangers, *Chemical Engineering and Processing* **45**(8): 633–640.

[48] Flannery, B. P., Deckman, H. W., Roberge, W. G. and Damico, K. L. [1987]. 3-dimensional x-ray microtomography, *Science* **237**(4821): 1439–1444.

[49] Flin, F., Brzoska, J. B., Lesaffre, B., Cileou, C. and Pieritz, R. A. [2003]. Full three-dimensional modelling of curvature-dependent snow metamorphism: first results and comparison with experimental tomographic data, *Journal of Physics D-Applied Physics* **36**(10A): A49–A54.

[50] *FLUENT 6.3 User's Guide* [2006].

[51] Forchheimer, P. [1901]. Water movement through the ground, *Zeitschrift Des Vereines Deutscher Ingenieure* **45**: 1781–1788.

[52] Fournier, M. C., Falk, L. and Villermaux, J. [1996]. A new parallel competing reaction system for assessing micromixing efficiency - experimental approach, *Chemical Engineering Science* **51**(22): 5053–5064.

[53] Fukushima, S. and Kusaka, K. [1979]. Gas-liquid mass-transfer and hydrodynamic flow region in packed-columns with cocurrent upward flow, *Journal of Chemical Engineering of Japan* **12**(4): 296–301.

[54] Gerbaux, O., Vercueil, T., Memponteil, A. and Bador, B. [2009]. Experimental characterization of single and two-phase flow through nickel foams, *Chemical Engineering Science* **64**(19): 4186–4195.

[55] Germano, M., Piomelli, U., Moin, P. and Cabot, W. H. [1991]. A dynamic subgrid-scale eddy viscosity model, *Physics of Fluids a-Fluid Dynamics* **3**(7): 1760–1765.

[56] Ghosh, I. [2009]. How good is open-cell metal foam as heat transfer surface?, *Journal of Heat Transfer* **131**(10): 101004 (8 pp.)–101004 (8 pp.).

[57] Giani, L., Cristiani, C., Groppi, G. and Tronconi, E. [2006]. Washcoating method for pd/-gamma-al2o3 deposition on metallic foams, *Applied Catalysis B-Environmental* **62**(1-2): 121–131.

[58] Giani, L., Groppi, G. and Tronconi, E. [2005a]. Heat transfer characterization of metallic foams, *Industrial and Engineering Chemistry Research* **44**(24): 9078–9085.

[59] Giani, L., Groppi, G. and Tronconi, E. [2005b]. Mass-transfer characterization of metallic foams as supports for structured catalysts, *Industrial and Engineering Chemistry Research* **44**(14): 4993–5002.

[60] Habisreuther, P., Djordjevic, N. and Zarzalis, N. [2008]. Numeric simulation of the micro current in porous inert structure, *Chemie Ingenieur Technik* **80**(3): 327–341.

[61] Hackeschmidt, K. [2005]. Abschlussbericht: Grundsatzuntersuchungen zum einsatz offenporiger metallschäume in der luft-, kälte- und wärmetechnik., *Technical report*, Institut für Luft- und Kältetechnik GmbH.

[62] Hall, M. J. and Hiatt, J. P. [1994]. Exit flows from highly porous-media, *Physics of Fluids* **6**(2): 469–479.

[63] Hampel, U., Otahal, J., Boden, S., Beyer, M., Schleicher, E., Zimmermann, W. and Jicha, M. [2009]. Miniature conductivity wire-mesh sensor for gas-liquid two-phase flow measurement, *Flow Measurement and Instrumentation* **20**(1): 15–21.

[64] Han, N. W., Bhakta, J. and Carbonell, R. G. [1985]. Longitudinal and lateral dispersion in packed-beds - effect of column length and particle-size distribution, *Aiche Journal* **31**(2): 277–288.

[65] Hanjalic, K. and Kenjeres, S. [2008]. Some developments in turbulence modeling for wind and environmental engineering, *Journal of Wind Engineering and Industrial Aerodynamics* **96**(10-11): 1537–1570.

[66] Harleman, D. R. F., Mehlhorn, P. F. and Rumer, R. R. [1963]. Dispersion-permeability correlation in porous media, *Journal of the Hydraulics Division* .

[67] Haussener, S., Lipinski, W., Petrasch, J., Wyss, P. and Steinfeld, A. [2009]. Tomographic characterization of a semitransparent-particle packed bed and determination of its thermal radiative properties, *Journal of Heat Transfer* **131**(7): 072701 (11 pp.)–072701 (11 pp.).

[68] Hendershot, D. C. [2000]. Process minimization: Making plants safer, *Chemical Engineering Progress* **96**(1): 35–40.

[69] Hiby, J. W. [1979]. Definition and measurement of quality of mixing in liquid-mixtures, *Chemie Ingenieur Technik* **51**(7): 704–709.

[70] Hill, C. G. [1977]. *An Introduction to Chemical Engineering Kinetics and Reactor Design*, John Wiley and Sons.

[71] Hirschberg, S., Koubek, R., Moser, F. and Schock, J. [2009]. An improvement of the sulzer smx (tm) static mixer significantly reducing the pressure drop, *Chemical Engineering Research and Design* **87**(4A): 524–532.

[72] Horton, N. A. and Pokrajac, D. [2009]. Onset of turbulence in a regular porous medium: An experimental study, *Physics of Fluids* **21**(4).

[73] Huang, A. Y. L., Huang, M. Y. F., Capart, H. and Chen, R. H. [2008]. Optical measurements of pore geometry and fluid velocity in a bed of irregularly packed spheres, *Experiments in Fluids* **45**(2): 309–321.

[74] Johnson, I. D. [1987]. Method and apparatus for measuring water in crude oil, *US Patent 4644263* .

[75] Kader, B. A. [1981]. Temperature and concentration profiles in fully turbulent boundary-layers, *International Journal of Heat and Mass Transfer* **24**(9): 1541–1544.

[76] Karasso, P. S. and Mungal, M. G. [1997]. Plif measurements in aqueous flows using the nd:yag laser, *Experiments in Fluids* **23**(5): 382–387.

[77] Karimian, S. A. M. and Straatman, A. G. [2008]. Cfd study of the hydraulic and thermal behavior of spherical-void-phase porous materials, *International Journal of Heat and Fluid Flow* **29**(1): 292–305.

[78] Karman, T. v. [1932]. Mechanische aehnlichkeit und turbulenz, *Nach. Ges. Wiss. Göttingen Math-Phys. Klasse* pp. 58–76.

[79] Kaviany, M. [1995]. *Principles of Heat Transfer in Porous Media*, 2nd edn, Springer-Verlag, New York.

[80] Kling, K. and Mewes, D. [2003]. Quantitative measurements of micro- and macromixing in a stirred vessel using planar laser-induced fluorescence, *Journal of Visualization* **6**(2): 165–173.

[81] Kozeny, J. [1927]. Capillary motion of water in soils, *Sitzungsberichte der Akademie der Wissenschaften in Wien, Mathematisch-Naturwissenschaftliche Klasse* **136**(5-6): 271–306.

[82] Krishnan, S., Garimella, S. V. and Murthy, J. Y. [2008]. Simulation of thermal transport in open-cell metal foams: Effect of periodic unit-cell structure, *Journal of Heat Transfer-Transactions of the Asme* **130**(2): 5.

[83] Krishnan, S., Murthy, J. Y. and Garimella, S. V. [2006]. Direct simulation of transport in open-cell metal foam, *Journal of Heat Transfer-Transactions of the Asme* **128**(8): 793–799.

[84] Kruse, N. [2005]. *Isothermal and non-isothermal turbulent flow over solid waves*, PhD thesis, ETH Zurich, Switzerland.

[85] Kruse, N., Kuhn, S. and Von Rohr, P. R. [2006]. Wavy wall effects on turbulence production and large-scale modes, *Journal of Turbulence* **7**(31): 1–24.

[86] Kuhn, S. [2008]. *Transport Mechanism in Mixed Convective Flow over Complex Surfaces*, PhD thesis, ETH Zurich, Switzerland.

[87] Kuhn, S., Wagner, C. and von Rohr, P. R. [2007]. Influence of wavy surfaces on coherent structures in a turbulent flow, *Experiments in Fluids* **43**(2-3): 251–259.

[88] Kurtbas, I. and Celik, N. [2009]. Experimental investigation of forced and mixed convection heat transfer in a foam-filled horizontal rectangular channel, *International Journal of Heat and Mass Transfer* **52**(5-6): 1313–1325.

[89] Kuwahara, F., Yamane, I. and Nakayama, A. [2006]. Large eddy simulation of turbulent flow in porous media, *International Communications in Heat and Mass Transfer* **33**(4): 411–418.

[90] Levenspiel, O. [1958]. Longitudinal mixing of fluids flowing in circular pipes, *Industrial and Engineering Chemistry* **50**(3): 343–346.

[91] Levenspiel, O. [1999]. *Chemical Reaction Engineering*, third edition edn, John Wiley and Sons.

[92] Lilly, D. K. [1992]. A proposed modification of the germano-subgrid-scale closure method, *Physics of Fluids a-Fluid Dynamics* **4**(3): 633–635.

[93] Lohse, S., Kohnen, B. T., Janasek, D., Dittrich, P. S., Franzke, J. and Agar, D. W. [2008]. A novel method for determining residence time distribution in intricately structured microreactors, *Lab on a Chip* **8**(3): 431–438.

[94] Lu, T. J., Stone, H. A. and Ashby, M. F. [1998]. Heat transfer in open-cell metal foams, *Acta Materialia* **46**(10): 3619–3635.

[95] Macdonald, I. F., Elsayed, M. S., Mow, K. and Dullien, F. A. L. [1979]. Flow through porous-media - ergun equation revisited, *Industrial and Engineering Chemistry Fundamentals* **18**(3): 199–208.

[96] Mahdi, H., Lopez, P., Fuentes, A. and Jones, R. [2006]. Thermal performance of aluminium-foam cpu heat exchangers, *International Journal of Energy Research* **30**(11): 851–860.

[97] Mahjoob, S. and Vafai, K. [2008]. A synthesis of fluid and thermal transport models for metal foam heat exchangers, *International Journal of Heat and Mass Transfer* **51**(15-16): 3701–3711.

[98] Maire, E. and Buffiere, J. Y. [2000]. X-ray tomography of aluminum foams and ti/sic composites, *in* J. Baruchel, J. Y. Buffiere, E. Maire, P. Merle and G. Peix (eds), *X-Ray Tomography in Material Science*, Hermes Science Publications, Paris, pp. 115–125.

[99] Mao, Z. S., Xiong, T. Y. and Chen, J. Y. [1998]. Residence time distribution of liquid flow in a trickle bed evaluated using fft deconvolution with coordinated smoothing, *Chemical Engineering Communications* **169**: 223–244.

[100] Mills, P. L. and Dudukovic, M. P. [1988]. Deconvolution of noisy tracer response data by a linear-filtering method, *Aiche Journal* **34**(10): 1752–1756.

[101] Montillet, A., Comiti, J. and Legrand, J. [1993]. Axial-dispersion in liquid flow-through packed reticulated metallic foams and fixed-beds of different structures, *Chemical Engineering Journal and the Biochemical Engineering Journal* **52**(2): 63–71.

[102] Muller, R., Van Campenhout, H., Van Damme, B., Van Der Perre, G., Dequeker, J., Hildebrand, T. and Ruegsegger, P. [1998]. Morphometric analysis of human bone biopsies: A quantitative structural comparison of histological sections and micro-computed tomography, *Bone* **23**(1): 59–66.

[103] Nahman, N. S. and Guillaume, M. E. [1981]. Deconvolution of time domain waveforms in the presence of noise, *Deconvolution of time domain waveforms in the presence of noise* pp. v+115 pp.

[104] Navio, J. A., Colon, G., Litter, M. I. and Bianco, G. N. [1996]. Synthesis, characterization and photocatalytic properties of iron-doped titania semiconductors prepared from tio2 and iron(iii) acetylacetonate, *Journal of Molecular Catalysis a-Chemical* **106**(3): 267–276.

[105] Olurin, O. B., Arnold, M., Korner, C. and Singer, R. F. [2002]. The investigation of morphometric parameters of aluminium foams using micro-computed tomography, *Materials Science and Engineering a-Structural Materials Properties Microstructure and Processing* **328**(1-2): 334–343.

[106] Owens, D. K. and Wendt, R. C. [1969]. Estimation of surface free energy of polymers, *Journal of Applied Polymer Science* **13**(8): 1741–and.

[107] Parish, R. W. and Casson, D. W. J. [1976]. Detecting porosity, *Engineering* **216**(10): 730–731.

[108] Parruk, B. and Riad, S. [1984]. Study and performance if two iterative frequency-domain deconvolution techniques, *IEE Transactions on Instrumentation and Measurement* **IM-33, NO. 4**.

[109] Patankar, S. V., Liu, C. H. and Sparrow, E. M. [1977]. Fully developed flow and heat-transfer in ducts having streamwise-periodic variations of cross-sectional area, *Journal of Heat Transfer-Transactions of the Asme* **99**(2): 180–186.

[110] Pavel, B. I. and Mohamad, A. A. [2004]. Experimental investigation of the potential of metallic porous inserts in enhancing forced convective heat transfer, *Journal of Heat Transfer-Transactions of the Asme* **126**(4): 540–545.

[111] Pedras, M. H. J. and de Lemos, M. J. S. [2001]. Macroscopic turbulence modeling for incompressible flow through undeformable porous media, *International Journal of Heat and Mass Transfer* **44**(6): 1081–1093.

[112] Pestryakov, A. N., Lunin, V. V. and Petranovskii, V. P. [2007]. Catalysts based on foam materials for neutralization of waste gases, *Catalysis Communications* **8**(12): 2253–2256.

[113] Petrasch, J. [2007]. *Multi-scale analyses of reactive flow in porous media*, Phd thesis, ETH Zurich.

[114] Petrasch, J., Wyss, P., Stampfli, R. and Steinfeld, A. [2008]. Tomography-based multiscale analyses of the 3d geometrical morphology of reticulated porous ceramics, *Journal of the American Ceramic Society* **91**(8): 2659–2665.

[115] Petrasch, J., Wyss, P. and Steinfeld, A. [2007]. Tomography-based monte carlo determination of radiative properties of reticulate porous ceramics, *Journal of Quantitative Spectroscopy and Radiative Transfer* **105**(2): 180–197.

[116] Phanikumar, M. S. and Mahajan, R. L. [2002]. Non-darcy natural convection in high porosity metal foams, *International Journal of Heat and Mass Transfer* **45**(18): 3781–3793.

[117] Phillips, C. H., Lauschke, G. and Peerhossaini, H. [1997]. Intensification of batch chemical processes by using integrated chemical reactor-heat exchangers, *Applied Thermal Engineering* **17**(8-10): 809–824.

[118] Pippel, W. [1978]. *Verweilzeitanalyse in technologischen Stroemungssystemen.*, Akademie-Verlag-Berlin, Berlin.

[119] Pittard, M. T., Evans, R. P., Maynes, R. D. and Blotter, J. D. [2004]. Experimental and numerical investigation of turbulent flow induced pipe vibration in fully developed flow, *Review of Scientific Instruments* **75**(7): 2393–2401.

[120] Pope, S. B. [2005]. *Turbulent flows*, Cambridge University Press, Cambridge.

[121] Prasad, A. K. [2000]. Stereoscopic particle image velocimetry, *Experiments in Fluids* **29**(2): 103–116.

[122] Prasser, H. M., Bottger, A. and Zschau, J. [1998]. A new electrode-mesh tomograph for gas-liquid flows, *Flow Measurement and Instrumentation* **9**(2): 111–119.

[123] Raffel, M., Willert, C. and Kompenhans, J. [1998]. *Particle Image Velocimetry. A practical guide*, Springer.

[124] Ramamurty, U. and Paul, A. [2004]. Variability in mechanical properties of a metal foam, *Acta Materialia* **52**(4): 869–876.

[125] Ramshaw, C. [1983]. Higee distillation - an example of process intensification, *Chemical Engineer-London* (389): 13–14.

[126] Reinecke, N., Boddem, M., Petritsch, G. and Mewes, D. [1996]. Tomographisches messen der relativen phasenanteile in zweiphasigen strömungen fluider phasen, *Chemie Ingenieur Technik - CIT* **68**(11): 1404–1412.

[127] Reynolds, O. [1894]. On the dynamicaltheory of incompressible viscous flows and the determination of the criterion., *Philos. Trans. R. Soc. London Ser. A* **186**: 123–161.

[128] Richardson, J. T., Remue, D. and Hung, J. K. [2003]. Properties of ceramic foam catalyst supports: mass and heat transfer, *Applied Catalysis a-General* **250**(2): 319–329.

[129] Saez, A. E. and Carbonell, R. G. [1985]. Hydrodynamic parameters for gas-liquid cocurrent flow in packed-beds, *Aiche Journal* **31**(1): 52–62.

[130] Salas, K. I. and Waas, A. M. [2007]. Convective heat transfer in open cell metal foams, *Journal of Heat Transfer-Transactions of the Asme* **129**: 1217–1229.

[131] Sasov, A. and Van Dyck, D. [1998]. Desktop x-ray microscopy and microtomography, *Journal of Microscopy-Oxford* **191**: 151–158.

[132] Scarano, F. [2002]. Iterative image deformation methods in piv, *Measurement Science and Technology* **13**(1): R1–R19.

[133] Scarano, F. and Riethmuller, M. L. [2000]. Advances in iterative multigrid piv image processing, *Experiments in Fluids* **29**: S51–S60.

[134] Seguin, D., Montillet, A. and Comiti, J. [1998]. Experimental characterisation of flow regimes in various porous media - i: Limit of laminar flow regime, *Chemical Engineering Science* **53**(21): 3751–3761.

[135] Sherwood, T. K. and Holloway, F. A. L. [1940]. Performance or packed towers - liquid film data for several packings, *Transactions of the American Institute of Chemical Engineers* **36**(1): 0039–0070.

[136] Shih, W. H., Chiu, W. C. and Hsieh, W. H. [2006]. Height effect on heat-transfer characteristics of aluminum-foam heat sinks, *Transactions of the ASME. Journal of Heat Transfer* **128**(6): 530–537.

[137] Smagorinsky, J. [1963]. General circulation experiments with the primitive equations, *Monthly Weather Review* **91**(3): 99–164.

[138] Sonnenfeld, A., Hauert, R. and von Rohr, P. R. [2006]. Uv absorptance of titanium dioxide thin films by plasma enhanced deposition from mixtures of oxygen and titanium-tetrakis-isopropoxide, *Plasma Chemistry and Plasma Processing* **26**(3): 319–334.

[139] Spanne, P., Thovert, J. F., Jacquin, C. J., Lindquist, W. B., Jones, K. W. and Adler, P. M. [1994]. Synchrotron computed microtomography of porous-media - topology and transports, *Physical Review Letters* **73**(14): 2001–2004.

[140] Stampanoni, M., Borchert, G., Wyss, P., Abela, R., Patterson, B., Hunt, S., Vermeulen, D. and Ruegsegger, P. [2002]. High resolution x-ray detector for synchrotron-based microtomography, *Nuclear Instruments and Methods in Physics Research Section a-Accelerators Spectrometers Detectors and Associated Equipment* **491**(1-2): 291–301.

[141] Stemmet, C. P. [2008]. *Gas-liquid Solid Foam Reactors: Hydrodynamics and Mass Transfer.*, Dissertation, Eindhoven University of Technology.

[142] Stemmet, C. P., Bartelds, F., van der Schaaf, J., Kuster, B. F. M. and Schouten, J. C. [2008]. Influence of liquid viscosity and surface tension on the gas-liquid mass transfer coefficient for solid foam packings in co-current two-phase flow, *Chemical Engineering Research and Design* **86**(10A): 1094–1106.

[143] Stemmet, C. P., Jongmans, J. N., van der Schaaf, J., Kuster, B. F. M. and Schouten, J. C. [2005]. Hydrodynamics of gas-liquid counter-current flow in solid foam packings, *Chemical Engineering Science* **60**(22): 6422–6429.

[144] Stemmet, C. P., Schouten, J. C. and Nijhuis, T. A. [2009]. In-situ uv-visible and raman spectroscopy for gas-liquid-solid systems, *Industrial and Engineering Chemistry Research* **48**(17): 8205–8210.

[145] Stemmet, C. P., Schouten, J. C. and Nijhuis, T. A. [n.d.]. In situ uv-vis spectroscopy in gas-liquid-solid systems, *Chemical Engineering Science* **65**(1): 267–272.

[146] Stemmet, C. P., van der Schaaf, J., Kuster, B. F. M. and Schouten, J. C. [2006]. Solid foam packings for multiphase reactors - modelling of liquid holdup and mass transfer, *Chemical Engineering Research and Design* **84**(A12): 1134–1141.

[147] Stitt, E. H. [2002]. Alternative multiphase reactors for fine chemicals - a world beyond stirred tanks?, *Chemical Engineering Journal* **90**(1-2): 47–60.

[148] Sultan, K., DeGroot, C. T., Straatman, A. G., Gallego, N. C. and Hangan, H. [2009]. Thermal characterization of porous graphitic foam - convection in impinging flow, *International Journal of Heat and Mass Transfer* **52**(19-20): 4296–4301.

[149] Tabor, G., Yeo, O., Young, P. and Laity, P. [2008]. Cfd simulation of flow through an open cell foam, *International Journal of Modern Physics C* **19**(5): 703–715.

[150] Topin, F., Bonnet, J. P., Madani, B. and Tadrist, L. [2006]. Experimental analysis of multiphase flow in metallic foam: Flow laws, heat transfer and convective boiling, *Advanced Engineering Materials* **8**(9): 890–899.

[151] Trachsel, F., Gunther, A., Khan, S. and Jensen, K. F. [2005]. Measurement of residence time distribution in microfluidic systems, *Chemical Engineering Science* **60**(21): 5729–5737.

[152] Trefler, M. and Gray, J. E. [1976]. Characterization of imaging properties of x-ray focal spots, *Applied Optics* **15**(12): 3099–3104.

[153] Viot, P. and Bernard, D. [2005]. Polymeric foam behaviour under impact tests: deformation study by micro tomography, *in* C. A. Brebbia and A. A. Mammoli (eds), *Computational Methods and Experiments in Materials Characterisation II*, Vol. 51 of *Wit Transactions on Engineering Sciences*, Wit Press, Southampton, pp. 217–227.

[154] Von der Schulenburg, D. A. G., Paterson-Beedle, M., Macaskie, L. E., Gladden, L. F. and Johns, M. L. [2007]. Flow through an evolving porous media-compressed foam, *Journal of Materials Science* **42**(16): 6541–6548.

[155] Wadley, R. and Dawson, M. K. [2005]. Lif measurements of blending in static mixers in the turbulent and transitional flow regimes, *Chemical Engineering Science* **60**(8-9): 2469–2478.

[156] Wagner, C. [2007]. PhD thesis, ETH Zurich, Switzerland.

[157] Wagner, C., Kuhn, S. and von Rohr, P. R. [2007]. Scalar transport from a point source in flows over wavy walls, *Experiments in Fluids* **43**(2-3): 261–271.

[158] Wen, C. Y. and Fan, L. T. [1975]. *Models for Flow Systems and Chemical Reactors*, Marcel Dekker, New York.

[159] Westerweel, J. [1997]. Fundamentals of digital particle image velocimetry, *Measurement Science and Technology* **8**(12): 1379–1392.

[160] Westerweel, J. and Van Oord, J. [2000]. Stereoscopic piv measurements in a turbulent boundary layer, *Particle Image Velocimetry*, Vol. 56 of *Fluid Mechanics and Its Applications*, Kluwer Academic Publ, Dordrecht, pp. 459–478.

[161] Weszka, J. S. [1978]. Survey of threshold selection techniques, *Computer Graphics and Image Processing* **7**(2): 259–265.

[162] Willert, C. [1997]. Stereoscopic digital particle image velocimetry for application in wind tunnel flows, *Measurement Science and Technology* **8**(12): 1465–1479.

[163] Wyrwa, D. W. and Schmid, G. [2007]. Metal nanoparticles on stainless steel surfaces as novel heterogeneous catalysts, *Journal of Cluster Science* **18**(3): 476–493.

[164] Xu, W. G., Zhang, H. T., Yang, Z. M. and Zhang, J. S. [2008]. Numerical investigation on the flow characteristics and permeability of three-dimensional reticulated foam materials, *Chemical Engineering Journal* **140**(1-3): 562–569.

[165] Yu, Q. J., Thompson, B. E. and Straatman, A. G. [2006]. A unit cube-based model for heat transfer and fluid flow in porous carbon foam, *Journal of Heat Transfer-Transactions of the Asme* **128**(4): 352–360.

[166] Zerai, B., Saylor, B. Z., Kadambi, J. R., Oliver, M. J., Mazaheri, A. R., Ahmadi, G., Bromhal, G. S. and Smith, D. H. [2005]. Flow characterization through a network cell using particle image velocimetry, *Transport in Porous Media* **60**(2): 159–181.

[167] Zhao, C. Y., Lu, T. J., Hodson, H. P. and Jackson, J. D. [2004]. The temperature dependence of effective thermal conductivity of open-celled steel alloy foams, *Materials Science and Engineering a-Structural Materials Properties Microstructure and Processing* **367**(1-2): 123–131.

[168] Zuercher, S., Pabst, K. and Schaub, G. [2009]. Ceramic foams as structured catalyst inserts in gas-particle filters for gas reactions-effect of backmixing, *Applied Catalysis a-General* **357**(1): 85–92.

List of publications

Journal publications

1. Trachsel, F. and Hutter, C. and Rudolf von Rohr, P. R. Transparent silicon/glass microreactor for high-pressure and high-temperature reactions. *Chemical Engineering Journal*, 135: 309-316, 2008.
2. Hutter, C. and Allemann, C. and Kuhn, S. and von Rohr, P. R. Scalar transport in a milli-scale metal foam reactor. *Chemical Engineering Science*, 65(10): 3169-3178, 2010.
3. Hutter, C. and Zenklusen, A. and Kuhn, S. and von Rohr, P. R. Large eddy simulations of flow through a streamwise-periodic structure. *Chemical Engineering Science*, in print.
4. Hutter, C. and Zenklusen, A. and Lang, R. and von Rohr, P. R. Axial Dispersion in Metal Foam and Streamwise-Periodic Porous Media. *Chemical Engineering Science*, in print.

Patent

1. C. Hutter, Ph. Rudolf von Rohr, F. Mascarello, and D. Ruppen. Device for processing and conditioning of material transported through the device. *Patent Application*, (Case 27319 EP0), 2010.

Conference contributions

1. C. Hutter, and Ph. Rudolf von Rohr. Metal foam as static mixer for novel continuous mini plug flow reactors: Simultaneous PIV/LIF measurements. *11*$^{\text{th}}$ *Conference on Multiphase Flows*, Palermo, 2008.
2. C. Hutter, and Ph. Rudolf von Rohr. Metal foam reactor: Mass transfer study at the milli scale. *2nd International Congress on Green Process Engineering, 2nd European Process Intensification Conference*, Venice, 2009.
3. C. Hutter, and Ph. Rudolf von Rohr. Heat transfer characterization of a novel plug flow reactor. *2nd International Congress on Green Process Engineering, 2nd European Process Intensification Conference*, Venice, 2009.
4. C. Hutter, and Ph. Rudolf von Rohr. Multiphase flow characterization in laser sintered mini plug flow reactor with integrated structured porous media. *7*$^{\text{th}}$ *International Conference on Multiphase Flow*, Tampa, 2010.

Curriculum Vitae

Name:	Cédric Hutter
Date of birth:	July 15th, 1980
Nationality:	Swiss, citizen of Lalden (VS) and Eggerberg (VS)
Marital status:	Married
2007–2010	Doctoral studies at the Institute of Process Engineering, ETH Zurich (Prof. Dr. Dr. h.c. Ph. Rudolf von Rohr)
2006–2007	Teaching assistant at the Institute of Process Engineering, ETH Zurich
2001–2006	Study of Process Engineering at ETH Zurich (academic degree: MSc)
2004	Internship at Néstle Waters, Paris, France
2003	Internship at Lonza Group Ldt., Lalden, Switzerland
2002	Internship at Stahleinbau AG, Stalden, Switzerland
2000	Military service, Sion, Switzerland
1995–2000	Kollegium Spiritus Sanctus, Brig, Switzerland
1990–1995	Secondary school, Visp, Switzerland
1987–1990	Primary school, Visp, Switzerland

Zurich, June 2010